Tidal Deformation of Planets and Satellites: Models and Methods for Laser- and Radar Altimetry

vorgelegt von
Diplom Physiker
Gregor Steinbrügge
geb. in Berlin

von der Fakultät VI – Planen Bauen Umwelt
der Technischen Universität Berlin
zur Erlangung des akademischen Grades

Doktor der Naturwissenschaften
- Dr. rer. nat. -

genehmigte Dissertation

Vorsitzender:	Prof. Dr. Dr. h.c. Harald Schuh
Gutachter:	Prof. Dr. Jürgen Oberst
Gutachter:	Prof. Dr. Nicolas Thomas
Gutachter:	Prof. Dr. Tilman Spohn

Tag der wissenschaftlichen Aussprache: 27.03.2018

Berlin 2018

Contents

List of Figures

List of Tables

Abstract

In this thesis, methods are developed and studied for radar and laser altimetry to measure radial tidal deformations of planets and satellites. The thesis investigates further how the tidal measurement allows constraining the interior structure and rheologic properties of the bodies. A semi-analytical performance model for laser altimetry has been developed to predict probability of false detection and ranging accuracy. At cross-over locations of the ground tracks, which can be derived from the spacecraft trajectory, the tidal deformation can be retrieved by a differential height measurement. With a known tidal potential at the time of the passes and a sufficient number of cross-over points, it is possible to solve for the tidal Love number h_2.
On this basis, the geodetic inversion of h_2 is simulated for Mercury and the BepiColombo mission, with its BepiColombo Laser Altimeter (BELA). The measurement is affected by the high eccentricity of the spacecraft orbit and BELA's limited shot frequency (10 Hz), which leads to a large spot-to-spot distance and associated interpolation errors at the cross-over locations. The measurement of h_2 is further complicated by only small variations of the tidal potential and by Mercury's slow rotation rate. The accuracy of h_2 is predicted to be 0.14 (1-sigma) after two years in orbit.
A comparable simulation has been performed for Ganymede, where significant higher radial amplitudes are expected. For the Ganymede Laser Altimeter (GALA), on board the Jupiter Icy Moons Explorer (JUICE), the predicted absolute accuracy for Ganymede's tidal Love number h_2 is around 0.03 (1-sigma) after 132 days in a polar 500 km orbit. This result can be explained by higher tidal amplitudes, GALA's higher shot frequency (30 Hz), and by a more favorable distribution pattern of the measurable cross-over points.
For radar, an equivalent method has been developed, analyzed, and applied to the Radar for Europa Assessment and Sounding: Ocean to Near-surface (REASON) on board the Europa Clipper mission. The measurement accuracy of the radar is estimated to be between 3 and 15 m. The main drivers are the signal-to-noise ratio, which is heavily dependent on Europa's surface roughness, and Europa's dynamic ionosphere. As the Europa mission only involves a set of fast flybys limiting the orbit determination, a method has been conceived to solve for the spacecraft trajectory simultaneously with the tidal deformation. The expected h_2 accuracy is between 0.04 and 0.17 (1-sigma).
Further, it has been investigated how the h_2 measurement allows constraining the interior structure of the bodies, eventually together with the tidal Love number k_2. For Mercury, it has been shown that the h_2/k_2 ratio may set an upper bound on the inner core size. The ratio of both Love numbers allows for a stronger constraint on Mercury's core than other geodetic measurements, e.g., the libration amplitude. For Ganymede and Europa, the h_2 measurement can confirm the existence of a global, subsurface ocean beneath the ice shell. Combined with k_2, a constraint on the ice shell thickness to around $\pm$ 20 km can be provided via the linear combination $1 + k_2 - h_2$. The largest ambiguity in this measurement is the rheology of the ice.

Zusammenfassung

Die vorgelegte Dissertation entwickelt und untersucht Methoden der Radar- und Laseraltimetrie für die Messung radialer Gezeitendeformationen von Planeten und Monden. Sie untersucht außerdem, inwieweit die Gezeitenmessungen dazu beitragen, den inneren Aufbau und die rheologischen Eigenschaften der Körper zu bestimmen.
Für die Laser Altimeter wurde ein semi-analytisches Modell entwickelt, welches für gegebene Kenngrößen des Instruments, die Detektionswahrscheinlichkeit und Messgenauigkeit von Einzelschüssen ermittelt. Unter Berücksichtigung der Bahn der Raumsonde im Orbit lassen sich Kreuzungspunkte errechnen, an denen, durch Interpolation zwischen den Einzelschüssen, eine differenzielle Höhenmessung erfolgen kann. Mit dem bekannten Gezeitenpotential zu den jeweiligen Zeitpunkten einer Vielzahl von Messungen, lässt sich so die Lovesche Zahl h_2 bestimmen. Auf dieser Grundlage wurde die geodätische Bestimmung von h_2 für den Merkur und die Mission BepiColombo mit dem BepiColombo Laser Altimeter (BELA) simuliert. Zu berücksichtigen sind die hohe Bahn-Exzentrizität der Raumsonde und die begrenzte Schussfrequenz von BELA (10 Hz), wodurch die Abstände zwischen den Einzelschüssen und Interpolationsfehler an den Kreuzungspunkten groß werden. Messungen von h_2 auf dem Merkur werden zudem erschwert durch die nur geringen Schwankungen der Gezeitenverformung im erzeugenden Potential, sowie die langsame Rotation des Planeten. Die erwartete Genauigkeit der h_2 Messung mit BELA, nach einer zweijährigen Mission, ist mit 0.14 (1-sigma) abgeschätzt.
Zum Vergleich wurde eine ähnliche Simulation für Ganymed erstellt, für den eine deutlich höhere Gezeitenamplitude erwartet wird. Für das Ganymede Laser Altimeter (GALA), auf der Mission Jupiter Icy Moons Explorer (JUICE), liegt die erwartete Genauigkeit für h_2 bei ca. 0.03 (1-sigma) nach 132 Tagen in einem polaren 500 km Orbit. Dieser Wert gründet zum einen auf den höheren Gezeitenamplituden, zum anderen aber auch auf der höheren Schussfrequenz von GALA (30 Hz) und der vorteilhafteren Verteilung der messbaren Kreuzungspunkte.
Für das Radaraltimeter wurde ebenfalls ein Modell für die Abschätzung der Messgenauigkeit und ein Verfahren zur Gezeitenmessung entwickelt, speziell zugeschnitten auf das "Radar for Europa Assessment and Sounding: Ocean to Near-surface" (REASON) auf der Europa Clipper Mission. Der Messfehler des Radars wird auf 3 bis 15 m (1-sigma) bestimmt, in Abhängigkeit von Signalstärke und Rauschen, wobei beide Terme stark von der Rauhigkeit der Oberflächen abhängen. Ein limitierender Faktor der Messungen ist weiterhin der Einfluss von Europas dynamischer Ionosphäre. Da sich die Mission auf schnelle Vorbeiflüge am Jupitermond beschränkt und nach jetziger Planung Bahninfromationen nur mit relativ großen Ungenauigkeiten vorliegen werden, wurde ein Verfahren entwickelt, bei dem – gleichzeitig zu den Gezeitendeformationen – Bahnmodelle unter Zuhilfenahme von Kreuzungspunkten der Bodenspuren des Radars bestimmt wurden. Die zu erwartende, absolute Genauigkeit für h_2 liegt zwischen 0.04 und 0.17 (1-sigma). Außerdem wurde untersucht, inwieweit die h_2 Bestimmung, ggf. zusammen mit der Messung der Gezitenpotential Love-Zahl k_2, zu Modellen des inneren Aufbaus der Körper beitragen kann. Für Merkur wurde gezeigt, dass das Verhältnis h_2/k_2 Auskunft über den Radius des

festen, inneren Kerns geben kann. Das Verhältnis beider Lovescher Zahlen stellt eine stärkere Randbedingung für den Aufbau des Merkurkerns dar als andere geodätische Messungen, wie zum Beispiel die Messung der Librationsamplitude.
Für Ganymed und Europa kann die h_2 Messung einen Beweis für die Existenz eines globalen Ozeans unter der äußeren Eisdecke liefern. Zusammen mit der k_2 Messung kann mittels der Linearkombination $1 + k_2 - h_2$ die Mächtigkeit der Eisdecke auf ca. $\pm$ 20 km bestimmt werden. Die größte Unsicherheit in der Eisdickenbestimmung ist auf die Eisrheologie zurück zu führen.

Chapter 1

Introduction

Tidal interaction and resulting deformation of planets and satellites are key to understand the dynamics of our Solar System. They are relevant for understanding the rotational state of bodies (e.g., Goldreich (1965); Peale and Gold (1965)), their orbital evolution (e.g., Goldreich (1963); Goldreich and Peale (1966); Kaula (1964)), thermal state (e.g., Peale and Cassen (1978); Peale et al. (1979); Yoder and Peale (1981)) and to assess the habitability of icy satellites in the outer Solar System. The discovery of magnetic signatures by the Galileo mission, indicating subsurface oceans underneath the icy crusts of Europa, Ganymede and Callisto (Kivelson et al., 1999, 2000, 2002; Khurana et al., 1998), promoted the idea of tides as an alternative energy source sustaining putative habitable zones. Since then our understanding of the icy moons orbiting Jupiter but also Saturn significantly changed. Consequently, follow up missions are already confirmed and in preparation. The JUpiter ICy moons Explorer (JUICE) selected in 2012, as the first L-class mission in the Cosmic Vision program of the European Space Agency (ESA), is scheduled for launch in 2022 to explore the Jovian system with a special emphasis on Ganymede (Grasset et al., 2013). In parallel its neighbor Europa is the selected target for a dedicated multiple-flyby-mission scheduled by the National Aeronautics and Space Administration (NASA) for the same launch window (Pappalardo and Phillips, 2014). The voyage of both missions to the Galilean moons aims at an exploration of a very dynamic and complex system of which current knowledge is - literally - very superficial. The interior structure of the satellites, in particular the ice shell thicknesses and depths of the putative oceans remain unknown. The measurement of tides can hereby give invaluable insights into the deepest working principles of these bodies. By observing the response of the body to the external forcing by Jupiter, physical properties like shell-thickness and rheology can be inferred (e.g., Wu et al. (2001); Wahr et al. (2006)). But also constraints on the tidal dissipation rate and therefore ultimately on the thermal structure as well as on the evolution of the bodies can be set (e.g., Hussmann et al. (2002); Spohn and Schubert (2003)).

Not only for icy satellites, but also for bodies with rocky shells, studying tides can enhance our understanding of the interior. Especially when a global liquid layer, e.g., a sub-surface magma ocean, as in case of Io (Khurana et al., 2011), or alternatively a molten core, is present. For Mercury with its at least partially liquid core (e.g., Margot et al. (2012); Hauck et al. (2013); Padovan et al. (2014)), a new opportunity for such an endeavor arises with ESA's BepiColombo mission scheduled for launch in October 2018 (Benkhoff et al., 2010).

However, measurements of tidal deformations are challenging in practice, in particular the radial deformation as a response to the tidal force. Consequently, up to now, no such measurement could be performed outside the Earth-Moon system. Usually the amplitudes are in the order of meters and several effects have to be considered, leading to extremely tight error budgets. For this reason every attempt for a determination of radial tides needs careful preparation.

This thesis explores the capabilities of the future missions JUICE, Europa Clipper and BepiColombo for their potential to measure radial tidal deformations at Ganymede, Europa and

Mercury, respectively. It investigates the performance of the respective altimetric instruments, it proposes and analyzes appropriate measurement concepts and it investigates the attainable scientific results from a geophysical perspective. The interdisciplinary character of the thesis therefore allows to understand the measurement process from end-to-end to support efficient instrument designs and operation planning on these upcoming missions.

1.1 Structure of the Dissertation

The following introduction will, while limiting itself to the literature relevant for this thesis, give an overview on the bodies in question, namely the planet Mercury as well as the Jovian moons Europa and Ganymede. It will discuss the fundamentals of the tidal theory and the applications of it to bodies in our Solar System, following up by a brief introduction of the missions and altimetric instruments which are motivating this thesis. The core of the dissertation is then structured around four research papers listed in Table 1.1.

	Reference	**Status**
Paper I	**The performance of the BepiColombo Laser Altimeter (BELA) prior launch and prospects for Mercury orbit operations** G. Steinbrügge, A. Stark, H. Hussmann, K. Wickhusen, J. Oberst *Planetary and Space Science*, in press https://doi.org/10.1016/j.pss.2018.04.017	Accepted on April 21, 2018
Paper II	**Viscoelastic Tides of Mercury and the Determination of its Inner Core Size.** G. Steinbrügge, S. Padovan, H. Hussmann, T. Steinke, A. Stark, J. Oberst *Under review in JGR-Planets*	Under review Submitted on February 6, 2018
Paper III	**Measuring Tidal Deformations by Laser Altimetry. A Performance Model for the Ganymede Laser Altimeter.** G. Steinbrügge, A. Stark, H. Hussmann, F. Sohl, J. Oberst *Planetary and Space Science*, Volume 117, Pages 184–191, November 2015 https://doi.org/10.1016/j.pss.2015.06.013	Published
Paper IV	**Assessing the Potential for Measuring Europa's Tidal Love Number h_2 Using Radar Sounder and Topographic Imager Data.** G. Steinbrügge, D. M. Schroeder, M. S. Haynes, H. Hussmann, C. Grima, D. D. Blankenship *Earth and Planetary Science Letters* Volume 482, Pages 334–341, January 2018 https://doi.org/10.1016/j.epsl.2017.11.028	Published

Table 1.1: Publications constituting this thesis. The papers are not ordered chronologically but rather thematically to avoid impairing the reading flow when the thesis is considered in its entirety.

Paper I presents a performance model for digital laser altimeters validated on the BepiColombo Laser Altimeter (BELA) (Thomas et al., 2007) flight model. Based on this model the question about the in-orbit performance of the instrument is discussed and an estimate of the measurement accuracy of Mercury's tidal Love number h_2 is given.
Paper II investigates the interior structure of Mercury based on the MErcury Space, Surface ENvironment, GEochemisty, and Ranging (MESSENGER) mission (Solomon et al., 2011) results and how the tidal Love number h_2 could be used as an additional constraint for interior modeling. A special focus is set on the currently unknown size of Mercury's inner core and it is shown that the tidal measurement can indeed provide an upper bound on the inner core size.
In Paper III, the instrument performance of the Ganymede Laser Altimeter (GALA) (Hussmann et al., 2014, 2017) is investigated, the accuracy of the h_2 measurement is estimated, and implications for Ganymede's ice shell thickness are given.
Since no laser altimeter is aboard the Europa Clipper mission, new altimetric techniques were developed for enabling the mission to perform a tidal measurement. This is done in Paper IV which investigates the possibility to solve for h_2 using a combination of radar altimetry and digital terrain models derived from camera images. A further challenge arises here because of the nature of a flyby trajectory and limited orbit determination accuracy. Therefore, the inversion part needs to solve simultaneously for the orbit of the spacecraft as well as for h_2 of Europa. At the end of the paper, further implications for the determination of the ice shell thickness are given.

1.1.1 Icy Satellites

Europa

Tidal energy as an additional heat source to radiogenic heating is particularly important in the context of the outer Solar System. Tidal energy can become the dominant heat source (Hussmann et al., 2002), in the case of icy satellites potentially even sustaining a habitable zone (Reynolds et al., 1983). An archetype of an icy satellite is Europa, which constitutes together with Io, Ganymede, and Callisto the Galilean moons of Jupiter. The surface is predominantly covered by water ice and only shows few impact craters, which indicates a relatively young age on geological time scales (Prockter et al., 2010). The most common landforms which can be inferred from image data obtained from the Voyager and Galileo missions are ridges (Figueredo and Greeley, 2000) and bands (Tufts et al., 2000). These features are indicating an active geologic environment. The explanation of the formation of many features on Europa's surface involves the presence of very low viscosity ice or liquid water underneath the icy crust (Pappalardo et al., 1999). Evidence that a global, electrically conductive layer on Europa is still present today, putatively in the form of a global, subsurface ocean are based on induced magnetic field measurements (Kivelson et al., 2000) and thermal considerations. In order to maintain such an ocean, tidal energy plays an important role to avoid freezing on a body with a distance 5 AU away from the Sun. Aside from the magnetic field measurements, constraints on the interior of Europa are based on the measurement of the total mass and the mean moment of inertia (MoI) (Anderson et al., 1998). These measurements suggest that Europa is differentiated into an iron core and a silicate mantle, which is overlain by the H_2O layer(s) (Schubert et al., 2004).
However, from the total mass and MoI no information about ocean depth or ice shell thickness can be obtained due to the small density contrast between liquid water and ice. Therefore, this important parameter remains unknown but two extreme cases, one being a thin, only few kilometers thick conductive ice layer (Greenberg et al., 1999), and the other case being a thicker,

at least 15–20 km deep, convective one (Pappalardo et al., 1998) can be distinguished. While the thin ice model is considered less likely today due to mainly geophysical reasons (e.g., McKinnon (1999); Hussmann et al. (2002)), at least the presence of local near-surface water reservoirs cannot be ruled out (Schmidt et al., 2011).
Additional information on the interior can come from measuring geodetic parameters like the obliquity, librations, or tides. The obliquity of Europa is expected to be small, slightly depending on the presence of a global liquid layer. Therefore, an accuracy of one arcsecond, corresponding to 100 m at the surface (on the spin pole location) would be needed to confirm the presence of an internal ocean (Baland et al., 2012). However, the libration amplitude strongly reduced in case of a subsurface ocean due to the tides. As a consequence the amplitude is expected to be at the same level as without subsurface ocean (Van Hoolst et al., 2013). A confirmation of a subsurface ocean or a constraint on the ice shell thickness from the libration measurement alone is therefore not possible. However, it has been pointed out by numerous authors that a definitive evidence for the presence of a subsurface ocean can be provided by the determination of the tidal Love numbers (e.g., Edwards et al. (1997); Moore and Schubert (2000); Wu et al. (2001); Wahr et al. (2006)). Wu et al. (2001) showed in a covariance analysis that a future orbiter could measure k_2 with an accuracy of 4×10^{-4} allowing to constrain the ice shell thickness when combined with a measurement of the physical librations. Wahr et al. (2006) demonstrated that the measurement could be even improved when measuring the diminishing factor $1 + k_2 - h_2$. This linear combination of h_2 and k_2 has the advantage that it depends less on the rigidity of the outer ice shell and therefore provides a less ambiguous estimate of the ice shell thickness. The authors estimated that an orbiter with a 30-day mission lifetime equipped with a laser altimeter and 1 m measurement accuracy could measure the tidal Love number h_2 with an accuracy of $< 1\%$. It is pointed out in Paper I and Paper III though, that the accuracy of the laser is usually not dominating the error budget and that such estimates are fairly optimistic. In Paper IV it is shown that in the frame of the Europa Clipper mission the h_2 accuracy by radar altimetry is in the order of 5 - 20 %, also due to the nature of the flyby mission, nonetheless allowing to confirm a putatively global ocean on Europa.
The recent discovery of plumes on Europa with Hubble Space Telescope (HST) observations (e.g., Roth et al. (2014); Sparks et al. (2017); Sparks et al. (2018)) further emphasizes the activity of the moon. While the presence of liquid water is not a sufficient criteria of habitability, the likelihood would be further increased by active sea-floor volcanism and the related exchange of minerals with the silicate layer. Tides can help to test for an active silicate layer by observing the tidal phase-lag which is directly related to the tidal dissipation. Hussmann et al. (2016) pointed out that the tidal difference between the k_2 and h_2 phase-lags is a strong indicator for putative sea-floor volcanism. Further, a lander could directly measure linear combinations of k_2, h_2 and l_2 on the surface of Europa by observing the surface acceleration, star motion and surface tilt (Hussmann et al., 2011).
Therefore, also beyond the exploration by the Europa Clipper, tidal deformations can and will be used for revealing Europa's interior structure and to characterize the moon as a potential habitable environment.

Ganymede

Due to the larger distance to Jupiter as well as due to the lower eccentricity of its orbit, Ganymede is subjected to less significant tidal forces as compared to Europa and Io and consequently to a lower heat production. This is well reflected by its surface morphology. About one third of the surface is covered by heavily cratered dark terrain, characterized by a low albedo. However, it is generally assumed that the surface is still younger as of the neighboring Callisto (Schoemaker and Wolfe, 1982; Neukum, 2001) being close to be saturated with craters (Zahnle et al., 1998). The predominant feature of this terrain are furrows, large-scale fracture systems being remnants of multiringed structures (Smith et al., 1979; Prockter et al., 2010). The remaining two thirds of Ganymede's surface are bright, or grooved terrain forming swaths that cross-cut dark terrains and possibly formed by intense tectonism during a phase of global expansion (Bland et al., 2009). The light terrain is less cratered and contains grooves which are interpreted to be the result of tectonic resurfacing like seen on Europa (Head et al., 2002). Further, its surface also contains features which have been interpreted previously to be of cryovolcanic origin (Head et al., 1998). However, in contrast to Europa, no direct evidence for present or past cryovolcanic activity currently exists.
Ganymede, as the largest satellite in the Solar System, is characterized by a unique interior structure. An iron core with an ongoing dynamo (Bland et al., 2008; Rückriemen et al., 2015), supporting an intrinsic magnetic dipole field (Kivelson et al., 2002), is overlain by a silicate mantle and a H_2O layer (Schubert et al., 2004). The latter is possibly subdivided into at least three layers of different ice phases. Due to the high pressure, the outermost ice I layer transitions in the deep interior into high-pressure ice of the form III, V or VI (Sotin et al., 1998). It has been shown on theoretical grounds, that a liquid layer would be thermally stable, sandwiched between the two ice layers (Spohn and Schubert, 2003). The presence of this subsurface ocean is in agreement with the induced magnetic field measurements from the Galileo mission (Kivelson et al., 2002). However, also models with multiple alternating layers of liquid water and different forms of high pressure ice have been suggested (Vance et al., 2014). The presence of a subsurface ocean is also in agreement with more recent HST observations (Saur et al., 2015), monitoring the oscillations of Ganymede's auroral oval which amplitudes depend on the presence of an ocean.
For the future exploration of Ganymede, the same geodetic measurements as in the case of Europa could further reveal the interior structure. However, in the case of Ganymede, resonant amplifications from some long periodic forcing terms lead to a stronger sensitivity of the obliquity to the interior structure (Baland et al., 2012). An ocean could thereby easily be detected if the obliquity is significantly different from the solid case state at the time of observation. The libration amplitude suffers from the same constraints as in the case of Europa, leading to a decreased amplitude due to tides (Van Hoolst et al., 2013).
The missing interface between the ocean and the silicate layer goes at the expense of the habitability due to the deprivation of a direct exchange of minerals between the two layers. Nonetheless, it has been suggested that such an exchange could take place on longer timescales by convection through the high-pressure ice (Choblet et al., 2017; Kalousova et al., 2018). As in the case of Europa, a measurement of Ganymede's tidal Love numbers can provide strong evidence on the presence for a subsurface ocean and allow for constraining its thickness and rheology even if the amplitudes are expected to be considerably lower (e.g., Moore and Schubert (2003); Paper III; Kamata et al. (2016)). However, with a well designed laser altimeter aboard of an orbiter mission, a better accuracy in h_2 is achievable than in case of Europa (Paper III, Paper IV). The better accuracy potentially also allows for the determination of the tidal phase-lag, allowing to test for dissipation in the high-pressure ice phase (Hussmann et al., 2016) and obtain additional information on the ice I rheology (Paper III).

1.1.2 Mercury

From 2011 to 2015 Mercury was investigated by the MErcury Space, Surface ENvironment, GEochemisty, and Ranging (MESSENGER) orbiter which was the first spacecraft inserted into Mercury orbit (Solomon et al., 2011). Equipped with eight instruments, it provided numerous new findings about the planet which had the reputation to be the least understood of the Solar System beforehand. The innermost planet has an orbital period of 88 days and a rotation period of 59 days and is locked in a stable 2:3 spin-orbit resonance (Colombo and Shapiro, 1966). It is the only known body of our Solar System trapped in such a rotational state. Further, due to the proximity to the Sun, the orbit of Mercury is affected by an advance of the longitude of pericenter related to effects of general relativity. The gravitational torques of the Sun also force Mercury into a Cassini state with a 300,000-year period precession of the orbital plane at a fixed rate around the Laplace plane (Peale, 1969). It is most commonly assumed that the origin of this resonance is rather old and related to Mercury's high eccentricity (Noyelles et al., 2014). However, also an origin from a retrograde spin-state has been suggested (Wieczorek et al., 2012). Although, with a radius of 2439.6 km (Perry et al., 2015) Mercury is the smallest planet of the Solar System, it sustains a weak magnetic dipole field already observed by the Mariner 10 mission (Ness et al., 1975). Further mapping by the MESSENGER mission revealed a north-south asymmetry (Anderson et al., 2011). The origin of the magnetic field is related to a large iron core. The gravitational parameter GM of the planet has been inferred from MESSENGER radio science experiments to $(2.203209 \pm 0.000091) \times 10^{13}$ m/s^2 (Verma and Margot, 2016) leading to a mean density of 5427.75 kg/m^3. Together with Mercury's radius, the density indicates that a significant fraction of Mercury's composition is iron. The measurement of the polar moment of inertia by Earth based radar observations (Margot et al., 2012), later using updated MESSENGER radio science observations (Mazarico et al., 2014b), as well as from a measurement of the physical librations at the 88 days orbital period using laser altimetry and stereo imaging data (Stark et al., 2015b) gave values between 0.343 and 0.349. A value below 0.4 indicates that Mercury is a differentiated planet. Based on these geodetic constraints, the core size has been inferred to be around 2000 km in radius (Hauck et al., 2013). The physical state of the core can be further revealed by measuring the physical librations in combination with the asymmetry of the gravity field (Peale, 1976a, 1988; Peale et al., 2002). Indeed, the observed libration amplitude of around 39 arcsec (Margot et al., 2012; Stark et al., 2015b) confirms that the core is at least partially molten. Based on thermal evolution models (e.g. Stevenson et al. (1983); Spohn et al. (2001); Grott et al. (2011); Tosi et al. (2013)), this implies that the core also contains some amount of sulfur to avoid freezing. Further constraints are derived from the measurement of Mercury's tidal Love number k_2, determined to be 0.451 ± 0.014 by Mazarico et al. (2014b) and 0.464 ± 0.023 by Verma and Margot (2016). Based on the k_2 determination of Mazarico et al. (2014a), Padovan et al. (2014) examined multiple interior models in agreement with the measurement. The authors showed that in presence of a liquid core with known size, k_2 is informative with regard to the mantle properties. They inferred a cold and/or rigid mantle and further concluded that the presence of a previously suggested solid FeS layer (Malavergne et al., 2010; Smith et al., 2012) is only consistent with the measurements when the temperature at the core mantle boundary (CMB) is < 1600 K.

Mercury's surface is dominated by very rough and heavily cratered terrain (Kreslavsky et al., 2014) but shows also smoother areas, mainly in the northern hemisphere originating from more recent flood volcanism (Head et al., 2011). Prominent geologic features on the surface are lobate scarps and wrinkle ridges which have been interpreted to be related to a contraction of Mercury's crust that lead to a shrinking of the planets radius of about 7 km (Byrne et al., 2014). The contraction is due to the cooling process of the planet, started about 2.5 Gyr ago, proceeding

at a constant rate, and ongoing today (Tosi et al., 2013).
Despite the plentiful new discoveries made by the MESSENGER mission a set of open questions remain. Some of these are linked to the surface, where only the northern hemisphere has been mapped with high resolution images and laser altimetry. Some others are linked to the interior like the question whether an inner solid core exists. Paper II proposes a concept to test for the presence of an inner core based on the measurement of radial tidal deformations by the BepiColombo Laser Altimeter (BELA) (compare to Section 1.4.3) and Paper I shows that such a measurement is feasible within an extended mission of BepiColombo.

1.2 Theory of Tides

All major moons in the Solar System are tidally locked to their parent body meaning that they rotate synchronously with their orbital revolution. In cases when the orbital eccentricity is high and the tidal interaction is weak then the body might also become trapped in a higher spin-orbit resonance, e.g., 2:1 or as in case of Mercury 3:2 (Makarov, 2012). In many cases the spin-orbit resonance is complemented by orbital resonances between different bodies. Well known examples are the Neptune–Pluto 3:2, the Enceladus–Dione 2:1, or Titan–Hyperion 4:3 orbital resonances. Io, Europa, and Ganymede constitute a special case, being trapped in a 1:2:4 three body resonance known as the Laplace resonance (e.g., Peale (1976b); Yoder (1979)). Resonances have the important property to force an increased orbital eccentricity of their members which is a necessary criteria for sustaining tides over long periods of time in a tidally locked body. The amount of tidal energy dissipated depends on the interior structure and on the intensity of the tidal potential raised by the central body. The latter increases linearly with the mass of the central body and decreases with the third power of the distance (see Section 1.2.1). Therefore, bodies in vicinity to their parent body can be subjected to immense tidal forces. The most prominent example is Io where tidal heating is the predominant heat source (e.g., Yoder and Peale (1981); Ross and Schubert (1985); Segatz et al. (1988)) leading to a partially molten interior as predicted by Peale et al. (1979).

1.2.1 Tidal Potentials

A tidal potential is generated whenever an extended body is exposed to a gravitational force of a second body. While the tidal force is exerted reciprocally, for simplicity, I focus throughout this section on the orbiting body in the tidal potential of its central body. The general form of the tidal potential can be expressed as an expansion in spherical harmonics. Let a body be at a distance R of its tide generating central body, then the gravitational potential V at any point can be expressed as

$$V = \frac{GM}{R} \sum_{l=2}^{\infty} \left(\frac{r}{R}\right)^l P_l^0(\cos(\phi)), \tag{1.1}$$

where r is the distance to the center of mass of the satellite, G is the gravitational constant, M is the mass of the tide generating body, $P_l^0(\cos(\phi))$ are the associated Legendre polynomials of degree l and order 0 and ϕ is the angle between the center of mass of the central body and the computation point.
With known ephemerides and a known rotational state of the body in question, the expression given in Equation (1.1) can directly be evaluated numerically. However, it should be noted that the tidal potential in the given form contains two components. A static and a periodic one.

While the static component is usually accounted for in the equilibrium shape, expressed by the spherical harmonic shape coefficients C_{20} and C_{22}, only the periodic term describes the dynamic body tides. To avoid confusion, in the following V will denote the total tidal potential, while Φ will be used when only the periodic part is considered. For many applications, it is favorable to have a more convenient analytical expression describing the latter part Φ. The derivation formulates Equation (1.1) in terms of averaged orbital elements semi-major axis a, eccentricity e, inclination i, longitude of ascending node Ω, argument of pericenter ω and mean anomaly M. The resulting expression can be formulated for a point expressed in a body-fixed coordinate system in terms of co-latitude θ and longitude λ according to Kaula (1964) as

$$V = \frac{GM}{R} \sum_{l=2}^{\infty} \left(\frac{r}{R}\right)^l \sum_{m=0}^{l} \frac{(m-l)!}{(m+l)!}(2-\delta_{0m}) P_l^m(\cos\theta) \tag{1.2}$$

$$\cdot \sum_{p=0}^{l} F_{lmp}(i) \sum_{q=-\infty}^{\infty} G_{lpq}(e) S_{lmpq}(\omega, M, \Omega, \Theta) \tag{1.3}$$

with δ_{0m} being the Dirac delta function defined by

$$\delta_{0m} = \begin{cases} 0 & m \neq 0 \\ 1 & m = 0 \end{cases} \tag{1.4}$$

and S_{lmpq} capturing the constraints arising from the spin-orbit resonance,

$$\begin{aligned} S_{lmpq} = &\begin{bmatrix} C_{lm} \\ -S_{lm} \end{bmatrix}_{l-m \text{ odd}}^{l-m \text{ even}} \cos\left[(1-2p)\omega + (1-2p+q)M + m(\Omega-\Theta)\right] \\ &+ \begin{bmatrix} S_{lm} \\ C_{lm} \end{bmatrix}_{l-m \text{ odd}}^{l-m \text{ even}} \sin\left[(1-2p)\omega + (1-2p+q)M + m(\Omega-\Theta)\right]. \end{aligned} \tag{1.5}$$

The coefficiencts S_{lm} and C_{lm} are given by

$$C_{lm} = \cos(m\lambda) \quad \text{and} \quad S_{lm} = \sin(m\lambda). \tag{1.6}$$

$F_{lmp}(i)$ and $G_{lmp}(e)$ are functions dependent on the inclination and eccentricity, respectively. They are tabulated in Kaula (1964). For a body trapped in a 1:1 resonance and with a mean motion n, the resulting expression up to second degree, first order eccentricity and 0-th order inclination can be described as (e.g., Segatz et al. (1988); Moore and Schubert (2000); Hussmann et al. (2011))

$$\Phi_2(r,\theta,\phi,t) = r^2 n^2 e \left[-\frac{3}{2} P_2^0(\cos\theta)\cos M + \frac{1}{4} P_2^2(\cos\theta)(3\cos M\cos 2\phi + 4\sin M \sin 2\phi)\right]. \tag{1.7}$$

Using Φ indicates, that the static part of the potential has been dropped and the index 2, that the potential has been developed up to second degree, i.e. $l = 2$. For bodies with small eccentricity and low inclination, Equation (1.7) is a good approximation to Equation (1.1). It should nonetheless be noted, that Equation (1.7) assumes a Keplerian orbit and a perfectly resonant rotation, which in the case of the Galilean satellites only applies if the orbital elements are averaged over long time scales. It is obvious from the expression that the tidal potential for a tidally locked body vanishes when the eccentricity is zero.
For the case of Mercury in the 3:2 resonance, an analytical formula for the second degree tidal

potential in first order eccentricity and 0-th order inclination has been given by Balogh and Giampieri (2002)

$$\Phi_2 = \frac{GMr^2}{8a^3}\left[12e\cos(M)P_2^0(\cos(\theta))\left(e\cos(2M+2\lambda) - 2\cos(M+2\lambda)\right)P_2^2(\cos(\theta))\right]. \quad (1.8)$$

However, due to the large eccentricity of Mercury ($e = 0.205$) the approximation yields in this case errors up to 20%. In order to obtain an adequate expression one has to expand the tidal potential at least up to degree 2 in eccentricity. The resulting expression is then

$$\begin{aligned}\Phi_2 = &\frac{GMr^2}{8a^3}\Big\{2\left[2+3e^2+6e\cos(M)+9e^2\cos(2M)\right]P_2^0(\cos(\theta)) + \big[-17e^2\cos(M-2\lambda)\\ &-7e\cos(2\lambda)+e\cos(2M+2\lambda)-2\cos(M+2\lambda)+5e^2\cos(M+2\lambda)\big]P_2^2(\cos(\theta))\Big\}. \quad (1.9)\end{aligned}$$

The derivation of Equation (1.9) can be found in Annex A. Further, a Mathematica notebook to compute analytical expressions for tidal potentials up to arbitrary order in eccentricity and inclination for any mean motion resonance can be found in the supplementary material of this thesis. To achieve an accuracy below 1%, an expansion up to 4-th order in eccentricity is necessary. Better results are barely possible because of the assumption of a resonant rotation, but the analytical version saves much computational time compared to the numerical approach. However, due to the inaccuracy of the analytical approximation, I will use only Equation (1.1) when evaluating the tidal potential of Mercury in Paper I.

1.2.2 Response of Planetary Bodies to Tidal Forces

Studying the interior of planetary bodies is important. Not only because many surface features are telltale signs of interior processes, but also because the properties of the interior dictate the thermal evolution (and vice-versa) and thereby constrain the planetary formation history. However, information on the interior properties of planetary bodies have to be mostly inferred from orbit. Common methods are radio science experiments, studying the mass distribution and the use of magnetometers since the magnetic field can give valuable information about the interior. The total mass of a body, together with the radius, provides information about the mean density which already constrains the bulk composition. In case of Mercury a mean density of > 5400 kg/km^3(e.g., Mazarico et al. (2014a); Verma and Margot (2016)) implies a significant amount of iron. Contrariwise, Ganymede's mean density of ≈ 1940 kg/m^3 (e.g., Schubert et al. (2004)) suggests a large amount of volatiles in the composition of the satellite. Since the bodies can be described also as a tri-axial ellipsoid, the moment of inertia (MoI) can be determined. It is mostly expressed for a body of mass m and radius R as a dimensionless entity MoI$= C/(mR^2)$ based on the polar moment of inertia C. The MoI quantifies how well a planet or moon is differentiated. A homogenous sphere has an MoI of exactly 0.4, for differentiated bodies the value is lower. However, if the density contrast between the different layers is low, e.g., like between liquid water and solid ice, the MoI cannot reveal these distinct layers.
The response of a body to tidal forces can be expressed by the Love numbers h and k (Love, 1909) as well as by the Shida number l (Shida and Matsuyama, 1912). These dimensionless, complex numbers are characterized by an amplitude and a phase. Love's number h describes the radial deformation of the surface u_r as a consequence of an external potential Φ_{ext} with respect to the shifted equipotential surface, i.e. the static equilibrium tide Φ_{ext}/g, where g is the gravitational acceleration at the surface.

$$u_r = h\frac{\Phi_{\text{ext}}}{g}. \quad (1.10)$$

The tidal forcing further leads to a redistribution of mass in the interior, generating a secondary gravitational potential $\Phi_{\rm int}$. The Love number k is the ratio between this induced gravity potential and the external tidal potential

$$\Phi^{\rm int} = k\Phi^{\rm ext}. \tag{1.11}$$

And finally, Shida's number l characterizes the lateral displacement u_t

$$u_t = l\frac{\nabla\Phi^{\rm ext}}{g}. \tag{1.12}$$

The Love-Shida numbers are a measure of the elastic properties of the body but further depend on the density structure. For a completely rigid body $h = k = l = 0$. As the tidal potential is usually expanded in spherical harmonics, the Love-Shida numbers can also be expressed as a function of degree n. Usually the expansion is truncated at degree 2, such that the tidal Love number h_2, k_2 and l_2 express the response of the body to the external potential Φ_2.
For a homogenous, incompressible body the tidal Love-Shida numbers can be calculated analytically (Munk and MacDonald, 1960)

$$k_2 = \frac{k_2^f}{1+\widetilde{\mu}} \qquad h_2 = \frac{5}{3}k_2 \qquad l_2 = \frac{k_2}{2}. \tag{1.13}$$

Thereby the fluid Love number k_2^f is 3/2 for a homogenous body and $\widetilde{\mu}$ is the effective shear modulus

$$\widetilde{\mu} = \frac{19\mu}{2\rho g r}, \tag{1.14}$$

depending on the density ρ and the complex rigidity μ. In case of more complex bodies with multiple layers, the Love numbers can be calculated numerically using e.g., a matrix propagation method (Wieczerkowski, 1999). If the deformation of the body is at least partially inelastic, the reaction of the body is not instantaneous leading to tidal friction which generates heat. Tidal forcing is therefore an energy source for planetary bodies in addition to radiogenic heating. The inelasticity is described by the quality factor Q (Zschau, 1978) defined by

$$Q^{-1} = \frac{1}{2\pi E^*}\oint\frac{\partial E}{\partial t}dt, \tag{1.15}$$

where the integral over the dissipation rate $\partial E/\partial t$ is the dissipated energy over a complete tidal cycle and E^* the peak energy stored in the system. By introducing Q as a free parameter, Munk and MacDonald (1960) as well as Kaula (1964) gave an analytic expression for the dissipation rate. Zschau (1978) expressed the tidal dissipation rate as a function of the imaginary part of k_2. For a body in synchronous rotation the dissipation rate then becomes

$$\frac{\partial E}{\partial t} = \frac{21}{2}\frac{r^5 n^5 e^2}{G}\mathrm{Im}(k_2). \tag{1.16}$$

Equation (1.16) is only valid if the inclination of the body's equator with respect to the orbital plane of the central body is set to zero and only terms up to second degree in eccentricity are accounted for.
For a body in 3:2 resonance and zero-th order inclination as well as fourth order in eccentricity the mean tidal dissipation rate has been given by Makarov and Efroimsky (2014) as

$$\frac{\partial E}{\partial t} = \frac{GM^2 r^5 n}{a^6}\left(\frac{3}{4} - \frac{39}{16}e^2 + \frac{2043}{32}e^4\right)\mathrm{Im}(k_2). \tag{1.17}$$

A particularity of the 3:2 resonance is that the tidal dissipation only weakly depends on the eccentricity. This leads to small dissipation rates, even for high eccentricities like in the case of Mercury. Indeed, it will be shown in Paper II that when respecting the geodetic constraints as determined by the MESSENGER mission the maximum surface heat flux due to tides is only 0.16 W/m^2.

1.3 Measuring Tidal Deformations

1.3.1 Measurement Concepts

In order to measure the radial tidal deformations the tidal signal has to be separated from other effects requiring a good coverage of observables in space and time. The most straight forward approach is the cross-over technique. When ground tracks of an altimeter cross at a certain location, the tidal amplitude can be retrieved by a differential measurement. This requires however, that the two measurements take place at different tidal phases and that the trajectory at both passes is accurately known. The advantage of the method is that the topography cancels out. The technique has been successfully applied for correcting ground track profiles of the Mars Orbiter Laser Altimeter (MOLA) instrument aboard Mars Global Surveyor (Neumann et al., 2001), in application to the Lunar Orbiter Laser Altimeter (LOLA) on board the Lunar Reconnaissance Orbiter (Mazarico et al., 2012), and for the Mercury Laser Altimeter (MLA) (Mazarico et al., 2014a). It can be used to improve the orbit solution (e.g., Smith et al. (2000), Mazarico et al. (2012)) and enhance the determination of the gravity field (e.g Lemoine et al. (2001), Genova et al. (2013)). With LOLA, a detection of radial tidal deformations was achieved for the first time with a space probe from orbit (Mazarico et al., 2014b).
An alternative method has been conceived by Koch et al. (2008, 2010), proposing to derive the tidal signal from spherical harmonics. The technique has the advantage of using the full data set. However, it needs to simultaneously solve for the topography with an accuracy in the same order of the tidal signal, which makes it very sensitive to orbit errors and high order topography. In both cases the spacecraft needs an altimetric instrument, usually a laser altimeter, but also radar instruments might be used. However, whatever altimetric instrument is used, the observable is the range from the spacecraft to the surface. In order to derive data products, like topography, librations or tides from that observable, additional information on the position of the spacecraft, the pointing, the reference frame, and the ephemeris data of the body in question are required.

1.3.2 Laser Altimetry

The first global topographic model from laser altimetry in planetary exploration was derived from the lidar on board the Clementine mission (Nozette et al., 1994; Zuber et al., 1994; Smith et al., 1997). The along track spacing was only between 20 – 100 km due to the low pulse repetition rate of 0.6 Hz. However, the high accuracy of the lidar emphasized the utility of the instrument such that laser altimeters became common payloads on planetary exploration missions. In 1996 the Mars Orbiter Laser Altimeter (MOLA) was launched on the Mars Global Surveyor (MGS) orbiter (Zuber et al., 1992) and successfully mapped Mars (Smith et al., 1999). In the following, a novelty was the Lunar Laser Altimeter, or LOLA (Smith et al., 2010), aboard the Lunar Reconnaissance Orbiter (LRO) (Chin et al., 2007) with five laser beams generating a pattern on

the surface, allowing the measurement of two dimensional roughness profiles (Kreslavsky et al., 2013). After seven years in orbit the instrument provided a full topographic map of the Moon with horizontal resolutions from 5 to 400 m (Smith et al., 2017) and albedo at 1064 nm (Lucey et al., 2014). Also the instrument allowed for laser ranging investigations (Zuber et al., 2010). Laser ranging can help to calibrate the instrument alignment (Sun et al., 2014), increase the quality of the orbit determination (Löcher and Kusche, 2014), and even allow for a calibration of the on-board clock (Bauer et al., 2017).
Also aboard the MESSENGER mission (Solomon et al., 2011) a laser altimeter was among the payload with the Mercury Laser Altimeter (MLA) (Cavanaugh et al., 2007). Due to the highly eccentric orbit of the spacecraft, only the northern hemisphere was mapped during the four years of operation (Zuber et al., 2012). Topographic maps were derived (Kreslavsky et al., 2014) and permanently shadowed craters investigated (Deutsch et al., 2016; Deutsch et al., 2018). Further, for the first time, a laser link over an interplanetary distance of 0.2 AU was established (Smith et al., 2006).
Full coverage of Mercury including also the Southern hemisphere is expected with the upcoming BepiColombo mission (Benkhoff et al., 2010). Part of the scientific payload of the mission is the BepiColombo Laser Altimeter, or BELA (Thomas et al., 2007). The BELA instrument will thereby be the first European laser altimeter for planetary exploration.
Having good performance models for laser altimeters for planetary exploration is necessary to reliably plan out missions and to responsibly allocate resources like mass, power, and data rate. Finding the right balance is not a trivial problem. The lidar on Clementine had a too limited laser link budget which lead to performance issues and many false detections on rough terrain (Smith et al., 1997). On Mars, MOLA had a very good link budget but under clear conditions over most surfaces, laser pulse returns exceeded the digital range of the MOLA detector leading to a pulse saturation (Neumann et al., 2003).
Most of the recently flown laser altimeters, like MOLA, MLA, or LOLA have an analog signal chain (e.g., Abshire et al. (2000); Cavanaugh et al. (2007)), implying that the return pulse is detected by an avalanche photo diode (APD) and the resulting photo current is compared to a threshold value. Usually the signal is filtered beforehand to avoid that single spikes in the noise profile lead to a false detection. Performance models for this concept have been developed by Gardner (1982, 1992) and are still the baseline for any link-budget calculation. The European instruments BELA and GALA will operate slightly different since no threshold detection is applied anymore. Instead the pulse will be digitized and detected with a matched filter algorithm (Thomas et al., 2007). Such a method requires efficient algorithms and hardware in order to keep up with the shot frequency of up to 50 Hz in case of GALA. A first attempt to work out a respective model to this concept on theoretical grounds has been made by Gunderson et al. (2006) in application to BELA. The model has been refined in some points in Gunderson and Thomas (2010). With the availability of test data (e.g., Gouman et al. (2014a,b); Althaus et al. (2014)) the models had to be revised leading to the current version of the BELA performance model which is presented in Paper I.

1.3.3 Radar Altimetry

On Earth radar altimeters are most commonly used to monitor sea levels and measure land heights. Examples for such systems are the radar altimeter RA2 aboard ESA's Envisat mission (Benveniste et al., 2002) or SIRAL aboard CryoSat-2 (Wingham, 2005). In planetary science radars are used either as imaging radars or as sounders. The first application was the sounder used aboard Apollo 17 with the Apollo Lunar Sounder Experiment (Phillips et al., 1973) (not

counting the avionics radars used e.g., for docking also on previous Apollo missions). However later on, only imaging radars were used, e.g., with the Soviet Venera missions and on board the Magellan mission to penetrate Venus cloud layers. With the Mars Advanced Radar for Subsurface and Ionosphere Sounding (MARSIS) (Jordan et al., 2009) a sounder has been used for the first time again since the Apollo era. Aboard ESA's MarsExpress (Chicarro and Science Team, 2003) it detected e.g., buried basins underneath the surface (Watters et al., 2006). Since 2006 it is complemented by the SHAllow RADar sounder (SHARAD) (Seu et al., 2004) aboard NASA's Mars Reconnaissance Orbiter (Zurek and Smrekar, 2007). On the Cassini mission, the radar (Elachi et al., 2004) proved to be a very versatile instrument. It has been used as an imaging radar (e.g., Elachi et al. (2006), Paganelli et al. (2007), Lopes et al. (2007)) and as well as an altimeter (e.g., Zebker et al. (2009); Mastrogiuseppe et al. (2014)). While the high center frequency (K_u-band) did not allow for using it as a sounder for ice, it was nonetheless possible to measure the depth of some shallow hydrocarbon lakes on Titan (Mastrogiuseppe et al., 2014; Mastrogiuseppe et al., 2018).
The future exploration of icy satellites in the outer Solar System will rely to an important part on radar sounders with higher wavelengths to penetrate the icy shells and search for sub-surface water reservoirs. The technique is well established for ice sheets and glaciers on Earth (Fretwell et al., 2013) and allows to characterize the form, flow and thickness (e.g., Dowdeswell and Evans (2004); Gogineni et al. (2014); MacGregor et al. (2015)) and to draw conclusions on their physical states (Schroeder et al., 2014; Greenbaum et al., 2015). Also for the polar ice sheets of Mars the technique has been successfully applied in the past (Seu et al., 2004; Plaut et al., 2007). It is therefore not surprising that two radar sounders have been selected to fly aboard the upcoming icy moon missions to the Jovian system with the Radar for Icy Moon Exploration (RIME) (Bruzzone et al., 2013) aboard JUICE and the Radar for Europa Assessment and Sounding: Ocean to Near-surface (REASON) (Blankenship et al., 2009; Moussessian et al., 2015) on the Europa Clipper mission. The latter is a dual frequency radar with a HF (high frequency, i.e. 3–30 MHz) and a VHF (very high frequency, i.e. 30–300 MHz) antenna. While the purpose of the HF band antenna is primarily to directly detect a subsurface ocean or local water reservoirs, the VHF antenna can also be used as an altimetric instrument. The main difference to laser altimetry is the lower inherent resolution of the radar and most importantly the fact that the radar is pulse limited while the laser is beam limited. That means that the footprint of the laser altimeter is limited by the laser beam width, i.e. the beam divergence. The footprint of the radar however is limited by the respective pulse limited zones, i.e. zones where the returns contribute to the same range bin. On a flat surface the first return would come from nadir while on rougher surfaces the origin of the return can become more confusing. But the radar profits from having Doppler information available in addition to the time of flight data. The altimetric capabilities of a radar can therefore be enhanced using the delay/Doppler technique proposed by Raney (1998, 2012). A concept will be presented in Paper IV combining radar delay/Doppler data with stereo images. It will be shown that the technique can thereby be further improved to a point where a tidal signal from Europa can be retrieved.

1.4 Missions and Instruments

1.4.1 REASON and the Europa Clipper Mission

The Europa Clipper (Pappalardo and Phillips, 2014) was approved in 2015 as a NASA flagship mission and is since 2016 part of the Ocean Worlds Exploration Program. It is intended as a

flyby mission with currently 46 planned Europa flybys (as of 17F12v2 trajectory). The spacecraft is equipped with nine instruments powered by solar panels. The launch is scheduled for 2022. The baseline launch vehicle is the Space Launch System (SLS) which would allow for a direct trajectory to Jupiter with a cruise time of less than three years.
One of the instruments aboard is the Radar for Europa Assessment and Sounding: Ocean to Near-surface (REASON) (Blankenship et al., 2009; Moussessian et al., 2015). REASON is a dual-band radar sounder composed of a VHF band operating at 60 MHz with a 10 MHz bandwidth and an HF band operating at 9 MHz with a 1 MHz bandwidth. The instrument is nadir looking and the chirp length is adjustable between 30 and 100 μs. The radar's main purpose is to characterize the surface and subsurface of Europa's ice shell by means of sounding (Aglyamov et al., 2017), reflectometry (Grima et al., 2015b), and altimetry (Paper IV). The estimated sounding depth is around 30 km but depends on the dielectric properties and thermal state of the ice shell. Due to the high radio noise emissions from Jupiter between 1–10 MHz (Cecconi et al., 2012), the HF antenna cannot be used for sub-Jovian sounding. Therefore, also passive sounding concepts have been investigated (Schroeder et al., 2016). Further, Galileo revealed a dynamic ionosphere in the vicinity of Europa (Kliore et al., 2002). The resulting effects on the radar signal propagation have been investigated by Grima et al. (2015a). Paper IV will describe the performance of REASON with respect to altimetry and emphasize that the ionosphere also imposes a significant challenge on the tides measurement.

1.4.2 GALA and the JUICE Mission

The JUICE mission (JUpiter ICy moons Explorer) (Grasset et al., 2013) was selected in 2012 as the first large class mission in ESA's Cosmic Vision program. Scheduled for the same launch window as the Clipper in 2022, it will be launched with an Ariane 5 and reach the Jovian system in 2029 after 7.6 years of cruise. The Jovian tour includes two Europa flybys as well as multiple Callisto and Ganymede flybys before entering orbit around Ganymede in 2033 and thereby being the first spacecraft entering an orbit around a moon of another planet. The spacecraft carries ten instruments, one being the Ganymede Laser Altimeter (GALA) (Hussmann et al., 2014, 2017). The most important phase of the mission will begin for GALA when the initially high altitude orbit is lowered to 500 km, which will be maintained for 132 days. In this short phase, compared to the complete mission duration, GALA aims at completing its two main scientific goals: 1) obtaining a global topographic coverage of Ganymede and 2) detect its radial tidal deformations (Hussmann et al., 2017). Secondary objectives are (a) the determination of the rotational state of Ganymede including rotation rate, librations, and obliquity. (b) the measurement of the surface roughness on different scales, i.e. from spot to spot but also within the laser footprint by analyzing the pulse width. And (c) to measure the geometric albedo at the laser wavelength. GALA therefore has a geological, geodetic and geophysical purpose. The instrument is a pulsed laser altimeter operating with two (cold-)redundant 17 mJ Nd:YAG lasers at 1064 nm. The nominal shot frequency is 30 Hz but adjustable up to 50 Hz. The ranging performance of the instrument in terms of signal-to-noise ratio and probability of false detection is described in Paper III. The capability to measure the rotational state by laser altimetry has been investigated by Steinke et al. (2015) and the estimated accuracy for the tidal measurement is described in Paper III.

1.4.3 BELA and the BepiColombo Mission

BepiColombo is a missions composed of two spacecraft, the Mercury Planetary Orbiter (MPO) under responsibility of ESA and the Mercury Magnetospheric Orbiter built and managed by the Japan Aerospace Exploration Agency (JAXA). After its launch in October 2018 and seven years of cruise the MPO will enter in a polar 400×1500 km orbit and investigate Mercury for a nominal mission lifetime of one year with the possibility of a second year of mission extension. The BELA instrument (Thomas et al., 2007) aboard is the first European laser altimeter built for a planetary science mission. Due to the eccentric orbit of the MPO the instrument was equipped with two redundant 50 mJ laser operating at a shot frequency of 10 Hz. A main challenge of the mission as well as for the instrument design is the harsh thermal environment at Mercury which lead to the implementation of special reflective *Stavroudis Baffles* to protect the instrument from the infrared flux (Beck et al., 2011). A novelty of the design compared to previous instruments is also the range detection mechanism which finds the pulse by digital filter matching instead of an analog threshold detection (Beck, 2012).
BELA's main scientific purpose is to provide a global topography map of Mercury (Paper I). Further goals are the determination of the rotational state, surface roughness, albedo at 1064 nm and to determine the radial tidal deformations of Mercury. The instrument might also allow a better orbit determination (Hosseiniarani et al., 2017).

Chapter 2

Research Paper I

The performance of the BepiColombo Laser Altimeter (BELA) prior Launch and Prospects for Mercury Orbit Operations

G. Steinbrügge, A. Stark, K. Wickhusen, H. Hussmann, J. Oberst

German Aerospace Center, Institute of Planetary Research, D-12489 Berlin, Germany

Published in Planetary and Space Science, in press
doi: 10.1016/j.pss.2018.04.017
Postprint

Abstract

We explore the perspectives of the BepiColombo Laser Altimeter (BELA) onboard ESA/JAXA's Mercury mission BepiColombo and present an updated semi-analytical instrument performance model, in which we estimate signal-to-noise ratio, single shot probability of false detection, range errors and the accuracy of pulse width reconstruction. The model is generally applicable for other laser altimeters using matched filter algorithms for pulse detection and has been validated against the recently tested BELA flight model after integration on the BepiColombo spacecraft. Further, we perform numerical simulations of the instrument performance expected in orbit about Mercury. In particular, we study the measurement accuracy of topography, slopes and surface roughness, which will allow us to estimate local and global topographic coverage based on the current trajectory design. We may also assess the potential for measuring the tidal Love number h_2 using cross-over points, which we estimate to be constrained with an absolute accuracy of 0.14 corresponding to a relative accuracy of about 18% after two years in Mercury orbit.

2.1. Introduction

After three flybys by the Mariner 10 probe in 1974 and 1975 the MErcury Space, Surface ENvironment, GEochemisty, and Ranging (MESSENGER) was the first spacecraft inserted into Mercury orbit in 2011 (Solomon et al., 2011). The high density of Mercury and the presence of an intrinsic magnetic field already observed by Mariner 10 have been linked to an extended liquid core, underneath a relatively thin mantle. By measurements of Mercury's 88-days libration amplitude and obliquity (Margot et al., 2007; Stark et al., 2015b) and determination of the gravity field including the tidal Love number k_2 (Mazarico et al., 2014b; Verma and Margot, 2016) the size and state of the core could be further constrained. However, due to the eccentric orbit of MESSENGER, the Mercury Laser Altimeter (MLA) (Cavanaugh et al., 2007) could not cover the Southern Hemisphere and the tidal Love number h_2 of Mercury remains unknown.

The BepiColombo joint mission by the European Space Agency (ESA) and the Japan Aerospace Exploration Agency (JAXA) consists of two spacecraft, the Mercury Planetary Orbiter (MPO) and the Mercury Magnetospheric Orbiter (MMO), which will complement and extend the data collected by MESSENGER. The two spacecraft will be launched in 2018 and conduct a one year nominal mission in Mercury orbit, with the possibility of an extension by one additional year (Benkhoff et al., 2010). One of the instruments aboard the MPO is the BepiColombo Laser Altimeter (BELA) (Thomas et al., 2007). While previous laser altimeters, e.g. the Mars Orbiter Laser Altimeter (MOLA) (Zuber et al., 1992) used matched filters followed by an analog leading edge detection, BELA uses digital matched filters, implemented in a field programmable gate array (FPGA) (Thomas et al., 2007). The resulting instrument performance has been modeled on theoretical grounds by Gunderson et al. (2006) and Gunderson and Thomas (2010). Following tests with the BELA qualification model the instrument parameters were reassessed and performance models were updated, which included models for alignment and pointing stability (Gouman et al., 2014b).

In the following, we present an improved performance model (Section 2.2) based on data from end-to-end tests carried out on the BELA flight model. The updated model allows us to analyze the expected scientific performance in terms of coverage (Section 2.3) and measurements of Mercury's radial tidal deformations (Section 2.4). Our performance models may also be generally applicable to other laser altimeters if using the same digital filter matching approaches as BELA.

2.2. Instrument Performance Modeling

The fundamental principal of laser altimetry is to send out short laser pulses from the transmitter towards the surface. The light is scattered by the area illuminated by the laser, referred to as footprint. Only a small fraction of the emitted photons return back to the receiver. The two-way travel time Δt of the photons measured by a high-accuracy clock can be translated into a range z by using the speed of light c and

$$z = \frac{c\Delta t}{2}. \tag{2.1}$$

To assess the instrument performance we base our calculations upon models originally developed by Gunderson et al. (2006) and Gunderson and Thomas (2010), consisting of two steps. In the first step the link budget is calculated, involving knowledge of the spacecraft altitude and the optical path of the laser pulse. It determines the energy of the return pulse received by the detector based on the instrument characteristics (e.g. laser energy and telescope radius) and further depends on the surface properties. The second part assesses the influence of optical and electronic noise, which interfere with the returned signal. To detect the signal, filters are needed to increase the signal-to-noise ratio (SNR) and to reduce the probability of false detection (PFD).

With ongoing instrument development and recent availability of test data we report on updates of earlier models, especially in the description of the critical instrument characteristics SNR and PFD. For reference, we keep the same notations as in the original publications while commenting on the changes we introduced.

2.2.1. Link Budget

The number of photons emitted by the transmitter laser at wavelength λ_T is given by

$$n_0 = \frac{E_T \lambda_T}{hc}. \tag{2.2}$$

The constants h and c are the Planck constant and the speed of light, respectively. The laser pulse energy E_T is generally specified as the energy emitted

by the instrument i.e., neglecting internal energy losses such as by the collimator efficiency. The laser pulse travels from the transmitter to the surface, which may have a slope angle of θ_R and a normal albedo of α_N. Thereby, the slope is considered as the angle between the surface normal and the nadir direction. In case of a nadir looking laser altimeter, the bidirectional reflectance at zero phase-angle is (Hapke, 1981; Gunderson et al., 2006)

$$\rho(\theta_R, \theta_R, 0) = \rho_0 = \alpha_N/\pi. \tag{2.3}$$

The pulse is then scattered from the surface and emitted into the complete hemisphere. A small fraction of the reflected laser light is captured by the receiver telescope. Since the full laser footprint falls within the receiver field of view, the amount of returning photons is proportional to the solid angle Ω_R covered by the telescope. The integration is therefore performed over the telescope aperture as seen from the center of the laser pulse footprint and

$$\Omega_R = 4\pi \sin^2\left(\frac{\theta_{AP}}{2}\right) \approx \pi\theta_{AP}^2 \quad [\text{sr}], \tag{2.4}$$

with θ_{AP} being the half-cone angle of the aperture as seen from ground, which can be computed from the spacecraft altitude H and the radius of the receiver telescope r_R as

$$\theta_{AP} = \tan^{-1}(r_R/H) \quad [\text{rad}]. \tag{2.5}$$

Due to surface slope and roughness the pulse is broadened in time. We assume that the laser beam has a Gaussian cross section and that the pulse has a Gaussian shape with a width of σ_0 in the time domain. Under these given presupmtions, the widths can be quadratically added and the return pulse captured by the telescope will have a Gaussian profile as well, with a temporal width of

$$\sigma_t = \sqrt{\sigma_0^2 + (2\delta_z/c)^2} \quad [\text{s}^2]. \tag{2.6}$$

Thereby, we express the roughness δ_z within the footprint as

$$\delta_z = \frac{H}{2}\tan(\theta_T)\tan(\theta_R) \quad [\text{m}]. \tag{2.7}$$

Note, that the factor $\frac{1}{2}$ is a further deviation from the original work of Gunderson et al. (2006), but consistent with the common approach taken in the literature (e.g. Gardner (1992); Neumann et al. (2003); Abshire et al. (2000)). The deviation arises from a different perception of the slope angle. E.g. Abshire et al. (2000) uses the slope as the angle between the surface normal and the nadir direction, while Gunderson et al. (2006) uses a roughness angle computed based on the rms height deviation from the mean elevation within the footprint. Even if both approaches are self-consistent we will continue with the more common definition used e.g. in Abshire et al. (2000). By exchanging the $1/e^2$ definition of the beam divergence with an $1/\sqrt{e}$ and by inserting Equation (2.7) into Equation (2.6), we get

$$\sigma_t^2 = \sigma_0^2 + (4H^2/c^2)\tan^2(\theta_T)\tan^2(\theta_R) \quad [\text{s}]. \tag{2.8}$$

This expression corresponds to Equation (4) from Abshire et al. (2000). Since the receiver field of view is larger than the laser beam divergence angle, the total energy of the return pulse E_R is given by

$$E_R = E_T\rho_0\Omega_R\epsilon_o\epsilon_t \quad [\text{J}], \tag{2.9}$$

where the efficiency of the system consists of the optical efficiency of the telescope ϵ_o and the transmission efficiency of the optical bandpass filter ϵ_t. Likewise, we can also compute the total amount of returning photons as

$$n_R = n_0\rho_0\Omega_R\epsilon_o\epsilon_t. \tag{2.10}$$

The optical power of the focused return pulse illuminating the avalanche photodiode (APD) can then be described as a Gaussian pulse of the form

$$P(t) = \frac{E_R}{\sqrt{2\pi}\sigma_t}\exp\left(-\frac{t^2}{2\sigma_t^2}\right) \quad [\text{W}], \tag{2.11}$$

which is translated into a photocurrent

$$I(t) = \frac{qn_R\epsilon_{qe}}{\sqrt{2\pi}\sigma_t}\exp\left(-\frac{t^2}{2\sigma_t^2}\right) \quad [\text{A}], \tag{2.12}$$

where q and ϵ_{qe} are the elementary charge and the quantum efficiency of the APD, respectively.

2.2.2. Signal-to-Noise Ratio

Due to the limited bandwidth B_0 of the receiver system, the analog signal experiences an additional broadening (Gunderson and Thomas, 2010), which can be quantified by

$$\sigma_p = 1/(2\sqrt{2\pi}B_0) \quad [\text{s}], \tag{2.13}$$

leading to a total temporal width of the Gauss function of

$$\sigma = \sqrt{\sigma_t^2 + \sigma_p^2} \quad [\text{s}]. \tag{2.14}$$

or full width half maximum of

$$\text{FWHM} = 2\sqrt{2\ln 2}\sigma \quad [\text{s}]. \tag{2.15}$$

The response of the APD to the incoming power is usually expressed by the responsivity at unity gain R_0 which can be directly measured or derived from the quantum efficiency ϵ_{qe} as

$$R_0 = \frac{q\lambda}{hc}\epsilon_{qe} \quad [\mathrm{A/W}]. \tag{2.16}$$

With the signal peak power after the analog bandpass

$$P_{\mathrm{peak}} = 2\sqrt{\frac{\ln 2}{\pi}}\frac{E_R}{\mathrm{FWHM}} = \frac{E_R}{\sqrt{2\pi}\sigma} \quad [\mathrm{W}], \tag{2.17}$$

and a given APD gain M the analog signal becomes

$$S_{\mathrm{analog}} = R_0^2 M^2 P_{\mathrm{peak}}^2 R_i^2 \quad [\mathrm{V}^2]. \tag{2.18}$$

For better comparability with the test results we express the signal in terms of voltage using the resistance of the feedback resistor within the transimpedance amplifier (TIA) R_i. The noise consists of four components. Solar noise, dark current, shot noise, and the electronic noise floor which in case of BELA is dominated by electric and magnetic disturbances (EMC noise) of the laser diode while firing (see Kallenbach et al. (2016) for further details). The first contribution, the solar noise, is the sunlight reflected from the surface of the planet within the field of view of the receiver.
The solar flux F at a distance d_{Sun} from the Sun at the laser wavelength of 1064 nm is according to Wehrli (1985)

$$F_0 = 0.643 \cdot \left(\frac{d_{\mathrm{Earth}}}{d_{\mathrm{Sun}}}\right)^2 \quad [\mathrm{W\ m^{-2}nm^{-1}}]. \tag{2.19}$$

Here, d_{Earth} is the distance to the Sun from Earth, i.e. 1 AU. The receiver captures all solar noise inside the field of view θ_{FoV} of the telescope which, on the surface is an area of[1]

$$A_{FOV} = \pi H^2 \tan^2(\theta_{FoV}) \quad [\mathrm{m}^2]. \tag{2.20}$$

We express the reflected sunlight by a cosine law assuming a Lambertian surface and a solar incidence angle of i and, contrary to the original work by Gunderson et al. (2006), we do not use a Hapke model (Hapke, 1981) to calculate the surface reflectance. The simplification is justified by the low influence of the solar noise on the measurement accuracy, even at Mercury. The resulting photocurrent is dependent on the width of the optical filter σ_{RF} around the central wavelength λ and can be expressed as

$$I_s = q\epsilon_t\epsilon_o\epsilon_{qe}\rho_0\cos(i)A_{FoV}\Omega_R\frac{F\lambda}{hc}\sigma_{rf} \quad [\mathrm{A}]. \tag{2.21}$$

[1] We assume that Equation (14) in Gunderson et al. (2006) has a typo which is corrected here.

The second contribution is the APD dark current, where surface I_{ds} and bulk I_{db} dark current of the APD are usually distinguished. Surface dark current does not trigger avalanche events within the substrate itself and is therefore independent of the APD gain. Bulk dark current, however, describes the electrical current within the pn-junction of the APD and therefore undergoes a multiplication process.

$$I_d = I_{ds} + MI_{db} \quad [\mathrm{A}]. \tag{2.22}$$

When illuminated, the APD experiences additional noise due to the statistical nature of the multiplication process. This contribution is called shot noise and depends on the incident optical power P_{opt}.

$$I_{sn} = P_{\mathrm{opt}}R_0 \quad [\mathrm{A}] \tag{2.23}$$

The dominant term, when the laser is operating, however, is EMC noise which we express here as a noise floor n_f. A more detailed description of the EMC noise characteristics of the instrument can be found in Kallenbach et al. (2016). Since the receiver measures a differential signal, the instrument is not sensitive to a constant noise level, but only to noise fluctuation. Presuming that all these current fluctuations are distributed as white uncorrelated Gaussian noise, the total noise can be expressed as sum of the constituent variances, i.e. $\mathrm{var}(I_i) = 2qBI_i$. For consistency with the signal we express the noise in terms of voltage.

$$N = 2qB_0R_i^2 \cdot \left[I_{ds} + (I_s + I_{db} + I_{sn})M^{2+x} + n_f^2\right] \quad [\mathrm{V}^2], \tag{2.24}$$

with x being the excess noise exponent. This leads to the following expression for the analog SNR.

$$\mathrm{SNR}_{\mathrm{analog}} = \frac{S_{\mathrm{analog}}}{N} \tag{2.25}$$

$$= \frac{R_0^2M^2P_{\mathrm{peak}}^2}{2q\left[I_{ds} + (I_s + I_{db} + I_{sn})M^{2+x} + n_f^2\right]} \cdot \frac{R_i^2}{B_0R_i^2} \quad \left[\frac{\mathrm{V}^2}{\mathrm{V}^2}\right] \tag{2.26}$$

In contrast to classical laser altimeter approaches used in space applications where the pulse is identified via a threshold detection, the analog SNR is not a good figure of merit for instruments using a digital filter matching approach since single noise spikes will not lead to a false detection even in case their amplitude exceeds the peak power of the laser pulse. This allows the instrument to operate at analog SNR values < 1. The basic concept of the filter matching has been outlined in Gunderson et al.

(2006) and Gunderson and Thomas (2010), however does not fully capture the maximum potential of the instrument performance. We therefore describe the signal by calculating the overlap of the incoming pulse with itself.

$$S = R_0^2 M^2 \cdot \int_{-\infty}^{\infty} \left[\frac{E_R}{\sqrt{2\pi}\sigma} \exp\left(-\frac{t^2}{2\sigma^2}\right) \exp\left(-\frac{1}{2}\frac{\tau_{\mathrm{adc}}}{\sigma}\right)\right]^2 dt = \frac{R_0^2 M^2 E_R^2}{4\pi\sigma^2} \exp\left(-\frac{\tau_{\mathrm{adc}}}{\sigma}\right) \quad [\mathrm{A}^2] \tag{2.27}$$

The additional exponential factor accounts for the dependence of the digital signal from the finite sampling frequency τ_{adc} of the analog-digital converter (ADC). This leads to a significantly decreased effective signal for very short pulses and must therefore be accounted for.

However, the actually implemented algorithm is performing a more complex correlation between the pulse candidate and the possible template functions and since the filter matching algorithm is a numerical process it is not possible to derive its performance analytically and it would be impractical to reproduce this numerical process for each shot in the following simulations. Therefore, the relation used in this work has been found empirically by testing the actually implemented algorithm for a statistical set of laser pulses under different SNR conditions. The noise floor used for this simulation has been measured onboard the spacecraft during laser operation and therefore within a representative EMC environment. However, the ground test setup did not allow for using optical laser pulses to assess the ranging performance. Therefore, we synthesized Gaussian pulses with energies representing different altitudes and surface slopes and introduced them artificially on the noise samples. We computed pulses with a width corresponding to a surface slope of 0°, 10°, 20°, and 40°. For each altitude between 400 and 2500 km a synthetic laser pulse has been generated and inserted in a random location within the range window. We then consider a false detection when the wrong sample in the return window has been identified as the location of the return pulse. We find that the empirical relation between SNR and PFD is best fit by a complementary Gauss error function of the form

$$\mathrm{PFD} = \frac{\mathrm{erfc}(0.69 \cdot \mathrm{SNR} - 1.64)}{1.98}. \tag{2.28}$$

The error of the approximation compared to the algorithm result is < 0.06. The instrument parameters used in the evaluation of the model are listed in Table 3.1. Figure 2.1 shows the PFD as a function of altitude for return pulses for the respective surface slopes. While the dots mark the PFD based on the measured noise floor and the numerical analysis of the onboard algorithm, the solid lines show the performance as predicted by the semi-analytical model. However, to make both data sets comparable, we had to remove the shot noise from the model since the APD was not illuminated during the ground test. The remaining discrepancies mainly reflect the idealistic model assumptions. It is assumed in the semi-analytical model that the noise is composed of fully white noise, while the real measured noise spectrum is not entirely flat. Further, there is a second order dependency of the PFD from the return pulse width, which is not accounted for in this model. The performance, as expected in orbit, including the shot noise is displayed with the dashed lines.

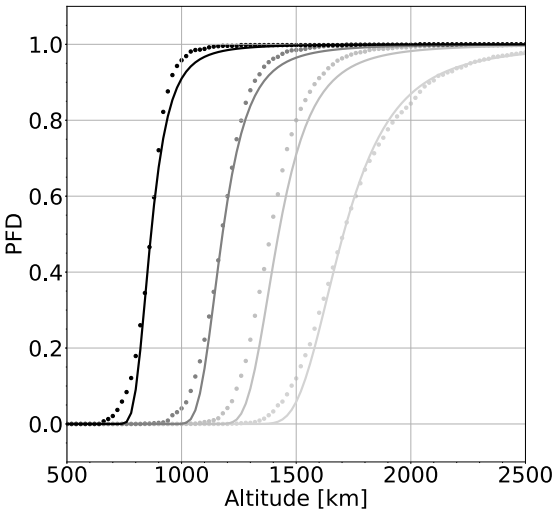

Figure 2.1: Single shot probability of false detection as a function of altitude for the albedo value 0.19. The PFD is given for four different slope angles, 0° (light gray), 10° (silver), 20° (dark gray) and 40° (black). The predicted PFD from the semi-analytical performance model (dashed lines) is compared against the PFD numerically derived from test data (bullets). To make the model comparable to the test results, the shot noise has to be removed (solid lines).

Using the same data set of noise measurements with

Parameter	**Symbol**	**Value**	**Unit**
Pulse energy	E_t	50	mJ
Wavelength	λ_T	1064	nm
Shot frequency	f	10	Hz
Pulse width (1-σ)	σ_0	2.2	ns
$1/e^2$ beam divergence (half cone)	θ_T	25	μrad
Telescope radius	r_R	10	cm
Field of view (half cone)	θ_R	247.5	μrad
Optical efficiency	ϵ_o	0.84	
Optical filter efficiency	ϵ_t	0.8	
Optical filter bandpass	σ_{rf}	2	nm
Quantum efficiency	ϵ_{qe}	0.30	
APD dark current (bulk)	I_{db}	100	pA
APD dark current (surface)	I_{ds}	100	nA
Noise floor	n_f	20	pA/$\sqrt{\text{Hz}}$
Nominal (maximum) gain	M	56 (113)	
Analog (TIA) bandwidth	B_0	20	MHz
TIA Resistance	R_i	51	kΩ
Sample resolution	τ_{adc}	12.5	ns

Table 2.1: BELA instrument parameters.

synthesized laser pulses as for the PFD, the range error of the instrument can be derived by a similar fit, giving

$$dz_i = 2 \cdot \exp\left(-\text{SNR}^{0.28}\right) + 0.1 \quad [\text{m}]. \tag{2.29}$$

For the range error evaluation of the return pulses only errors below the PFD threshold of 12.5 ns (digitization resolution) have been taken into account. Figure 2.2 visualizes the corresponding range error for the same set of surface slopes as a function of altitude. It should be noted that compared to the Cramer-Rao limit used in Gunderson et al. (2006) this leads to significantly different results. The Cramer-Rao ratio gives an upper limit to the range error measurement but underestimates the real performance of the filter matching algorithm. Instead it can be observed that the performance of the instrument is mainly PFD-driven, i.e. if the correct pulse is identified, then the range can usually be determined with an accuracy better than 2 m. At infinite SNR the range error converges towards the inherent range resolution of the instrument, which is 10 cm. Similarly, the relation between pulse width measurement accuracy and SNR can be approximated as

$$\delta_\sigma = 88.7 \exp\left(-\text{SNR}^{0.18}\right) + 11.78 \quad [\text{ns}]. \tag{2.30}$$

Since the detector of the laser altimeter integrates all returns over the footprint area, it is not possible to distinguish between surface slope and surface roughness within the laser footprint from one return pulse alone. Therefore, they are treated together and parametrized as a single value.

Gouman et al. (2015) used Mercury Laser Altimeter (MLA) data to statistically analyze the albedo distribution of Mercury at the laser wavelength and found that about 50% of the measured albedo values are exceeding 0.2 and that around 70% exceed 0.1. Inside dark craters the reflectance can further drop to around 0.05. The assumed average albedo in the following analysis is 0.19. The MPO spacecraft will be in an elliptical 400 $\times$ 1500 km orbit where the apoapsis is usually located on the illuminated side of Mercury due to thermal reasons. BELA is intended to operate up to at least 1050 km to assure global coverage. The coverage of the higher altitudes depends on the surface slope and albedo such that the effective limit is in a range between 800 km for very rough surfaces and an albedo around 0.2 and the apoapsis height for reasonably flat surfaces or higher albedo values. However, aside from the range error, a further significant error source is the limited knowledge of lateral position of the range measurement. It arises from the misalignment of the transmitter with respect to the inertial reference frame of the spacecraft and the resulting unknown pointing of the instrument. To verify the instrument alignment in orbit for the different thermal conditions during the mission, calibration campaigns will be carried out. Concepts for

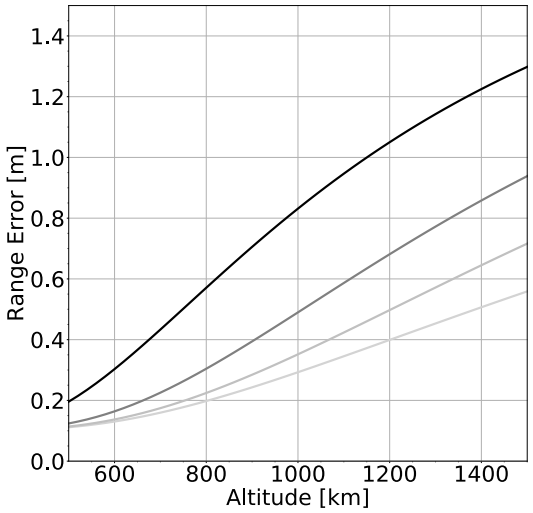

Figure 2.2: Range error as a function of altitude using the semi-analytical model for surface slopes of 0° (light gray), 10° (silver), 20° (dark gray) and 40° (black).

these have been studied in the frame of the BELA project and suggest alignment residuals of around 4 arcseconds (Stark et al., 2017a). The pointing knowledge of the spacecraft is assumed to be within 20 arcsec. On the surface the resulting total pointing error $d\phi$ translates to a topography measurement error $dz_p = H \tan(\theta_R) \tan(d\phi)$, with H being the spacecraft altitude. Other error sources, not explicitly considered in this study, are errors related to electronics and clock drifts. Since both signals, the transmitter as well as the receiver signal undergo the same electronic signal chain, we assume any electronic delays to cancel out. Further, clock drifts will be calibrated using an on board pulse per second signal and the calibration residual can be neglected for the purpose of this study.

2.3. Expected Science Performance

2.3.1. Topographic Coverage

The main science goal of BELA is to provide a global topographic elevation model of Mercury. The coverage and horizontal resolution on a global scale is mainly constrained by the spacecraft trajectory and the instrument performance in terms of PFD. For the projected resolution of a global elevation model we took all potential spots from two years of operation where the performance model returns a PFD $< 20\%$ (a value which is on the steep raising edge of the PFD curve). In this context we defined the horizontal resolution as the largest empty grid cell one can position on the surface. Thereby the grid is defined over a map in a sinusoidal projection of Mercury's surface but is visualized in equidistant projection with a resolution of $1° \times 1°$ (Figure 2.3). The horizontal resolution then varies from about 3 km at the equator down to less than 250 m at latitudes above 80° and below −80°. It is common to express the global resolution in terms of degree and order of a spherical harmonics expansion. This is achieved by subdividing the surface into single grid elements of the worst resolution, here 3×3 km in size. We then obtain $n \approx 2500$ grid elements. Expressed in a spherical harmonics expansion this corresponds to a maximum degree of $l_{\max} = (n-2)/2 \approx 1100$ but it should be noted that the assumed operation scenario is a best case scenario implying that BELA operates whenever performance permitting.

Due to the high number of laser profiles and SNR ratio at high- and mid-latitudes features such as lobate scarps or wrinkle ridges in these regions (e.g. Watters et al. (2015)) are expected to be mapped in good resolution. Further, many geologically interesting features like hollows are concentrated on the equatorial and mid latitudes which have only been mapped by laser altimetry in low horizontal resolution so far. Accurate profiles, however can help to calculate e.g. the associated volumes and outgassing rates. More accurate shape models of the planet allow better constraints on Mercury's crustal structure and the origin of the 3:2 resonance especially when studied in combination with gravity data. The regional topography in the northern high latitudes is dominated by smooth volcanic plains being less heavily cratered than the surroundings and containing a large number of buried craters (Head et al., 2011). So laser altimetry offers further the unique possibility to quantitatively study Mercury's morphology.

2.3.2. Slope and Roughness

As any planetary surface, the surface of Mercury is subject to modifications related to geological processes (impacts and internal processes) as well as erosion and degradation due to radiation and solar wind particles, which modify the surface on dif-

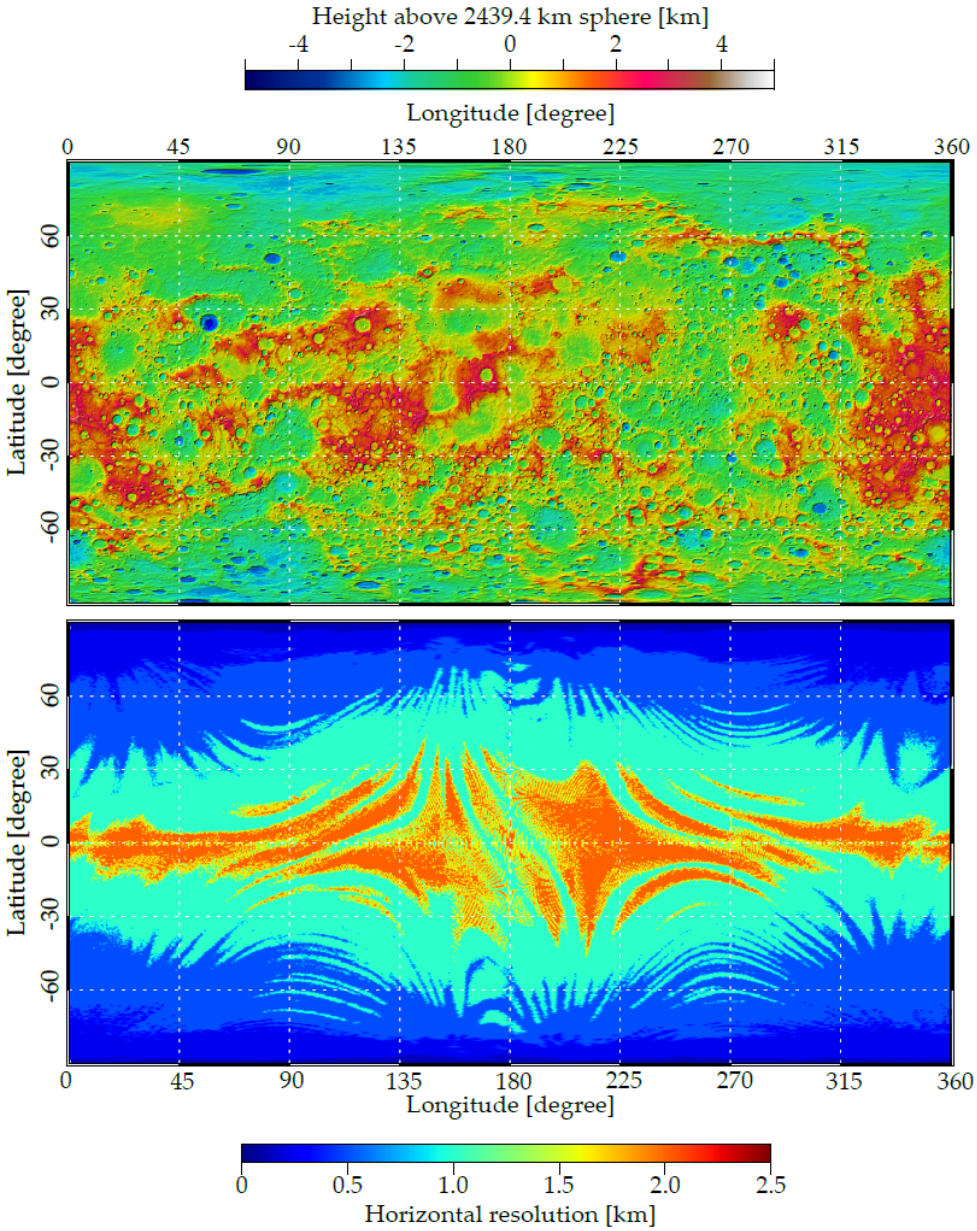

Figure 2.3: Top panel: Color-shaded relief of Mercury based on stereo images of the MESSENGER Mercury Dual Imaging System (Becker et al., 2016). Bottom panel: Topographic coverage after two years of BELA operation. The colors visualize the attainable local horizontal resolution.

ferent length scales. Data on surface roughness and its scale-dependence is an important clue for understanding surface processes in different (sometimes competing) regimes and their relative ages. The analysis of reflected laser pulses in combination with high along-track resolution of laser spots is an important method to characterize surface roughness on different length scales and to relate these measurements to specific geologic features and units. This has been successfully achieved with laser altimeter data in the case of Mars (Neumann et al., 2003), the Moon (Rosenburg et al., 2011; Kreslavsky et al., 2013) and Mercury (Yang et al., 2013; Kreslavsky et al., 2014). While global coverage could be achieved for the Moon and Mars, complete data-sets are still lacking for Mercury. Yang et al. (2013) have analyzed MLA data in the northern hemisphere noticing that the increased cross-track spacing towards lower latitudes (due to MESSENGER's elliptic polar orbit) may lead to bi-

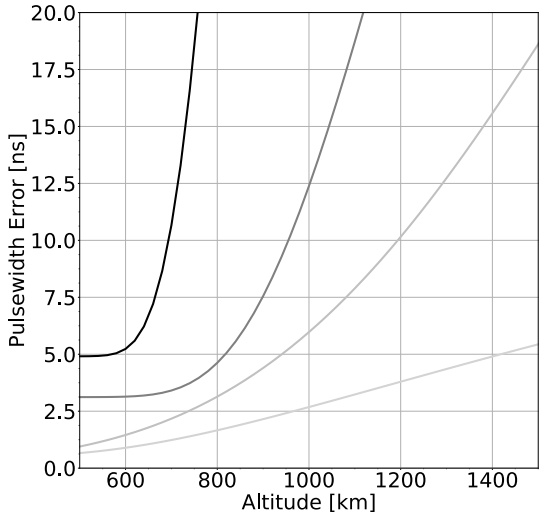

Figure 2.4: Accuracy of the return-pulse width measurement as a function of altitude. Shown is the estimated error of the reconstructed pulse compared to the return pulse sampled by the ADC (i.e. already broadened by the bandpass filter). The different colors represent different surface slopes of 0° (light gray), 10° (silver), 20° (dark gray) and 40° (black).

ased slopes and roughness, because the high resolution, with which along-track slopes can be determined, might not reflect the trends in longitudinal direction. Therefore, Kreslavsky et al. (2014) focused on the high-resolution data around Mercury's North-pole (between 65° and 84° N) only, covering 4.4% of Mercury's surface. The main results of these studies indicate basically a good correlation of surface roughness with geologic units. Topographic depressions turn out to be rather smooth, whereas highlands are heavily cratered and rougher at all baselines (Yang et al., 2013). An exception is an area of cratered low-lands at high northern latitude, which is significantly rougher than its surroundings. The northern smooth plains, a lowland region near the pole is smoother than its surrounding terrain and generally interpreted as a volcanic flow (Head et al., 2011).

By sampling and analyzing the digitized return pulse BELA will have the capability for determining the pulse shape including pulse broadening that is indicative of slope and roughness at the footprint scale of around 50 m. The accuracy of the roughness at footprint-scale can be estimated with Equation (2.30). By its filtering algorithms BELA is not limited to pure Gaussian shaped return pulses but can be adjusted by tele-commands to various families of filter functions, of which the best-fit parameters can be transmitted to the ground. The ability is limited however by the 20 MHz bandwidth. As expressed in Equation (2.14), the return pulse is not only broadened by the surface roughness but also by the analog bandpass filter. Therefore, the minimum width of any return pulse is σ_p, independently of the surface slope. The 20 MHz analog bandwidth is related to σ_p by Equation (2.13), leading to a respective σ_p of around 10 ns. Using Equation (2.14) this relates to an elevation difference of $\delta_z \approx$ 1.5 m. The broadening of the return pulse due to the surface slope further depends on the altitude. From higher altitudes, the footprint on the surface is larger, thus leading to a larger height difference within the footprint, when there is a slope. Therefore, the sensitivity to slopes increases with altitude. The MPO's periapsis is at 400 km. At this altitude the footprint is 20 m in diameter. Using Equation (2.7) we find that from 400 km altitude a δ_z of 1.5 m corresponds to a minimum slope angle of 10°. Slopes below this value will be difficult to distinguish. At the poles the altitude is 1050 km and the minimum measurable slope decreases to 4°. The minimum slope angle is best at apoapsis, i.e. 1500 km would correspond to 2.8°. However, at high altitudes the instrument capabilities to measure slopes are limited by the SNR, setting an upper maximum to slopes of around 15-20°. This value increases with decreasing altitude to 40° at $\approx$ 700 km (Figure 2.4). However, for larger slopes and reasonable SNR's the pulse width can be determined with an accuracy better than 5 ns corresponding to a slope (or equivalent rms roughness) of around 2° (Figure 2.4). The performance drops rapidly with decreasing SNR limiting reliable roughness measurements to low altitudes. On larger scales the high along-track resolution of 170 - 300 m will allow for correction of slopes at the various length-scales of interest. This capability is mainly PFD driven and therefore applicable also at higher altitudes. Furthermore, BELA will not be limited in coverage to the northern regions, which will yield invaluable data-sets for surface roughness globally, but also regionally and locally to be interpreted in combination with geologic units and surface evolution. As indicated by the examples above this will yield a deeper understanding of Mercury's surface evolution and the relative ages of events that have shaped the surface, both on regional and global scales.

2.4. Tidal Deformation

Due to its proximity to the Sun and its rather eccentric orbit, Mercury is exposed to significant tidal forces. The general form of the resulting degree 2 tidal potential is given as

$$V = \frac{GM_\odot^2 r^2}{d^3} P_2^0(\cos\phi), \tag{2.31}$$

with r being the distance from Mercury's center of mass and d the distance from the Sun which has the gravitational parameter $GM_\odot$. P_2^0 is the associated Legendre polynomial of degree 2 and order 0. Assuming that Mercury is on a Keplerian orbit, its trajectory can be described by the elements semi-major axis a, eccentricity e, inclination i, mean anomaly M, argument of periapsis ω, and longitude of ascending node Ω. Expressing the angle of the sub-Solar point ϕ in latitude θ and longitude λ the potential is often given as a series expansion in first order eccentricity. The resulting expression can be formulated as (Balogh and Giampieri, 2002):

$$\begin{aligned} V = &\frac{GMr^2}{8a^3}[12e\cos(M)P_2^0(\sin(\theta)) \\ &+ (e\cos(2M+2\lambda) \\ &- 2\cos(M+2\lambda))P_2^2(\sin(\theta))]. \end{aligned} \tag{2.32}$$

However, it should be noted that due to the high orbit eccentricity (≈ 0.205) the expansion up to first order is rather rough and yields residuals of around 15% even for a perfectly Keplerian orbit of Mercury. For the computation of the tidal potential it is therefore preferable to evaluate Equation (2.31) for each point in time. Note that static tides are usually removed when solving for the body-response but also cancel out in the cross-over approach used here (see below). The amplitudes of the response further depend on the material properties of the interior and are rather small for terrestrial planets. While MESSENGER determine Mercury's gravitational field up to order 50 and constrained the tidal Love number k_2 to 0.45 ± 0.02 (Mazarico et al., 2014b), as well as libration amplitude (Stark et al., 2015b), the radial response h_2 remains unknown at the time of this publication. Measuring Mercury's tidal amplitude would help interpret Mercury's surface geology, further constrain Mercury's core radius as well as the mantle rheology beyond the current constraints posed by k_2 and the observed librations.

2.4.1. Covariance Analysis

The MPO will be inserted into a polar orbit around Mercury and the ground tracks will intersect over time. These cross-over points can be used to extract the time dependent signal by a differential range measurement. Assuming a set of cross-over measurements we can obtain an estimate on h_2 using a least-squares inversion. The accuracy of the measurement of h_2 can be derived from a covariance analysis and is therefore dependent on two main components: the cross-over distribution and the mean measurement error. While the former is defined by the MPO orbit, the latter is driven by the instrument and spacecraft performance. The model used in this study to assess the performance of BELA is based on the performance model described in section 2.2. The number and distribution (in space and time) of cross-over points available for evaluation is driven by the mission lifetime and the operation scenario for the instrument. Simulations of the orbit determination using the radio science experiment MORE reports vertical error estimates of 1.80 m using a multifrequency link of X and Ka band (Marabucci, 2016) without including altimetry data. The combined along and cross track errors are estimated to be in the order of 5 m. The latter must be combined with the interpolation error dz_i, being a function of the spot to spot distance d and the surface slope ($dz_i = d\tan\theta_R$). At a shot frequency of 10 Hz and a typical slope on the scale of the spot to spot distance (see next section) the interpolation error is about 7-8 m. Therefore, the limited shot frequency and the resulting gaps between the footprints contribute the largest part of the total budget reported in table 2.2. The formal error in the h_2 estimation can then be assessed by a covariance analysis. In the here presented simple case the error can be computed directly as the sum over all cross-over points N. For the nominal mission lifetime N is in the order of 16 Mio, for the extended mission in the order of 60 Mio cross-over points.

$$\Delta h_2 = \sqrt{2\sum_i^N \frac{V_{i,1}(r,\theta,\lambda,t_{i,1}) - V_{i,2}(r,\theta,\lambda,t_{i,2})}{g}} \cdot dz \tag{2.33}$$

After the nominal operation time of one year this value is 7.0×10^{-3} and decreases to 3.2×10^{-3} at the end of the extended mission after two years assuming that all error distributions are Gaussian. However, due to the very high number of cross-over points we expect that non-Gaussian errors will dominate the measurement uncertainty. To identify the

critical sources we performed a numerical simulation of the measurement described in the following section.

2.4.2. Numerical Simulation

Most of the error sources affect the cross-over observable by causing an offset of the actual lateral position of the laser footprint with respect to the assumed location. As a consequence the uncertainty of the cross-over observable is driven by the roughness of the surface. To get a consolidated estimate for the accuracy of the tidal amplitude measurement it is therefore required to use an accurate roughness statistic. The scales of interest are the footprint size (around 50 m) and the spot to spot distance which is typically a couple of hundred meters. To compute the roughness at these baselines we used a digital terrain model (DTM) of the H6 (Kuiper) quadrangle derived from Mercury Dual Imaging System data (Preusker et al., 2017). To retrieve the respective roughness value at the baseline of interest we calculated the structure function (SF) which represents the mean height difference expected over a certain spatial distance τ (Shepard et al., 2001). It can be calculated for any given topography profile $z(x)$ as

$$S(\tau) = \lim_{L\to\infty} \frac{1}{L} \int_0^L |z(x) - z(x+\tau)|\, dx, \quad (2.34)$$

where L is the length of the profile and x is the distance from the starting point. The SF appears to follow a power law (Figure 2.5). Since no roughness information at the footprint size can be directly inferred from the data we extrapolated the SF to the relevant baselines. This results in a mean height difference of 12.1 m at the 200 m baseline and 6.4 m at the 50 m baseline.

A random RMS roughness value is chosen for each cross-over assuming a one-sided Gaussian distribution with a mean value of μ and corresponding to the extrapolated statistic at the respective baseline. The RMS height on a certain baseline is then given by $\delta = \sqrt{\frac{\pi}{2}}\mu$. This value is used for the pointing and alignment error, interpolation error and cross-track orbit errors. Further, we consider errors in the assumed rotational state of Mercury, which will result in an equivalent effect, causing differential horizontal offsets of the laser profiles. The reference rotation parameters used to simulate the ground truth are taken from Stark et al. (2015b). The errors for the spin axis, rotation rate and librations are generated using a covariance matrix are based

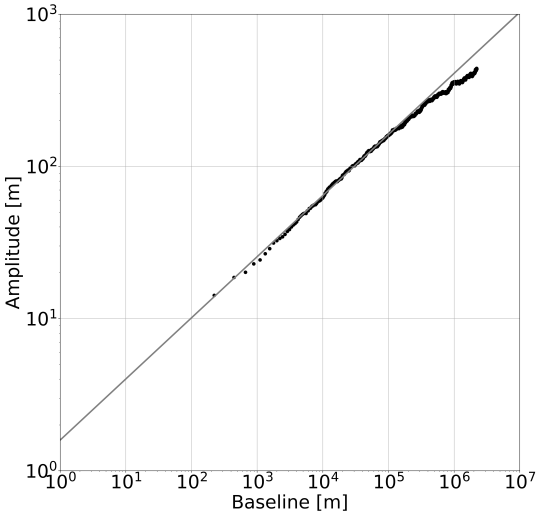

Figure 2.5: Structure Function of Mercury's surface as derived from stereo DTM data. The data points are derived from the quadrangle H6 (Preusker et al., 2017). The fit parameters of the line log(y)=a·log(x)+b are a=0.454 and b=0.371.

on Stark et al. (2015a). Following Mazarico et al. (2014a) or Steinbrügge et al. (2015), errors for each orbit n are modeled with random amplitude A and phase ϕ generated as

$$dr_n(t) = A_n \sin(\omega_n t + \phi_n) + C_n \quad (2.35)$$
$$= U_n \sin(\omega_n t) + V_n \cos(\omega_n t) + C_n, \quad (2.36)$$

where $U_n = A_n \cos(\phi_n)$ and $V_n = A_n \sin(\phi_n)$. For keeping internal consistency, we further require that the orbit corrections of consecutive orbits are continuous at the connecting points

$$dr_n(2\pi/\omega_n) = dr_{n+1}(0). \quad (2.37)$$

The total error due to the lack of knowledge on the rotational state is around 2 m i.e., smaller than the interpolation error, but introduces systematic errors, which in combination with the systematic nature of the orbit errors lead to a non-Gaussian error distribution. As a consequence the numerical error of the h_2 inversion increases despite of the fact that the linear nature of the problem is preserved.

Error source	**Value [m]**
Instrument	0.2
Pointing & alignment	9.5
Radial orbit errors	1.8
Rotational state	2.0
Interpolation errors	7.7
Sum	21.2
Quadratic sum	12.5

Table 2.2: Cross-over observable error budget calculated for a rms roughness of 12.1 m at 200 m baseline, 6.4 m at 50 m baseline and an albedo of 0.19.

The analysis suggests that h_2 cannot be reliably determined during the nominal mission lifetime given the small tidal amplitude ($\approx$ 20 cm for an $h_2 \approx 1$) in the polar regions combined with a high surface roughness. Also, with a shot frequency of 10 Hz, we obtain to severe errors in estimates of the cross-over location. Due to the slow rotation of Mercury, only very few cross-over points are available in the equatorial region where higher tidal amplitudes of around 2 m are expected. Fortunately, in the extended mission the total amount of available cross-over points increases from about 16 Mio to ca. 60 Mio and more low latitude points are available. The statistical result after 20 runs leads to in an error estimate for h_2 of 0.14 after 2 years, significantly higher than the initial covariance error. The standard deviation of the simulation results was 0.02.

2.5. Discussion

The updated performance model is a step towards a realistic description of digital laser altimeters using filter matching approaches instead of a classical threshold detection. In the description by Gunderson et al. (2006) and Gunderson and Thomas (2010) the calculation of the PFD as a function of SNR were limited by the assumption of a filter matching with a single template function. In effect the actual pulse fitting algorithm shows a much better performance than expected by a classical filter matching convolution. Nonetheless, this effect is counteracted to some extent by an increased noise level not expected from previous studies. However, the final instrument performance has been shown to be still well within the specification.

For the application of the instrument performance into orbital conditions around Mercury it should be noted that we assume the operation of BELA independently of any specific operation scenario. Currently, the baseline scenario foresees to limit operations to a maximum altitude of 1050 km. Respecting this restriction would lead to slightly worse coverage of the Hermean surface and therefore to slightly reduced horizontal resolution.

An important result of the simulated h_2 inversion is that the cross-over observable error budget is dominated by systematic errors while white noise is negligible due to the very high number of available cross-over points. The covariance analysis, which uses a too simplified model may be misleading. Any parallel solving for other parameters, like orbit, gravity field or rotational state of Mercury would increase this covariance error, but probably not change the error estimate of the numerical simulation since the error budget is heavily dominated by interpolation errors which come along with the 10 Hz shot frequency and the resulting spacing between the footprints.

The main difficulty in measuring Mercury's radial tidal deformation is the unequal distribution of cross-over points heavily biased towards the poles. Even if this is a natural consequence of a polar orbit, the slow rotation rate of Mercury leads to a very low number of cross-over points at lower latitudes and since the tidal amplitudes at the poles are very small, measuring tides can be a significant challenge.

An alternative method to circumvent this situation might be to infer h_2 by separating the static and dynamic topography from a spherical harmonics expansion (Koch et al., 2008, 2010). However, this method requires a very good surface coverage to detect such small changes in the topography and is very sensitive to any systematic errors. Nonetheless, the expected accuracy of 0.14 is a valuable geodetic constraint which might in combination with the already available observations put better constraints on Mercury's interior structure. The determination of h_2 allows for better constraints on the core size and the density as well as the rheology of the mantle. Further, other improvements might lead to a better h_2 determination, e.g. a better performance or reconstruction of the pointing including which currently contributes the highest value on the errors.

2.6. Conclusion

This study proposes a modified performance model for BepiColombo's BELA instrument, based on BELA flight model tests. The performance model may be generalized and used for performance assessment of other digital laser altimeter experiments as well. It has been shown that the PFD effects are not treated propperly in previous work but can be well fitted by an empirical relation and that the instrument performance is much better than originally estimated at a given SNR. In orbit, BELA will achieve a global coverage of Mercury with maximum gaps of 3 km between the ground tracks after two years of operations. However, when measuring Mercury's tidal amplitude there are three major challenges to overcome: First, due to the slow rotation of Mercury, only cross-over points at the polar regions will be available for measurements of tidal effects. Second, the shot frequency of 10 Hz leads to interpolation errors in rough terrain, higher than the expected tidal amplitude requiring direct studies on predominantly flat areas. And last, since measurements are concentrated at the poles during the nominal mission lifetime, an extended mission will be necessary to reliably determine h_2. In that case, the quadratic growth of the number of cross-over points over time leads to significantly improved statistics on one hand and allows for more cross-over points at lower latitudes on the other hand. After two years of operation we estimate that h_2 can be measured with an absolute accuracy of 0.14.

Acknowledgments

The authors would like to thank Urs Geissbüler for, Alain Peteut, Seyedalireza Hosseiniarani, Karsten Seiferlin and Nicolas Thomas for their support and helpful discussions. We thank two anonymous reviewers for a constructive review which helped to improve this contribution. A. Stark was supported by a research grant from the Helmholtz Association and German Aerospace Center (DLR).

References

Abshire, J.B., Sun, X., Afzal, R.S.. Mars Orbiter Laser Altimeter: receiver model and performance analysis. Appl Opt 2000;39(15):2449–2460. doi:10.1364/AO.39.002449.

Balogh, A., Giampieri, G.. Mercury: the planet and its orbit. Reports on Progress in Physics 2002;65(4):529.

Becker, K.J., Robinson, M.S., Becker, T.L., Weller, L.A., Edmundson, K.L., Neumann, G.A., Perry, M.E., Solomon, S.C.. First global digital elevation model of Mercury. 2016.

Benkhoff, J., van Casteren, J., Hayakawa, H., Fujimoto, M., Laakso, H., Novara, M., Ferri, P., Middleton, H.R., Ziethe, R.. BepiColombo-Comprehensive exploration of Mercury: Mission overview and science goals . Planetary and Space Science 2010;58(1-2):2 – 20. doi:10.1016/j.pss.2009.09.020.

Cavanaugh, J.F., Smith, J.C., Sun, X., Bartels, A.E., Krebs, D.J., McGarry, J.F., Trunzo, R., Novo-Gradac, A.M., Britt, J.L., Karsh, J., Katz, R.B., Lukemire, A.T., Szymkiewicz, R., Berry, D.L., Swinski, J.P., Neumann, G.A., Zuber, M.T., Smith, D.E.. The Mercury Laser Altimeter Instrument for the MESSENGER Mission. Space Science Reviews 2007;131(1):451–479. doi:10.1007/s11214-007-9273-4.

Gardner, C.. "Ranging Performance of Satellite Laser Altimeters". "IEEE Transactions on Geoscience and Remote Sensing" 1992;30 No 5:1061–1072. doi:10.1109/36.175341.

Gouman, J., Beck, T., Affolter, M., Thomas, N., Geissbühler, U., Peteut, A., Bandy, T., Servonet, A., Piazza, D., Seiferlin, K., Ghose, K.. Measurement and stability of the pointing of the BepiColombo Laser Altimeter under thermal load . Acta Astronautica 2014;105(1):171 – 180. doi:10.1016/j.actaastro.2014.09.006.

Gouman, J., Pommerol, A., Thomas, N.. Propoerties of the Surface of Mercury from MESSENGER Laser Altimeter Data and their consequences on the BepiColombo Laser Altimeter Performance. 2015. 46th Lunar and Planetary Science Conference, Abstract 1959.

Gunderson, K., Thomas, N.. BELA receiver performance modeling over the BepiColombo mission lifetime. Planetary and Space Science 2010;58:309–318. doi:10.1016/j.pss.2009.08.006.

Gunderson, K., Thomas, N., Rohner, M.. A laser altimeter performance model and its application to BELA. "IEEE Transactions on Geoscience and Remote Sensing" 2006;44 No 11:3308–3319. doi:10.1109/tgrs.2006.880623.

Hapke, B.. Bidirectional reflectance spectroscopy: 1. theory. Journal of Geophysical Research: Solid Earth 1981;86(B4):3039–3054. doi:10.1029/JB086iB04p03039.

Head, J.W., Chapman, C.R., Strom, R.G., Fassett, C.I., Denevi, B.W., Blewett, D.T., Ernst, C.M., Watters, T.R., Solomon, S.C., Murchie, S.L., Prockter, L.M., Chabot, N.L., Gillis-Davis, J.J., Whitten, J.L., Goudge, T.A., Baker, D.M.H., Hurwitz, D.M., Ostrach, L.R., Xiao, Z., Merline, W.J., Kerber, L., Dickson, J.L., Oberst, J., Byrne, P.K., Klimczak, C., Nittler, L.R.. Flood Volcanism in the Northern High Latitudes of Mercury Revealed by MESSENGER. Science 2011;333(6051):1853–1856. doi:10.1126/science.1211997.

Kallenbach, R., Behnke, T., Perplies, H., Henkelmann, R., Rech, M., Geissbühler, U., Peteut, A., Lichopoj, A., Schroedter, R., Michaelis, H., Seiferlin, K., Thomas, N., Castro, J.M., Herranz, M., Lara, L.. Electromagnetic compatibility of transmitter, receiver, and communication port of a space-qualified laser altimeter. 2016 ESA Workshop on Aerospace EMC (Aerospace EMC) 2016;:1–7.

Koch, C., Christensen, U., Kallenbach, R.. Simultaneous determination of global topography, tidal Love number and libration amplitude of Mercury by laser altimetry. Planetary and Space Science 2008;56(9):1226 – 1237. doi:10.1016/j.pss.2008.04.002.

Koch, C., Kallenbach, R., Christensen, U.. Mercury's global topography and tidal signal from laser altimetry by using a rectangular grid. Planetary and Space Science 2010;58(14):2022 – 2030. doi:10.1016/j.pss.2010.10.002.

Kreslavsky, M.A., Head, J.W., Neumann, G.A., Rosenburg, M.A., Aharonson, O., Smith, D.E., Zuber, M.T.. Lunar topographic roughness maps from Lunar Orbiter Laser Altimeter (LOLA) data: Scale dependence and correlation with geologic features and units. Icarus 2013;226(1):52 – 66. doi:10.1016/j.icarus.2013.04.027.

Kreslavsky, M.A., Head, J.W., Neumann, G.A., Zuber, M.T., Smith, D.E.. Kilometer-scale topographic roughness of mercury: Correlation with geologic features and units. Geophysical Research Letters 2014;41(23):8245–8251. doi:10.1002/2014GL062162.

Marabucci, M.. The Determination of the Hermean Gravity and Topography from Radio Science and Laser Altimeter Data of the Mission BepiColombo. 2016. PhD Thesis.

Margot, J.L., Peale, S.J., Jurgens, R.F., Slade, M.A., Holin, I.V.. Large longitude libration of mercury reveals a molten core. Science 2007;316(5825):710–714. doi:10.1126/science.1140514.

Mazarico, E., Barker, M., Neumann, G., Zuber, M., Smith, D.. Detection of the lunar body tide by the Lunar Orbiter Laser Altimeter. Geophysical Research Letters 2014a;41. doi:10.1002/2013GL059085.

Mazarico, E., Genova, A., Goossens, S., Lemoine, F.G., Neumann, G.A., Zuber, M.T., Smith, D.E., Solomon, S.C.. The gravity field, orientation, and ephemeris of Mercury from MESSENGER observations after three years in orbit. Journal of Geophysical Research: Planets 2014b;119(12):2417–2436. doi:10.1002/2014JE004675.

Neumann, G.A., Abshire, J.B., Aharonson, O., Garvin, J.B., Sun, X., Zuber, M.T.. Mars orbiter laser altimeter pulse width measurements and footprint-scale roughness. Geophysical Research Letters 2003;30(11):1561. doi:10.1029/2003GL017048; 1561.

Preusker, F., Stark, A., Oberst, J., Matz, K.D., Gwinner, K., Roatsch, T., Watters, T.R.. "Toward high-resolution global topography of Mercury from MESSENGER orbital stereo imaging: A prototype model for the H6 (Kuiper) quadrangle. Planetary and Space Science 2017;142:26 – 37. doi:10.1016/j.pss.2017.04.012.

Rosenburg, M.A., Aharonson, O., Head, J.W., Kreslavsky, M.A., Mazarico, E., Neumann, G.A., Smith, D.E., Torrence, M.H., Zuber, M.T.. Global surface slopes and roughness of the moon from the lunar orbiter laser altimeter. Journal of Geophysical Research: Planets 2011;116(E2). doi:10.1029/2010JE003716.

Shepard, M.K., Campbell, B.A., Bulmer, M.H., Farr, T.G., Gaddis, L.R., Plaut, J.J.. The roughness of natural terrain: A planetary and remote sensing perspective. Journal of Geophysical Research: Planets 2001;106(E12):32777–32795. doi:10.1029/2000JE001429.

Solomon, S.C., McNutt Jr, R.L., Prockter, L.M.. Mercury after the {MESSENGER} flybys: An introduction to the special issue of planetary and space science. Planetary and Space Science

2011;59(15):1827 – 1828. doi:10.1016/j.pss.2011.08.004.

Stark, A., Hussmann, H., Steinbrügge, G., Gläser, P., Gwinner, K., Oberst, J., Casasco, M., Cremonese, G.. In-flight alignment calibration between a laser altimeter and an imaging system - Application to the BepiColombo mission. 2017. EGU General Assemply 2017, Abstract 8364.

Stark, A., Oberst, J., Hussmann, H.. Mercury's resonant rotation from secular orbital elements. Celestial Mechanics and Dynamical Astronomy 2015a;123(3):263–277. doi:10.1007/s10569-015-9633-4.

Stark, A., Oberst, J., Preusker, F., Peale, S.J., Margot, J.L., Phillips, R.J., Neumann, G.A., Smith, D.E., Zuber, M.T., Solomon, S.C.. First MESSENGER orbital observations of Mercury's librations. Geophysical Research Letters 2015b;42(19):7881–7889. doi:10.1002/2015GL065152.

Steinbrügge, G., Stark, A., Hussmann, H., Sohl, F., Oberst, J.. Measuring tidal deformations by laser altimetry. A performance model for the Ganymede Laser Altimeter . Planetary and Space Science 2015;117:184 – 191. doi:10.1016/j.pss.2015.06.013.

Thomas, N., Spohn, T., Barriot, J.P., Benz, W., Beutler, G., Christensen, U., Dehant, V., Fallnich, C., Giardini, D., Groussin, O., Gunderson, K., Hauber, E., Hilchenbach, M., Iess, L., Lamy, P., Lara, L.M., Logonne, P., Lopez-Moreno, J., Michaelis, H., Oberst, J., Resendes, D., Reynaud, J.L., Rodrigro, R., Sasaki, S., Seiferlin, K., Wieczorek, M., Whitby, J.. The BepiColombo Laser Altimeter (BELA): Concept and baseline design. Planetary and Space Science 2007;55:1398–1413. doi:10.1016/j.pss.2007.03.003.

Verma, A.K., Margot, J.L.. Mercury's gravity, tides, and spin from MESSENGER radio science data. Journal of Geophysical Research: Planets 2016;121(9):1627–1640. doi:10.1002/2016JE005037.

Watters, T.R., Selvans, M.M., Banks, M.E., Hauck, S.A., Becker, K.J., Robinson, M.S.. Distribution of large-scale contractional tectonic landforms on Mercury: Implications for the origin of global stresses. Geophysical Research Letters 2015;42(10):3755–3763. doi:10.1002/2015GL063570.

Wehrli, C.. Extraterrestrial Solar Spectrum. 1985. Publication no. 615, Physikalisch-Meteorologisches Observatorium + World Radiation Center (PMO/WRC) Davos Dorf, Switzerland.

Yang, D., Zuber, M.T., Head, J.W., Solomon, S.C.. Distribution of topographic slope and roughness in Mercury's Northern hemisphere. 2013. 44th Lunar and Planetary Science Conference, Abstract 1719.

Zuber, M.T., Smith, D.E., Solomon, S.C., Muhleman, D.O., Head, J.W., Garvin, J.B., Abshire, J.B., Bufton, J.L.. The Mars Observer laser altimeter investigation. Journal of Geophysical Research 1992;97(E5):7781–7797. doi:10.1029/92JE00341.

Chapter 3

Research Paper II

Viscoelastic Tides of Mercury and the Determination of its Inner Core Size

G. Steinbrügge[1], S. Padovan[1], H. Hussmann[1], T. Steinke[2], A. Stark[1], J. Oberst[1]

[1]German Aerospace Center, Institute of Planetary Research, D-12489 Berlin, Germany
[2]Delft University of Technology, Delft, The Netherlands

Preprint submitted for publication in JGR-Planets

Abstract

We computed interior structure models of Mercury and analyzed their viscoelastic tidal response. The models are consistent with MErcury Surface, Space Environment, GEochemistry and Ranging (MESSENGER) mission inferences of mean density, mean moment of inertia, moment of inertia of mantle and crust, and tidal Love number k_2. Based on these constraints we estimate the tidal Love number h_2 to be in the range from 0.77 to 0.93. The tidal phase-lag is estimated to be 4° at maximum. The corresponding tidal dissipation in Mercury's silicate mantle induces a surface heat flux smaller than 0.16 mW/m^2. We show that for inner cores above 700 km in radius, the size can be constrained by using the ratio of the tidal Love numbers k_2 derived by past and upcoming radio science measurements and h_2 to be derived from future BepiColombo laser altimeter measurements. The h_2/k_2 ratio provides a better constraint on the maximum inner core size with respect to other geodetic parameters (e.g. librations or a single Love number). The measurement of the tidal phase-lag with an accuracy better than $\approx 0.5°$ would further allow constraining the temperature at the core-mantle boundary and therefore improve our understanding of the physical structure of Mercury's core.

3.1. Introduction

From 2011 to 2015, NASA's MErcury Surface, Space Environment, GEochemistry and Ranging (MESSENGER) spacecraft (Solomon et al., 2011) orbited Mercury and was able to provide, in combination with Earth-based radar measurements, a set of geodetic constraints on the interior structure of the planet. Mercury's mean radius of (2439.36 ± 0.02) km (Perry et al., 2015) in combination with the gravitational parameter GM of (2.203209 ± 0.000091)×10^{13} m/s^2 (Verma and Margot, 2016) leads to a mean density of 5427.75 kg/m^3. This high value in combination with Mercury's size indicates a significant fraction of iron in Mercury's composition. The mean moment of inertia has been first determined by ground-based radar observations of Mercury's spin state to a value of $C/MR^2 = 0.346$ ± 0.014 (Margot et al., 2007). With updated values for the gravity field inferred from MESSENGER radio science observations, a value of 0.349 ± 0.014 was found (Mazarico et al., 2014b). The measurement of the physical librations at the 88 days orbital period using laser altimetry and stereo imaging data gave a value of 0.343 ± 0.014 (Stark et al., 2015b; Baland et al., 2017). A value smaller than 0.4 indicates a concentration of mass towards the center of the planet, thus indicating the abundant iron is likely concentrated in a large core. In the Cassini state, a combination of libration amplitudes, gravitational field, and obliquity provides an estimate of the moment of inertia of the mantle and crust (Peale, 1976b; Peale et al., 2002). The determined values range between 0.431 ± 0.025 (Margot et al., 2012) and 0.421 ± 0.021 (Stark et al., 2015b), revealing an at least partially molten core (Margot et al., 2007; Margot et al., 2012; Stark et al., 2015b; Hauck et al., 2013). Further constraints come from the measurement of Mercury's tidal Love number k_2. The value indicates the intensity of the generated gravitational potential due to an internal redistribution of mass. This redistribution is a consequence of the tidal forcing that is exerted by the Sun during Mercury's orbit. k_2 has been determined to be 0.451 ± 0.014 by Mazarico et al. (2014b) and 0.464 ± 0.023 by Verma and Margot (2016). Based on the k_2 determination of Mazarico et al. (2014a), Padovan et al. (2014) examined multiple interior models in agreement with the measurement. The authors showed that in presence of a liquid core with known size, k_2 is informative with regard to the mantle properties. They inferred a cold and / or rigid mantle and further concluded that the presence of a previously suggested solid FeS layer (Malavergne et al., 2010; Smith et al., 2012) is only consistent with the measurements when the temperature at the core mantle boundary (CMB) is < 1600 K.

The core generates a weak magnetic field with an unusually large quadropole moment (Anderson et al., 2012). Possible origins are the classical dynamo model (Manglik et al., 2010; Cao et al., 2014) but also alternative models involving snow formation dynamics have been proposed (Dumberry and Rivoldini, 2015). Independent of the model assumed, a key factor of the magnetic field generation models is the presence and, if it exists, the size of the inner solid inner core. This work studies the tidal deformation of Mercury based on the geodetic constraints from the MESSENGER mission and shows that a future determination of the tidal Love number h_2 can yield important constraints on the inner core size, when combined with the available (or future) measurements of k_2. We further study the potential range of tidal phase-lags and resulting tidal heat dissipation in Mercury's mantle. All the geodetic parameters discussed in this paper are expected to be measured by the upcoming BepiColombo mission (Benkhoff et al., 2010) scheduled for launch in October 2018 and operated by the European Space Agency (ESA) and the Japan Aerospace Exploration Agency (JAXA).

3.2. Methods

The constructed interior structure models consist of three chemically separated layers: a core surrounded by a mantle and a crust. While the crust is kept as one single layer, mantle and core are further subdivided into 5 and 20 layers, respectively. Each sublayer is characterized by its thickness, density, temperature, pressure, viscosity and rigidity. It should be noted that unlike previous work (e.g. Hauck et al. (2013); Knibbe and van Westrenen (2015)) this work does not aim at randomly generating the models to create a probabilistic distribution. Instead we sweep through the parameter space (defined below) in an equally spaced grid without giving preference to any of the models as long as they are in agreement with the geodetic constraints. The parameter space is spanned by the 3-σ error interval of the measured geodetic constraints, the amount of light iron-alloying components in the core, where we account for sulfur and silicon, the CMB temperature, as well as by the crustal thickness and density. The remaining parameters, i.e. the outer core radius and reference density as well as the mantle

density are solved-for.
The construction of the models follows a two-step approach. In a first step each model is initialized by a given set of values from the structural and compositional parameters listed above, i.e. crustal thickness and density, sulfur and silicon content in the core, and the CMB temperature. The initial crust parameters are varied between thicknesses of 10 and 40 km with a step size of 2 km and densities between 2600 and 4000 kg/m^3. The density step size is 10 kg/m^3. The sulfur content of the core is assumed to be between 0 and 14%, varied with a step size of 1%. The silicon content of the core is varied between 0 and 26% in a step size of 2%. The temperature at the core mantle boundary is initially assumed to be between 1400 K for a cold mantle and 2000 K representing a very hot mantle. The step size is 10 K.
These values are then combined with a set of the three geodetic constraints, namely the mean density (ρ), the mean moment of inertia (MoI) and the fractional part of the moment of inertia of the mantle (C_m/C) to solve for the radius of the outer core R_c, the reference liquid core density ρ_0 as well as for the mantle density ρ_m.
For the geodetic constraints we consider values within the 3-σ error bar. The nominal value used for k_2 is 0.464 ± 0.023 (Verma and Margot, 2016) but the 3-σ error bar includes the value determined by Mazarico et al. (2014b). The used mean moment of inertia is 0.346 ± 0.014 and has been taken from Margot et al. (2012) but is consistent with the value derived by Stark et al. (2015b). The assumed C_m/C value is 0.421 ± 0.025 and taken from Stark et al. (2015b). However, within the used error intervals the C_m/C is also consistent with the value 0.431 ± 0.021 determined by Margot et al. (2012).
A solution is only considered valid if the resulting model is hydrostatic and if the solved core reference density is consistent with laboratory measurements as listed in Table 3.1.
In the second step each solution for the structural model is provided with a set of different mantle rheologies, parameterized by the unrelaxed rigidity and the grain size. For the unrelaxed mantle rheology we use values between 59 GPa and 71 GPa and a stepsize of 2 GPa. The grain size is varied between 1 mm and 1.2 cm with a step size of 2 mm. Based on these, the tidal Love number k_2 is calculated and compared against the measurement. Models which are not consistent with the measurement inside its 3-σ error bar are discarded.
The two steps - structural and rheological model - are then repeated with different values for the initial conditions as well as for different geodetic constraints consistent within the respective measurement error bars.

3.2.1. Structural Models

For each set of parameters, the models are built from outside to inside and generally follow the recipe from previous studies (e.g. Hauck et al. (2007, 2013); Knibbe and van Westrenen (2015)). Assuming the densities in the mantle and crust to be constant, we compute the pressure and gravitational acceleration at the CMB. From there on, pressure and temperature of the core are propagated inwards satisfying Equations (3.1) - (3.5). Equation (3.1) is a third-order Birch-Murnaghan equation of state giving the pressure P at radius r as a function of density ρ and temperature T

$$\begin{aligned} P(r) &= \frac{3K_0}{2}\left[\left(\frac{\rho}{\rho_0}\right)^{7/3} - \left(\frac{\rho}{\rho_0}\right)^{5/3}\right] \\ &\quad \cdot \left[1 + \frac{3}{4}(K_0' - 4)\left(\left(\frac{\rho}{\rho_0}\right)^{2/3} - 1\right)\right] \\ &\quad + \alpha_0 K_0 (T(r) - T_0). \end{aligned} \tag{3.1}$$

T_0, ρ_0, K_0, K_0' and α_0 are the local reference temperature, density, isothermal bulk modulus as well its pressure derivative and the reference volumetric coefficient of thermal expansion, respectively. A list of all parameters used to calculate the properties of the core in this study can be found in Table 3.1.
The pressure can be calculated from the overlaying layers by integrating from the outer radius R down to the current radius r.

$$P(r) = \int_R^r \rho(x) g(x) dx \tag{3.2}$$

The function g denotes the gravitational acceleration of each layer and can be calculated by

$$g(r) = \frac{4\pi G}{r^2} \int_0^r \rho(x) g(x) x^2 dx. \tag{3.3}$$

The adiabatic temperature profile in the core is obtained by integration of the adiabatic relation

$$\frac{dT}{dP} = \frac{\alpha T}{\rho C_p}, \tag{3.4}$$

where C_p is the thermal heat capacity and α the thermal expansion coefficient which can be obtained from

$$\alpha_0 K_0 = \alpha \rho \frac{dP}{d\rho}. \tag{3.5}$$

In this work we use a thermal heat capacity for the core of 825 J/(kgK) (Beutl et al., 1994; Knibbe and

Solid Core			
Parameter	**Value**	**Unit**	**Source**
$T_{0,\mathrm{Fe}}$	298	K	Komabayashi and Fei (2010)
$\rho_{0,\mathrm{Fe}}$	8170	kg m^{-3}	Komabayashi and Fei (2010)
$K_{0,\mathrm{Fe}}$	165.3	GPa	Komabayashi and Fei (2010)
$K'_{0,\mathrm{Fe}}$	5.5	-	Komabayashi and Fei (2010)
$\alpha_{0,\mathrm{Fe}}$	6.4×10^{-5}	K^{-1}	Komabayashi and Fei (2010)
$T_{0,\mathrm{Fe3S}}$	293	K	Fei et al. (2000)
$\rho_{0,\mathrm{Fe3S}}$	7033	kg m^{-3}	Fei et al. (2000)
$K_{0,\mathrm{Fe3S}}$	150	GPa	Fei et al. (2000)
$K'_{0,\mathrm{Fe3S}}$	4	-	Fei et al. (2000)
$\alpha_{0,\mathrm{Fe3S}}$	6.4×10^{-5}	K^{-1}	Fei et al. (2000)
$T_{0,\mathrm{Fe-Si(17wt\%)}}$	300	K	Lin et al. (2003)
$\rho_{0,\mathrm{Fe-Si(17wt\%)}}$	7147	kg m^{-3}	Lin et al. (2003)
$K_{0,\mathrm{Fe-Si(17wt\%)}}$	141	GPa	Lin et al. (2003)
$K'_{0,\mathrm{Fe-Si(17wt\%)}}$	5.7	-	Lin et al. (2003)
$\alpha_{0,\mathrm{Fe-Si(17wt\%)}}$	5.5×10^{-5}	K^{-1}	Uchida et al. (2001), Lin et al. (2003)
Liquid Core			
Parameter	**Value**	**Unit**	**Reference**
$T_{0,\mathrm{Fe-Si(17wt\%)}}$	1650	K	Sanloup et al. (2004)
$\rho_{0,\mathrm{Fe-Si(17wt\%)}}$	6300	kg m^{-3}	Sanloup et al. (2004)
$K_{0,\mathrm{Fe-Si(17wt\%)}}$	79	GPa	Sanloup et al. (2004)
$K'_{0,\mathrm{Fe-Si(17wt\%)}}$	4	-	Sanloup et al. (2004)
$\alpha_{0,\mathrm{Fe-Si(17wt\%)}}$	9.2×10^{-5}	K^{-1}	Sanloup et al. (2004)
$T_{0,\mathrm{FeS}}$	1770	K	Knibbe and van Westrenen (2015),Sanloup et al. (2000)
$\rho_{0,\mathrm{FeS},a}$	31524	kg m^{-3}	Knibbe and van Westrenen (2015),Sanloup et al. (2000),Jing et al. (2014)
$\rho_{0,\mathrm{FeS},b}$	-20012	kg m^{-3}	Knibbe and van Westrenen (2015),Sanloup et al. (2000),Jing et al. (2014)
$\rho_{0,\mathrm{FeS},c}$	7019	kg m^{-3}	Knibbe and van Westrenen (2015),Sanloup et al. (2000),Jing et al. (2014)
$K_{0,\mathrm{FeS},a}$	780.8	GPa	Knibbe and van Westrenen (2015),Sanloup et al. (2000),Jing et al. (2014)
$K_{0,\mathrm{FeS},b}$	-462.4	GPa	Knibbe and van Westrenen (2015),Sanloup et al. (2000),Jing et al. (2014)
$K_{0,\mathrm{FeS},c}$	86.6	GPa	Knibbe and van Westrenen (2015),Sanloup et al. (2000),Jing et al. (2014)
$K'_{0,\mathrm{FeS}}$	5.1	-	Knibbe and van Westrenen (2015),Sanloup et al. (2000),Jing et al. (2014)
$\alpha_{0,\mathrm{Fe3S}}$	9.2×10^{-5}	K^{-1}	Knibbe and van Westrenen (2015),Sanloup et al. (2000),Jing et al. (2014)

Table 3.1: Parameters derived from laboratory measurements used for the computation of the interior structure of Mercury's liquid and solid core.

van Westrenen, 2015). By performing the inwards propagation the problem reduces to solving Equations (3.1), (3.4) and (3.5). These are solved simultaneously for the density ρ at the given depth, the temperature T, and the coefficient of thermal expansion α using a Levenberg-Marquardt algorithm (Levenberg, 1944; Marquardt, 1963) to allow for self-consistent core models. For models with mixed Fe-FeS-FeSi composition, the parameters in Equation (3.1) - (3.5) are linearly interpolated from the values given in Table 3.1. The bulk modulus of sulfur is quadratically interpolated as

$$K_{0,\mathrm{FeS}} = K_{0,\mathrm{FeS},a} \cdot \chi_S^2 + K_{0,\mathrm{FeS},b} \cdot \chi_S + K_{0,\mathrm{FeS},c}^2. \quad (3.6)$$

At each sublayer the liquidus for the respective sulfur and silicon content is checked and if the temperature is lower than the melting temperature at the corresponding pressure, the state of the core is switched from liquid to solid. The parametrization for the liquidus of a sulfur-enriched Fe core is taken from Dumberry and Rivoldini (2015) and modified according to Knibbe and van Westrenen (2015) to account for the further decrease of the melting temperature due to the Si content. The melting temperature of the Fe-S-Si system is then described as a function of pressure P, sulfur content χ_{S}, and silicon content χ_{Si} as:

$$\begin{aligned} T_m(P, \chi_{\mathrm{S}}, \chi_{\mathrm{Si}}) &= T_{m,\mathrm{Fe}}(P) \\ &- \frac{T_{m,\mathrm{Fe}}(P) - T_{e_{\mathrm{S}}}(P)}{\chi_{e_S}} \chi_{\mathrm{S}} \\ &- \frac{T_{m,\mathrm{Fe}}(P) - T_{e_{\mathrm{Si}}}(P)}{\chi_{e_{\mathrm{Si}}}} \chi_{\mathrm{Si}}. \end{aligned} \quad (3.7)$$

$T_{m,\mathrm{Fe}}$ is the melting temperature of pure iron which is parameterized as a function of pressure by

$$T_{m,\mathrm{Fe}}(P) = a_1 (P_0 + P)^{a_2}, \quad (3.8)$$

with $a_1 = 495.5$ K GPa^{-a2}, a_2=0.42 and $P_0 = 22.2$ GPa (Dumberry and Rivoldini, 2015). In Equation (3.7), $T_{e_{\mathrm{S}}}$ and $T_{e_{\mathrm{Si}}}$ are the eutectic temperatures of the Fe-S sytem with sulfur content $\chi_{e_{\mathrm{S}}}$ and the Fe-Si system with the silicon content $\chi_{e_{\mathrm{Si}}}$, respectively. While the Fe-S system is parameterized as a

function of pressure,

$$T_{e_S}(P) = \begin{cases} 1265\text{K} - 11.15(P - 3\text{GPa})\text{K/GPa} \\ \text{for 3 GPa} \leq \text{P} < 14 \text{ GPa} \\ \\ 1143\text{K} - 29(P - 14\text{GPa})\text{K/GPa} \\ \text{for 14 GPa} \leq \text{P} < 21 \text{ GPa} \\ \\ 1346\text{K} - 13(P - 21\text{GPa})\text{K/GPa} \\ \text{for 21 GPa} \leq \text{P} < 60 \text{ GPa} \end{cases} \tag{3.9}$$

and

$$\chi_{e_S} = 0.11 + 0.187 \exp\left(-\frac{0.065P}{\text{GPa}}\right), \tag{3.10}$$

no information about the eutectic temperature as a function of pressure is available from experimental data. We therefore follow the approach of Knibbe and van Westrenen (2015) and use $T_{m,\text{Fe}}(P) - T_{e_{\text{Si}}}$ = 400 K at 0.26 wt.% Si based on the lab measurements from Kuwayama and Hirose (2004).

The inner core is assumed isothermal and to have an Fe-Si alloy composition with a silica content being the same as in the liquid phase. For sulfur contents up to 15 wt.%, sulfur would not precipitate, for higher contents an additional FeS layer would form on top of the inner core. In the presence of silicon it has also been suggested that the liquid core would partition into a lower Si-rich part and an upper S-rich part leading to an accretion of solid FeS in the mantle layer. However, previous studies (Hauck et al., 2013; Knibbe and van Westrenen, 2015; Padovan et al., 2014) could not confirm the presence of such a layer and therefore this particular case is not further treated in this study.

An example model is given in Figure 3.1. The pressure for this model is around 5 GPa at the CMB and 30-40 GPa in the center, in agreement with previous studies (Hauck et al., 2013; Dumberry and Rivoldini, 2015).

3.2.2. Rheological Models

In a second step the rheological model is computed. For this step we follow the same approach as Padovan et al. (2014) using a Maxwell model for the core and crust and a pseudo-period Andrade model for the mantle (Jackson and Faul, 2010). The tidal Love numbers are then computed using a matrix propagation method (e.g. Segatz et al. (1988)) taking as input the radial profile of density and complex shear modulus μ, which in the case of a Maxwell model is given by

$$\mu = \frac{i\omega\mu_U}{i\omega + \frac{\mu_U}{\eta}}. \tag{3.11}$$

In Equation (3.11) ω is the tidal frequency $2\pi/t$ with t being the tidal period, i.e. $\approx$ 88 days for Mercury (Van Hoolst and Jacobs, 2003). μ_U is the unrelaxed rigidity of the corresponding layer and η its viscosity. The ratio η/μ_U corresponds to the Maxwell time τ_M of the material. In the case where $\tau_M \gg 2\pi/\omega$ the medium reacts fully elastically to external forces, while in the case $\tau_M \ll 2\pi/\omega$ the material is in the fluid regime. We use the Maxwell rheology for the solid inner core and the crust since both are assumed to respond elastically and the liquid core is in the fluid regime. However, the mantle is expected to show a viscoelastic response to the external tidal potential ($\tau_M \approx 2\pi/\omega$) and it has been shown previously that in this case a Maxwell description is inadequate (Efroimsky and Lainey, 2007; Nimmo et al., 2012; Padovan et al., 2014). Therefore, for the mantle we employ the Andrade pseudo-prediod model introduced by Jackson and Faul (2010). The complex shear modulus is expressed as

$$\mu = \frac{1}{J_R + iJ_I}, \tag{3.12}$$

where J_R and J_I are the real and imaginary parts of the complex compliance given as

$$\begin{aligned} J_R &= \frac{1}{\mu_U}[1 \\ &\quad +\beta^*\Gamma(1+\alpha)\omega_p^{-\alpha}\cos\left(\frac{\alpha\pi}{2}\right)], \quad (3.13) \\ J_I &= \frac{1}{\mu_U}[\beta^*\Gamma(1+\alpha)\omega_p^{-\alpha}\sin\left(\frac{\alpha\pi}{2}\right) \\ &\quad +\frac{1}{\omega_p\tau_M}]. \quad (3.14) \end{aligned}$$

In the equations above, μ_U denotes the unrelaxed rigidity, α and β^* are the Andrade creep coefficient and parameter, respectively, and Γ is the Gamma-function. The tidal frequency is replaced here by the pseudo-frequency $\omega_p = 2\pi/X_b$, where X_b is the pseudo-period master variable (Jackson and Faul, 2010; Padovan et al., 2014). It is temperature- and pressure-dependent and can be computed by

$$\begin{aligned} X_b =& T_0\left(\frac{d}{d_R}\right)^{-m}\exp\left[\left(\frac{-E_B}{R}\right)\left(\frac{1}{T}-\frac{1}{T_R}\right)\right] \\ &\cdot\exp\left[\left(\frac{-V}{R}\right)\left(\frac{P}{T}-\frac{P_R}{T_R}\right)\right]. \end{aligned} \tag{3.15}$$

The exponent m characterizes the dependence on the grain size d. E_B is the activation energy

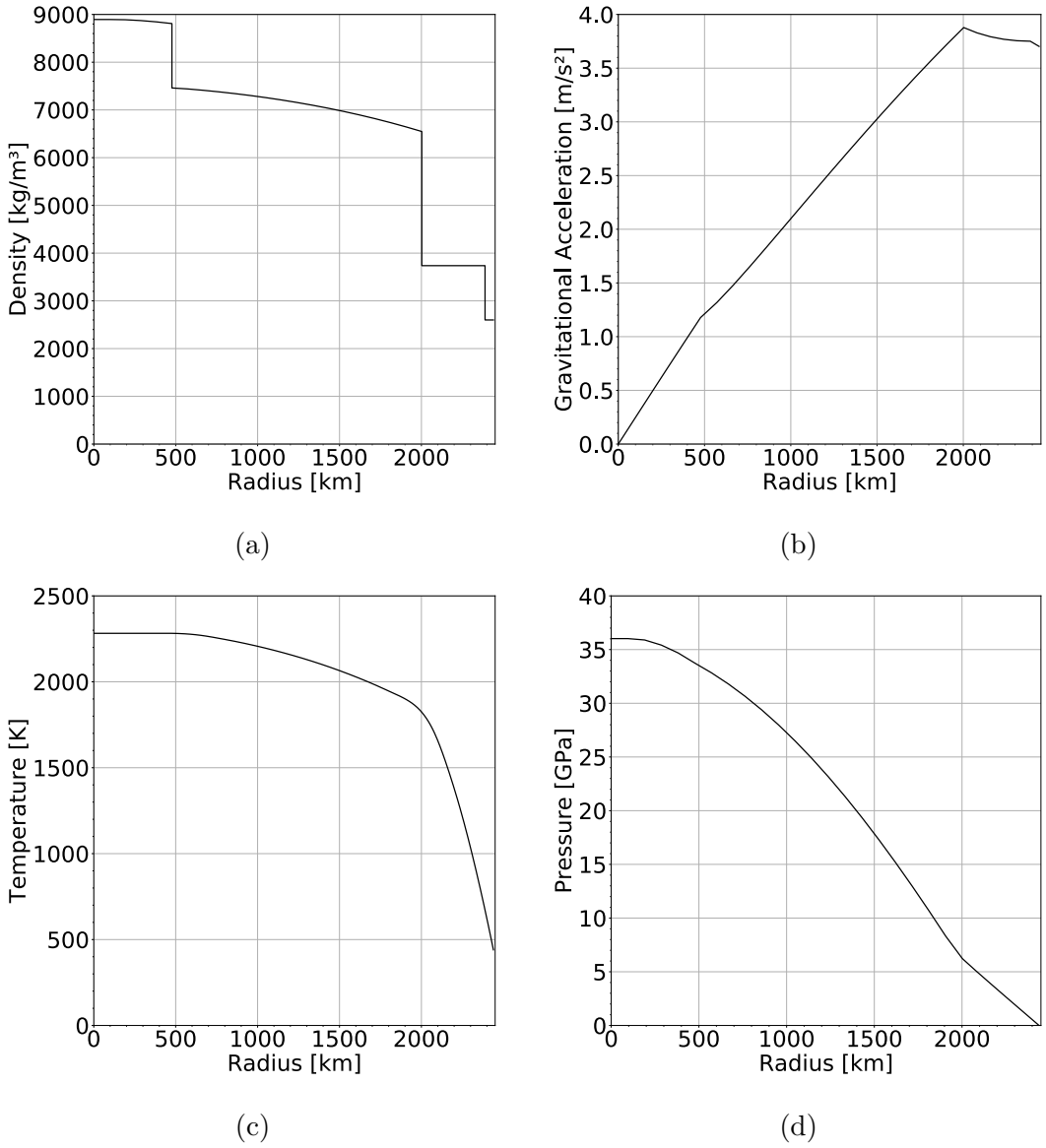

Figure 3.1: Example of a structural model consistent with the geodetic constraints. The core radius is about 2000 km. Figure (a) shows the density profile assumed constant in the mantle and gradually increasing within the core due to increasing pressure. The phase transition from a liquid to solid core occurs at a radius of around 500 km. (b) shows the gravitational acceleration and Figure (c) and (d) the temperature and pressure profiles. The pressure is around 5 GPa at the core-mantle boundary and between 30 and 40 GPa in the center.

and V the activation volume. R is the ideal gas constant and P_R and T_R the reference temperature and pressure. The unrelaxed rigidity can be calculated from the temperature and pressure of the respective layer. We calculate them for a reference temperature of $T_R = 1173$ K and a reference pressure of $P_R = 0.2$ GPa (Jackson and Faul, 2010) as

$$\mu_U(T_R, P_R) = \mu_0 + (T - T_R)\frac{d\mu}{dT} + (P - P_R)\frac{d\mu}{dP}. \quad (3.16)$$

For the composite rigidity μ_0 we assumed values between 59 and 71 GPa representing the possible end members of Mercury's mantle composition

(Padovan et al., 2014). $d\mu/dT$ is set to 13.6×10^{-3} GPa/K and $d\mu/dP$ to 1.8 (Jackson and Faul, 2010). All further parameters used to compute the rheology in this study are summarized in Table 3.2.
The pressure inside each layer is given by the respective structural model and the temperature is controlled by the CMB temperature as well as by the surface temperature, which is set to 440 K (Padovan et al., 2014). The temperature profile is obtained by solving the static heat conduction equation

$$k\frac{1}{r^2}\frac{d}{dr}\left(r^2\frac{dT}{dr}\right)+\rho H=0. \tag{3.17}$$

In our case the assumption of a conductive profile is justified by the chosen temperature range. On the upper bound a higher temperature would result in partial melting of the mantle, and on the lower bound the mantle would be too cold to convect. For the temperatures in between a convective profile might be generally possible leading to modified temperatues. However, these would still fall in the assumed temperature range and therefore not significantly modify our results. The heat production rate H is set for the crust to $H_c = 2.2 \times 10^{-11}$ W·kg^{-1} (Peplowski et al., 2011). For the mantle we used $H_m = H_c/2.5$ (Padovan et al., 2014) in agreement with the enrichment factor derived by (Tosi et al., 2013). The value of the thermal conductivity k is set to 3.3 Wm^{-1}K^{-1}. For a given temperature profile the rigidity and viscosity of each layer can then be derived from the complex compliance by

$$\mu = \sqrt{J_R^2 + J_I^2} \tag{3.18}$$

$$\eta = 1/\sqrt{J_I \omega_p}. \tag{3.19}$$

3.3. Results

The resulting models of Mercury's interior are in agreement with the currently available literature constraints. We find models with liquid cores between 1950 and 2100 km in agreement with Hauck et al. (2013); Rivoldini and Van Hoolst (2013); Margot et al. (2017). Mantle densities are between 2800 and 4000 kg/m^3, a range that covers all cover all possible composition models for Mercury's mantle (e.g. Rivoldini et al. (2009) and Padovan et al. (2014)).

3.3.1. Tidal Love Numbers

The measured k_2 value is on the lower quarter of all possible interior models. Typical k_2 values range between 0.45 and 0.52 implying that the measured value argues for a high mantle rigidity, large grain-sizes and / or a lower temperature at the core-mantle boundary in agreement with Padovan et al. (2014). In the considered range of models the tidal Love number h_2 ranges between 0.77 and 0.93. The corresponding tidal amplitudes are between 1.93 to 2.33 m at the equator and 0.24 to 0.29 m at the poles. For the tidal Love number l_2 we find values between 0.17 and 0.20. The main parameters controlling h_2 are the size of the liquid core and the unrelaxed rigidity of the mantle, while the sensitivity to the mantle density is small. Another control parameter is the temperature at the CMB because it strongly influences the mantle viscosity.

3.3.2. Inner Core Radius

The size of Mercury's inner core is a key parameter to understand the workings of the planetary dynamo. Further, Peale et al. (2016) showed that a solid inner core would raise an additional torque on the silicate shell due to its non-spherical shape. As a consequence the resulting C/MR^2 would change it's value based on the size and density of the solid core. Based on the MESSENGER results, the radius of the inner core is assumed to be smaller than $\approx$ 1300 km (Dumberry and Rivoldini, 2015; Knibbe and van Westrenen, 2015) with smaller core sizes being favored. However, no direct measurements are currently available and it is not evident that an improved measurement accuracy will lead to a direct detection (Margot et al., 2017). Therefore, an uncertainty in Mercury's moment of inertia persists. The measurement of h_2 is listed among the objectives of the BepiColombo Laser Altimeter (BELA) aboard the BepiColombo mission (Thomas et al., 2007). An important advantage of having both tidal Love numbers is that certain trade-offs among the parameters can be suppressed by combining them. The main parameter controlling the magnitude of k_2 and h_2 in case of Mercury is the existence of a liquid core. Further, the amplitude of the tidal deformation is controlled by the mantle rheology. For the given geodetic constraints, and for each Love number individually, the magnitude is mainly controlled by the thickness and rheological properties of the mantle while the presence of an inner core has only a minor influence (Figure 3.2a). However, a linear combination as well as the ratio h_2/k_2 can-

Parameter	Symbol	Value	Unit	Reference
Crust rigidity	μ_U	55	GPa	Padovan et al. (2014)
Crust viscosity	η	10^{23}	Pa s	Padovan et al. (2014)
Liquid core rigidity	μ_U	0	GPa	-
Liquid core viscosity	η	0	GPa	-
Solid core rigidity	μ_U	100	GPa	Padovan et al. (2014)
Solid core viscosity	η	10^{20}	Pa s	Padovan et al. (2014)
Andrade creep coefficient	α	0.33	-	Jackson and Faul (2010)
Andrade creep parameter	β	0.02	-	Jackson and Faul (2010)
Reference temperature	T_R	1173	K	Jackson and Faul (2010)
Reference pressure	P_R	0.2	GPa	Jackson and Faul (2010)
Reference grain size	d_R	3.1	μm	Jackson and Faul (2010)
Grain size exponent	m	1.31	-	Jackson and Faul (2010)
Activation volume	V	10^{-5}	m^3 $mol^{-}1$	Jackson and Faul (2010)
Activation energy	E_B	303	MJ $mol^{-}1$	Jackson and Faul (2010)

Table 3.2: Rheologic parameters used in the computation of the tidal Love numbers.

cels out the ambiguity to a certain extent. In presence of a density contrast between a solid core and a liquid core, the size of an inner core is noticeable when combining both Love numbers. It should be noted that the density contrast alone is not sufficient to observe the effect, the inner core must be in a predominantly elastic regime, i.e. $\tau_M > 2\pi/\omega$. The effect is further not limited to the given range of k_2 but also noticeable when assuming much higher values. The linear combination $1+k_2-h_2$ is known as the *diminishing factor*, which has been proposed previously to better constrain the ice thickness of Jupiter's moon Europa (Wahr et al., 2006) and of other icy satellites as Ganymede (Steinbrügge et al., 2015). For small solid cores however, the effect is barely noticeable, and a measurement of the respective ratio or linear combination would allow the determination of an upper bound for the size of the inner core but the determination of the actual radius would have a significant uncertainty due to the remaining ambiguity. The ratio h_2/k_2 is affected by a similar behavior, however is less ambiguous for larger cores. Therefore, for inner cores > 700 km in radius and with a 1%-level accuracy in the determination of h_2, the inner core size can potentially be inferred to roughly ± 100 km.

3.3.3. Phase-lags

Since the tidal Love numbers are complex numbers they are not only characterized by their amplitude but also have a phase which is a function of the rheological parameters. The tidal phase-lag is defined as

$$\arctan(\varphi_{k2}) = \frac{\mathrm{Im}(k_2)}{\mathrm{Re}(k_2)}. \tag{3.20}$$

$\mathrm{Re}(k_2)$ and $\mathrm{Im}(k_2)$ are the real and imaginary part of the complex number k_2, respectively. In the elastic and fluid limit of the rheology, the Maxwell-time is either significantly larger or lower than the forcing period, in which case the body reacts instantly to the tidal forcing. Such a case implies further that no heat is dissipated. The more the forcing period approaches the Maxwell-time, the more the body reacts visco-elastically and the more heat is dissipated. The tidal dissipation can be derived from a multipole expansion in eccentricity and inclination. To zero-th order inclination and fourth order in eccentricity the mean tidal dissipation rate can then be derived from Makarov and Efroimsky (2014) as

$$\dot{E} = \frac{GM_{\mathrm{Sun}}^2 R^5 n}{a^6}\mathrm{Im}(k_2)\left(\frac{3}{4} - \frac{39}{16}e^2 + \frac{2043}{32}e^4\right). \tag{3.21}$$

A particularity of the 3:2 resonance is that the tidal dissipation barely depends on the eccentricity. Therefore, a body with a low $Im(k)$ but a significant eccentricity like Mercury does not dissipate much tidal energy. The main source of tidal dissipation on Mercury is the mantle, however the maximum values for $\mathrm{Im}(k_2)$ consistent with the geodetic constraints range between 0.02 and 0.03 corresponding to a phase-lag of less than 4° (Figure 3.3). This result is consistent with the maximum value derived by Baland et al. (2017) estimated from the spin orientation. The maximum tidal dissipation expected from Equation (3.21) is then equivalent to a surface heat flux < 0.16 mW/m^2. Since the viscosity is mainly controlled by the temperature and grain size, a measurement of a tidal phase-lag with an accuracy better than 0.5° would however help to further constrain the temperature at the core-mantle

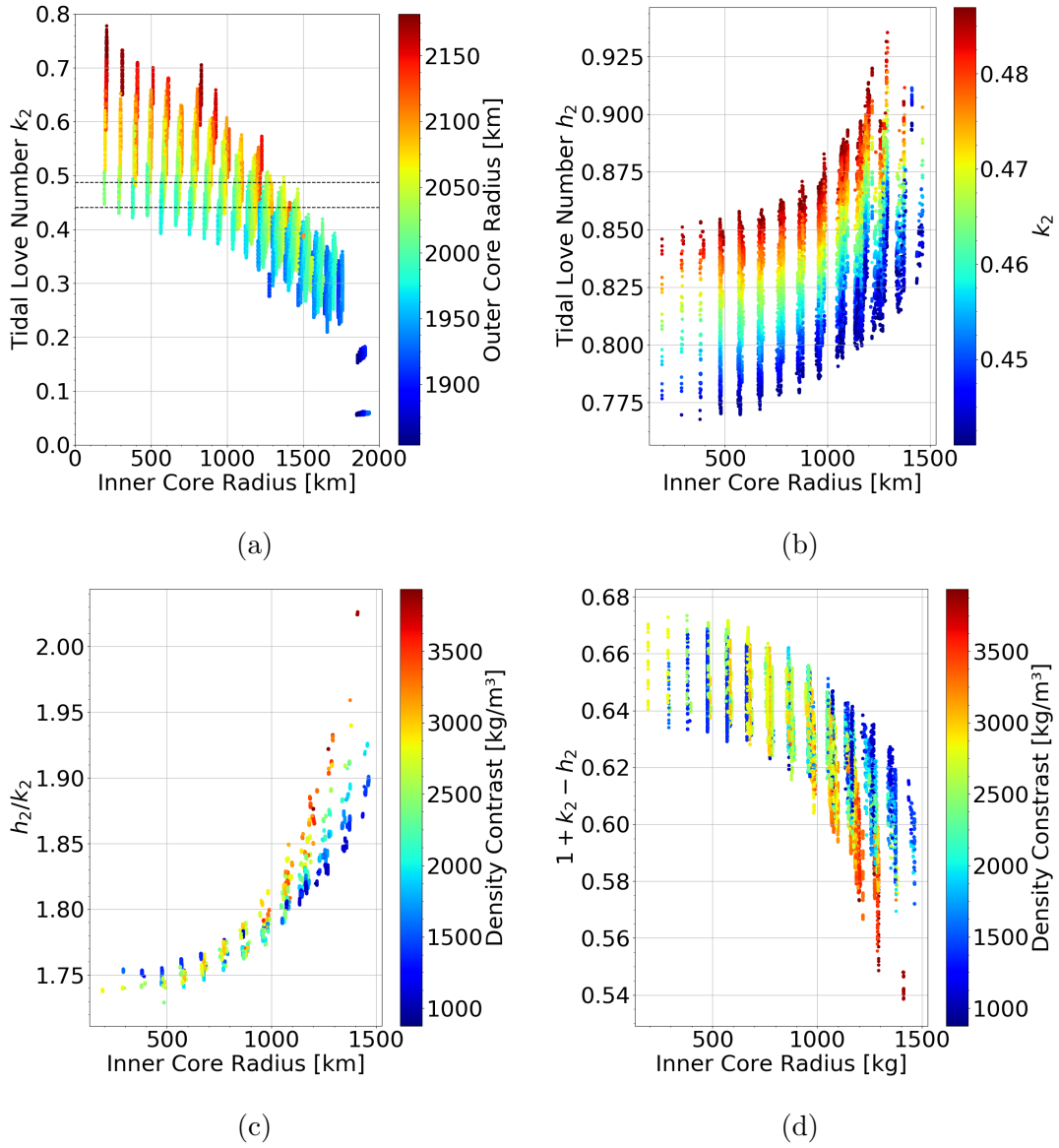

Figure 3.2: (a) Full range of tidal Love number k_2 as a function of inner core size. No direct dependence can be inferred within the measured k_2 range (dashed lines). (b) The tidal Love number h_2 for the subset of models in agreement with the k_2 error interval from Figure (a). The result is ambiguous, the observable trend is given by the strong correlation with k_2. (c) Using the ratio h_2/k_2 is less ambiguous and therefore allows setting an upper limit on the core size. (d) The same effect can be principally observed using the linear combination $1 + k_2 - h_2$, however provides a less strict constraint.

boundary and therefore also further constrain the physical state of the core. The caveat at this point is that even small amounts of iron have an influence on the mantle viscosity and can lead to lower values (Zhao et al., 2009). A low grain size can have a similar effect (Figure 3.3). This might also lead to a lower Maxwell time and therefore to a bigger phase-lag.

The h_2 and k_2 phase-lags of Mercury are expected to be almost identical. This is in contrast to the case of icy satellites, where the phase-lag difference can be indicative for dissipation in the deep interior (Hussmann et al., 2016). The maximum difference is expected to be 0.2° but due to the small radial amplitudes the phase-lag of k_2 is more likely to be measured than the h_2-lag (see section 3.4).

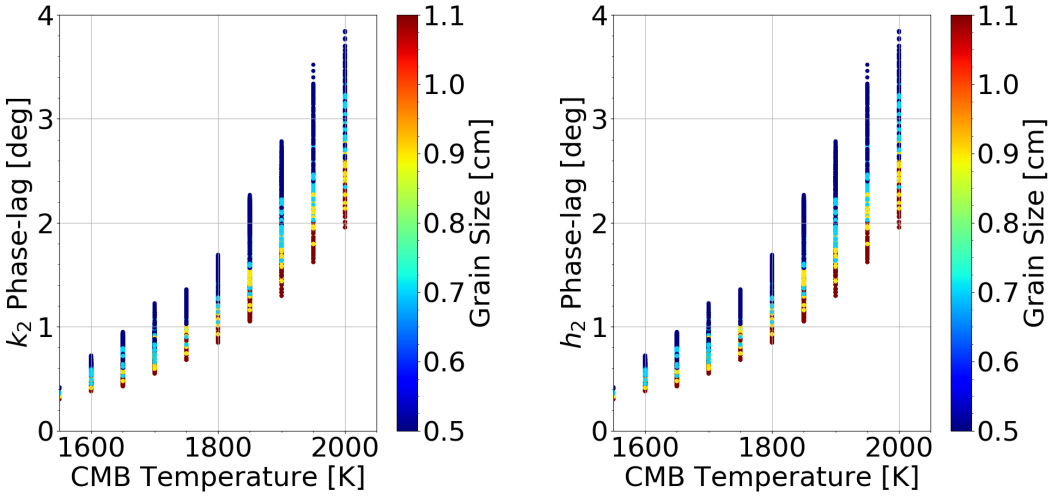

(a) (b)

Figure 3.3: Phase-lag of (a) k_2 and (b) h_2 as a function of the temperature at the core-mantle boundary. The difference between both phase-lags is < 0.2 at maximum and therefore barely noticeable.

3.4. Discussion and Conclusion

We constructed a broad range of Mercury interior models compliant with MESSENGER measurements of mean density, moment of inertia and C_m/C within their 3-σ range. Our approach to sample the parameter space in a regular grid is chosen to assure that all possible models in agreement with the measurement constraints are represented in our analysis. If our current understanding of the interior structure of Mercury is correct, then a measurement of the tidal Love number h_2 should fall within the range of 0.77 to 0.93. The corresponding tidal deformations from peak-to-peak are between 1.93 and 2.33 m at the equator and between 0.24 and 0.29 m at the poles. Refined measurements of the moment of inertia, C_m/C and k_2 are expected to further constrain the range. The remaining uncertainties should mainly be captured inside the parameters used for the interior modeling. While for the most part these values rely on laboratory measurements, an uncertainty linked to the composition of the core remains and a measured h_2 number outside the predicted range could point out inaccurate assumptions of present-day interior models. In the case of a compliant measurement the remaining range of possible values is particularly valuable to obtain additional constraints on the inner core size. The current literature assumption is that the inner core is small, i.e. $<$ 1000 km in radius (Margot et al., 2017). This assumption could be confirmed or rejected with the proposed h_2/k_2 measurement. In case of a small core however, the inner core size is unlikely to be constrained any further due to the remaining ambiguity in the interior models and the little sensitivity of h_2/k_2 to a small inner core (Figure 3.2c). In case of an inner core with a radius above 1000 km, its size could be constrained due to the rapid growth of the h_2 over k_2 ratio. Therefore, it would also allow for reassessing the moment of inertia and providing constraints for models addressing Mercury's core dynamics and related magnetic field generation. However, it requires that the tidal Love number h_2 can be measured with the sufficient accuracy since the measurement of k_2 alone is not informative, unlike previous authors suggested (Spohn et al., 2001). Assuming that the h_2 determination dominates the h_2/k_2 error at the upcoming BepiColombo mission, an absolute accuracy of < 0.05 in h_2 would be needed to discriminate between a large and a small core. For an h_2 value of 0.8 this corresponds to a measurement error of 6%. This is close to the estimated 7% by Koch et al. (2010) for the BepiColombo Laser Altimeter (BELA) (Thomas et al., 2007). The authors suggest inferring h_2 from the time dependency of the spherical harmonics expansion of Mercury's topography. However, their estimation assumes a mission life time of four years and does not treat a wide range of systematic errors (e.g. instrument alignment or rotational state). Indeed, due to the

low tidal amplitudes and the 10 Hz shot frequency of BELA an accurate-enough determination will be very challenging. Alternative methods, like cross-over measurements suffer from the low-rotation rate of Mercury and a consequently low amount of cross-over points at lower latitudes during the nominal mission. While being in the range of what is technically feasible, the success of the measurement will depend on the final instrument performance in orbit, the mission lifetime, the accuracy of the alignment calibration as well as on the quality of the orbit reconstruction.
The tidal phase-lag is inferred to be lower than 4°. The tidal dissipation would then correspond to a surface heat flux of < 0.16 mW/m^2. A measurement of the tidal phase-lag can allow for constraining the temperature at the core-mantle boundary under the condition that the profile is conductive, which seems to be the case based on thermal evolution models (Tosi et al., 2013; Padovan et al., 2017), and thereby further constrain the physical state of Mercury's core. The accuracy on the real and imaginary part of k_2 has been estimated for the Mercury Orbiter Radio Experiment (MORE) (Iess et al., 2009) on board of the upcoming BepiColombo mission to be 2.6×10^{-4} (Imperi et al., 2018). This allows for a phase-lag measurement with an accurcay of $< 0.1°$ and therefore provides the needed precision. An estimate for the h_2 phase-lag is currently not available, however due to the small expected radial amplitudes unlikely to be measured. We expect it to be very similar to the k_2-lag and below 4°. Therefore, refined measurements of Mercury's gravity field and librations together with a simultaneous determination of h_2 as well as both, the real and imaginary part of k_2 by the upcoming mission can constrain the interior structure of Mercury, including the inner core size and the temperature profile, to an unprecedented level.

Acknowledgments

The authors would like to thank Frank Sohl for helpful discussions. A. Stark was supported by a research grant from the Helmholtz Association and German Aerospace Center (DLR). All data for this paper are properly cited and referred to in the reference list. The numerical output necessary to generate the figures is given in the supplementary data.

References

Anderson, B.J., Johnson, C.L., Korth, H., Winslow, R.M., Borovsky, J.E., Purucker, M.E., Slavin, J.A., Solomon, S.C., Zuber, M.T., McNutt, R.L.. Low-degree structure in Mercury's planetary magnetic field. Journal of Geophysical Research: Planets 2012;117(E12). doi:10.1029/2012JE004159; e00L12.

Baland, R.M., Yseboodt, M., Rivoldini, A., Hoolst, T.V.. Obliquity of Mercury: Influence of the precession of the pericenter and of tides. Icarus 2017;291(Supplement C):136 – 159. doi:10.1016/j.icarus.2017.03.020.

Benkhoff, J., van Casteren, J., Hayakawa, H., Fujimoto, M., Laakso, H., Novara, M., Ferri, P., Middleton, H.R., Ziethe, R.. Bepicolombo-comprehensive exploration of mercury: Mission overview and science goals. Planetary and Space Science 2010;58(1–2):2 – 20. doi:10.1016/j.pss.2009.09.020.

Beutl, M., Pottlacher, G., Jäger, H.. Thermophysical properties of liquid iron. International Journal of Thermophysics 1994;15(6):1323–1331. doi:10.1007/BF01458840.

Cao, H., Aurnou, J.M., Wicht, J., Dietrich, W., Soderlund, K.M., Russell, C.T.. A dynamo explanation for Mercury's anomalous magnetic field. Geophysical Review Letters 2014;41:4127–4134. doi:10.1002/2014GL060196.

Dumberry, M., Rivoldini, A.. Mercury's inner core size and core-crystallization regime. Icarus 2015;248:254 – 268. doi:10.1016/j.icarus.2014.10.038.

Efroimsky, M., Lainey, V.. Physics of bodily tides in terrestrial planets and the appropriate scales of dynamical evolution. Journal of Geophysical Research: Planets 2007;112(E12). doi:10.1029/2007JE002908.

Fei, Y., Li, J., Bertka, C., Prewitt, C.. Structure type and bulk modulus of Fe3S, a new iron-sulfur compound. American Mineralogist 2000;85:1830–1833. doi:10.2138/am-2000-11-1229.

Hauck, S.A., Margot, J.L., Solomon, S.C., Phillips, R.J., Johnson, C.L., Lemoine, F.G., Mazarico, E., McCoy, T.J., Padovan, S., Peale, S.J., Perry, M.E., Smith, D.E., Zuber, M.T.. The curious case of Mercury's internal structure. Journal of Geophysical Research: Plan-

ets 2013;118(6):1204–1220. doi:10.1002/jgre.20091.

Hauck, S.A., Solomon, S.C., Smith, D.A.. Predicted recovery of Mercury's internal structure by MESSENGER. Geophysical Research Letters 2007;34(18). doi:10.1029/2007GL030793; l18201.

Hussmann, H., Shoji, D., Steinbrügge, G., Stark, A., Sohl, F.. Constraints on dissipation in the deep interiors of Ganymede and Europa from tidal phase-lags. Celestial Mechanics and Dynamical Astronomy 2016;126(1):131–144. doi:10.1007/s10569-016-9721-0.

Iess, L., Asmar, S., Tortora, P.. MORE: An advanced tracking experiment for the exploration of Mercury with the mission BepiColombo. Acta Astronautica 2009;65(5):666 – 675. doi:10.1016/j.actaastro.2009.01.049.

Imperi, L., Iess, L., Mariani, M.J.. An analysis of the geodesy and relativity experiments of bepicolombo. Icarus 2018;301:9 – 25. doi:10.1016/j.icarus.2017.09.008.

Jackson, I., Faul, U.H.. Grainsize-sensitive viscoelastic relaxation in olivine: Towards a robust laboratory-based model for seismological application. Physics of the Earth and Planetary Interiors 2010;183(1):151 – 163. doi:10.1016/j.pepi.2010.09.005; special Issue on Deep Slab and Mantle Dynamics.

Jing, Z., Wang, Y., Kono, Y., Yu, T., Sakamaki, T., Park, C., Rivers, M.L., Sutton, S.R., Shen, G.. Sound velocity of Fe-S liquids at high pressure: Implications for the Moon's molten outer core. Earth and Planetary Science Letters 2014;396:78 – 87. doi:10.1016/j.epsl.2014.04.015.

Knibbe, J.S., van Westrenen, W.. The interior configuration of planet Mercury constrained by moment of inertia and planetary contraction. Journal of Geophysical Research: Planets 2015;120(11):1904–1923. doi:10.1002/2015JE004908; 2015JE004908.

Koch, C., Kallenbach, R., Christensen, U.. Mercury's global topography and tidal signal from laser altimetry by using a rectangular grid. Planetary and Space Science 2010;58(14):2022 – 2030. doi:10.1016/j.pss.2010.10.002.

Komabayashi, T., Fei, Y.. Internally consistent thermodynamic database for iron to the Earth's core conditions. Journal of Geophysical Research: Solid Earth 2010;115(B3). doi:10.1029/2009JB006442.

Kuwayama, Y., Hirose, K.. Phase relations in the system Fe-FeSi at 21 GPa. American Mineralogist 2004;89(2-3):273–276. doi:10.2138/am-2004-2-303.

Levenberg, K.. A method for the solution of certain problems in least squares. Quart J App Math 1944;2(2):164–168. doi:10.1137/0111030.

Lin, J.F., Campbell, A.J., Heinz, D.L., Shen, G.. Static compression of iron-silicon alloys: Implications for silicon in the Earth's core. Journal of Geophysical Research: Solid Earth 2003;108(B1). doi:10.1029/2002JB001978.

Makarov, V., Efroimsky, M.. Tidal Dissipation in a Homogeneous Spherical Body. II. Three Examples: Mercury, IO, and Kepler-10 b. The Astrophysical Journal 2014;795:7. doi:10.1088/0004-637X/795/1/7.

Malavergne, V., Toplis, M.J., Berthet, S., Jones, J.. Highly reducing conditions during core formation on Mercury: Implications for internal structure and the origin of a magnetic field. Icarus 2010;206:199–209. doi:10.1016/j.icarus.2009.09.001.

Manglik, A., Wicht, J., Christensen, U.R.. A dynamo model with double diffusive convection for Mercury's core. Earth and Planetary Science Letters 2010;289(3):619 – 628. doi:10.1016/j.epsl.2009.12.007.

Margot, J., Peale, S., Jurgens, R., Slade, M., Holin, I.. Large Longitude Libration of Mercury Reveals a Molten Core. Science 2007;316:710. doi:10.1126/science.1140514.

Margot, J.L., Hauk II, S.A., Mazarico, E., Padovan, S., Pealo, S.J.. Mercury's Internal Structure. In: Solomon, S., Anderson, B., Nittler, L., editors. Mercury - The View after MESSENGER. Cambridge University Press; 2017. .

Margot, J.L., Peale, S.J., Solomon, S.C., Hauck, S.A., Ghigo, F.D., Jurgens, R.F., Yseboodt, M., Giorgini, J.D., Padovan, S., Campbell, D.B.. Mercury's moment of inertia from spin and gravity data. Journal of Geophysical Research: Planets 2012;117(E12). doi:10.1029/2012JE004161.

Marquardt, D.W.. An algorithm for least-squares

estimation of nonlinear parameters. Journal of the Society for Industrial and Applied Mathematics 1963;11(2):431–441. doi:10.1137/0111030.

Mazarico, E., Barker, M., Neumann, G., Zuber, M., Smith, D.. Detection of the lunar body tide by the Lunar Orbiter Laser Altimeter. Geophysical Research Letters 2014a;41. doi:10.1002/2013GL059085.

Mazarico, E., Genova, A., Goossens, S., Lemoine, F.G., Neumann, G.A., Zuber, M.T., Smith, D.E., Solomon, S.C.. The gravity field, orientation, and ephemeris of Mercury from MESSENGER observations after three years in orbit. Journal of Geophysical Research: Planets 2014b;119(12):2417–2436. doi:10.1002/2014JE004675.

Nimmo, F., Faul, U.H., Garnero, E.J.. Dissipation at tidal and seismic frequencies in a melt-free moon. Journal of Geophysical Research: Planets 2012;117(E9). doi:10.1029/2012JE004160.

Padovan, S., Margot, J.L., Hauck, S.A., Moore, W.B., Solomon, S.C.. The tides of Mercury and possible implications for its interior structure. Journal of Geophysical Research: Planets 2014;119(4):850–866. doi:10.1002/2013JE004459.

Padovan, S., Tosi, N., Plesa, A.C., Ruedas, T.. Volcanic Infillings of Large Basins on Mercury as Indicators of Mantle Thermal State and Composition. In: Lunar and Planetary Science Conference. volume 48 of *Lunar and Planetary Science Conference*; 2017. p. 1809.

Peale, S.. Does Mercury have a molten core. Nature 1976;262:765. doi:10.1038/262765a0.

Peale, S.J., Margot, J.L., Hauck, S.A., Solomon, S.C.. Consequences of a solid inner core on Mercury's spin configuration. Icarus 2016;264:443–455. doi:10.1016/j.icarus.2015.09.024.

Peale, S.J., Phillips, R.J., Solomon, S.C., Smith, D.E., Zuber, M.T.. A procedure for determining the nature of Mercury's core. Meteoritics & Planetary Science 2002;37(9):1269–1283. doi:10.1111/j.1945-5100.2002.tb00895.x.

Peplowski, P.N., Evans, L.G., Hauck, S.A., McCoy, T.J., Boynton, W.V., Gillis-Davis, J.J., Ebel, D.S., Goldsten, J.O., Hamara, D.K., Lawrence, D.J., McNutt, R.L., Nittler, L.R., Solomon, S.C., Rhodes, E.A., Sprague, A.L., Starr, R.D., Stockstill-Cahill, K.R.. Radioactive Elements on Mercury's Surface from MESSENGER: Implications for the Planet's Formation and Evolution. Science 2011;333(6051):1850–1852. doi:10.1126/science.1211576.

Perry, M.E., Neumann, G.A., Phillips, R.J., Barnouin, O.S., Ernst, C.M., Kahan, D.S., Solomon, S.C., Zuber, M.T., Smith, D.E., Hauck, S.A., Peale, S.J., Margot, J.L., Mazarico, E., Johnson, C.L., Gaskell, R.W., Roberts, J.H., McNutt, R.L., Oberst, J.. The low-degree shape of Mercury. Geophysical Research Letters 2015;42(17):6951–6958. doi:10.1002/2015GL065101; 2015GL065101.

Rivoldini, A., Van Hoolst, T.. The interior structure of Mercury constrained by the low-degree gravity field and the rotation of Mercury. Earth and Planetary Science Letters 2013;377:62–72. doi:10.1016/j.epsl.2013.07.021.

Rivoldini, A., Van Hoolst, T., Verhoeven, O.. The interior structure of Mercury and its core sulfur content. Icarus 2009;201:12–30. doi:10.1016/j.icarus.2008.12.020.

Sanloup, C., Fiquet, G., Gregoryanz, E., Morard, G., Mezouar, M.. Effect of Si on liquid Fe compressibility: Implications for sound velocity in core materials. Geophysical Research Letters 2004;31(7):L07604. doi:10.1029/2004GL019526.

Sanloup, C., Guyot, F., Gillet, P., Fiquet, G., Mezouar, M., Martinez, I.. Density measurements of liquid Fe-S alloys at high-pressure. Geophysical Research Letters 2000;27(6):811–814. doi:10.1029/1999GL008431.

Segatz, M., Spohn, T., Ross, M., Schubert, G.. Tidal dissipation, surface heat flow, and figure of viscoelastic models of Io. Icarus 1988;75:187–206. doi:10.1016/0019-1035(88)90001-2.

Smith, D.E., Zuber, M.T., Phillips, R.J., Solomon, S.C., Hauck, S.A., Lemoine, F.G., Mazarico, E., Neumann, G.A., Peale, S.J., Margot, J.L., Johnson, C.L., Torrence, M.H., Perry, M.E., Rowlands, D.D., Goossens, S., Head, J.W., Taylor, A.H.. Gravity Field and Internal Structure of Mercury from MESSENGER. Science 2012;336:214. doi:10.1126/science.1218809.

Solomon, S.C., Jr., R.L.M., Prockter, L.M.. Mercury after the {MESSENGER} flybys: An introduction to the special issue of planetary and space science. Planetary and Space Science

2011;59(15):1827 – 1828. doi:10.1016/j.pss.2011.08.004.

Stark, A., Oberst, J., Preusker, F., Peale, S.J., Margot, J.L., Phillips, R.J., Neumann, G.A., Smith, D.E., Zuber, M.T., Solomon, S.C.. First MESSENGER orbital observations of Mercury's librations. Geophysical Research Letters 2015;42(19):7881–7889. doi:10.1002/2015GL065152.

Steinbrügge, G., Stark, A., Hussmann, H., Sohl, F., Oberst, J.. Measuring tidal deformations by laser altimetry. A performance model for the Ganymede Laser Altimeter. Planetary and Space Science 2015;117:184 – 191. doi:10.1016/j.pss.2015.06.013.

Thomas, N., Spohn, T., Barriot, J.P., Benz, W., Beutler, G., Christensen, U., Dehant, V., Fallnich, C., Giardini, D., Groussin, O., Gunderson, K., Hauber, E., Hilchenbach, M., Iess, L., Lamy, P., Lara, L.M., Logonne, P., Lopez-Moreno, J., Michaelis, H., Oberst, J., Resendes, D., Reynaud, J.L., Rodrigro, R., Sasaki, S., Seiferlin, K., Wieczorek, M., Whitby, J.. The BepiColombo Laser Altimeter (BELA): Concept and baseline design. Planetary and Space Science 2007;55:1398–1413. doi:10.1016/j.pss.2007.03.003.

Tosi, N., Grott, M., Plesa, A.C., Breuer, D.. Thermochemical evolution of mercury's interior. Journal of Geophysical Research: Planets 2013;118(12):2474–2487. doi:10.1002/jgre.20168.

Uchida, T., Wang, Y., Rivers, M.L., Sutton, S.R.. Stability field and thermal equation of state of epsilon-iron determined by synchrotron X-ray diffraction in a multianvil apparatus. Journal of Geophysical Research: Solid Earth 2001;106(B10):21799–21810. doi:10.1029/2001JB000258.

Van Hoolst, T., Jacobs, C.. Mercury's tides and interior structure. Journal of Geophysical Research (Planets) 2003;108:5121. doi:10.1029/2003JE002126.

Verma, A.K., Margot, J.L.. Mercury's gravity, tides, and spin from MESSENGER radio science data. Journal of Geophysical Research: Planets 2016;121(9):1627–1640. doi:10.1002/2016JE005037.

Wahr, J., Zuber, M., Smith, D., Luine, J.. Tides on Europa, and the thickness of Europa's icy shell. Journal of Geophysical Research 2006;111:E12005. doi:10.1029/2006JE002729.

Zhao, Y.H., Zimmerman, M.E., Kohlstedt, D.L.. Effect of iron content on the creep behavior of olivine: 1. Anhydrous conditions. Earth and Planetary Science Letters 2009;287(1):229 – 240. doi:10.1016/j.epsl.2009.08.006.

Chapter 4

Research Paper III

Measuring Tidal Deformations by Laser Altimetry. A Performance Model for the Ganymede Laser Altimeter

G. Steinbrügge[1], A. Stark[1], H. Hussmann[1], F. Sohl[1], J. Oberst[1,2]

[1]German Aerospace Center, Institute of Planetary Research, D-12489 Berlin, Germany
[2]Moscow State University for Geodesy and Cartography, RU-105064 Moscow, Russia

Published in Planetary and Space Science, Volume 117, Pages 184–191
doi: 10.1016/j.pss.2015.06.013
Postprint

Abstract

Invaluable information about the interior of icy satellites orbiting close to the giant planets can be gained by monitoring the response of the satellite's surfaces to external tidal forces. Due to its geodetic accuracy, laser altimetry is the method of choice to measure time-dependent radial surface displacements from orbit. We present an instrument performance model with special focus on the capabilities to determine the corresponding tidal Love number h_2 and apply the model to the Ganymede Laser Altimeter (GALA) on board of the Jupiter Icy Moons Explorer (JUICE). Based on the instrument and spacecraft performance, we derive the range error and the measurement capabilities of the GALA instrument to determine the amplitude of the tide induced radial displacement of Ganymede's surface using the cross-over technique. We find that h_2 of Ganymede can be determined with an accuracy of better than 2 % by using data acquired during the nominal mission. Furthermore, we show that this accuracy is sufficient to confirm the presence of a putative subsurface water ocean and, additionally, to constrain the thickness of the overlaying ice shell to ± 20 km.

4.1. Introduction

The interior structure of Ganymede as we understand it today, mainly from the results of the Galileo mission (Anderson et al., 1998), can be subdivided into five structural layers: An iron core, composed of Fe-FeS sustaining the intrinsic magnetic field by dynamo action (Schubert et al., 1996), is surrounded by a silicate rock mantle and overlain by an ice shell, which can be further divided into an inner high-pressure ice layer (ice III / ice V / ice VI) and an outer ice I layer (Sohl et al., 2002; Vance et al., 2014). Measurements of induced magnetic fields (Kivelson et al., 2002) and recent Hubble Space Telescope observations (Saur et al., 2015) suggest that between the two ice zones a globe-encircling, briny subsurface water ocean may be located. Also, alternating layers between high pressure ices and salty liquid water were conceived by Vance et al. (2014).

However, interior structure models consistent with Ganymede's mean moment of inertia and total mass can constrain neither the ice thickness nor the ocean depth. In order to reduce the ambiguity of the structural models, it has been proposed to measure the dynamic response of Ganymede's ice shell to tidal forces exerted by Jupiter and characterized by the body tide Love numbers h_2 and k_2 (Moore and Schubert, 2003). Similar strategies have been investigated in application to Europa (Moore and Schubert, 2000; Wu et al., 2001; Wahr et al., 2006; Hussmann et al., 2011). While k_2 describes the tidal secondary potential induced by the mass redistribution as a consequence of the external forcing, the Love number h_2 expresses the corresponding radial amplitude u_r of the tidal deformation. It depends on the tidal forcing frequency, the internal structure, and the rheology but in particular on the presence of intervening fluid layers below the surface and the thickness and rigidity of an overlaying ice shell.
In section 4.2, a numerical model designed to estimate the range measurement error and a covariance analysis aiming at the accuracy of the h_2 measurement will be presented. This model will then be applied to the Ganymede Laser Altimeter (GALA) in section 4.3. Toward the end of this section, the derived error will be used further to assess the level of accuracy at which the ice-I thickness can be determined. The obtained results and the limitations of the presented model will then be discussed in section 4.4, and finally some conclusions are drawn in section 4.5.

4.2. Method and Model Description

4.2.1. Ganymede Tides

The radial surface displacement u_r can be measured by laser altimetry as time-dependent variation of the degree-2 shape

$$u_r = \frac{h_2 \Phi(r,\theta,\phi,t)}{g}, \tag{4.1}$$

where $\Phi(r,\theta,\phi,t)$ is the time-dependent tidal potential as a function of the spherical coordinates. Here r denotes the radial distance, θ and ϕ are respectively the co-latitude and longitude of a point on Ganymede's surface, and g is the gravitational acceleration $g = GM_p/R^2$, with M_p and R being Ganymede's total mass and radius. The tidal potential $\Phi(r,\theta,\phi,t)$ on a satellite in synchronous rotation with Jupiter has been described by e.g., Segatz et al. (1988), Moore and Schubert (2000) and Hussmann et al. (2011) and can be expressed up to second degree as

$$\Phi(r,\theta,\phi,t) = r^2\omega^2 e[-\frac{3}{2}P_2^0(\cos\theta)\cos M + \frac{1}{4}P_2^2(\cos\theta)(3\cos M\cos 2\phi + 4\sin M\sin 2\phi)], \tag{4.2}$$

where e and ω are respectively the eccentricity and main tidal frequency and M denotes the mean anomaly of Ganymede with respect to Jupiter. $P_2^0(\cos\theta)$ and $P_2^2(\cos\theta)$ are the associated Legendre polynomials

$$P_2^0(\cos\theta) = \frac{3\cos^2(\theta)-1}{2} \tag{4.3}$$

$$P_2^2(\cos\theta) = 3(1-\cos^2\theta). \tag{4.4}$$

The potential has a maximum amplitude Φ_{Max} at the surface of $3.2 \times r^2\omega^2 e$. The double amplitude (peak-to-peak) of the tidal deformation, assuming a typical h_2 value of 1.3, is shown in Fig. 4.1 (left) and can reach up to 7 m in the case that a subsurface ocean is present.
Thus, since the tidal potential of the body is precisely known, measurements of the radial displacement u_r leads to the determination of h_2, which in turn directly depends on the interior structure, especially the thickness of the outer ice shell and the corresponding rheological parameters. The tidal potential can be extended by an additional term yielding the obliquity of the body (e.g. Kaula

Parameter	Symbol	Unit	Value
Radius	R	km	2631.2 ± 1.7
Mean density	$\overline{\rho}$	kg m^{-3}	1942.0 ± 4.8
Moment-of-inertia factor	MoI	kg m^2	0.3115 ± 0.0028
Gravitational parameter	GM_p	km^3 s^{-2}	9887.83 ± 0.003
Eccentricity	e	-	0.0015
Main tidal period	$2\pi/\omega$	d	7.155

Table 4.1: Ganymede equilibrium and gravity parameters. All values are taken from Schubert et al. (2004).

(1964); Wahr et al. (2009)). This work neglects this term since we assume the obliquity to be known after the spacecraft arrives in Ganymede's orbit and, therefore, should not have significant impact on the h_2 measurement from a technical point of view.

4.2.2. Instrument and Mission Setup

The measurement of Ganymede's tide-induced radial surface displacement amplitudes will be one of the main scientific goals of the Ganymede Laser Altimeter (GALA), which is one of the instruments selected for the Jupiter Icy Moons Explorer (JUICE) of the European Space Agency (ESA) (Grasset et al., 2013). The launch of the spacecraft is scheduled for 2022 and, after a cruise time of eight years, it will start its Jovian tour with several flybys at Europa and Callisto before entering into Ganymede orbit. GALA is built on the heritage of the BepiColombo laser altimeter BELA (Thomas et al., 2007) under the responsibility of the German Aerospace Center (DLR). The technical key parameters of GALA in comparison to the BELA instrument are summarized in Table 4.2. The determination of the tidal Love number h_2 requires altitude measurements temporally distributed over the tidal cycle of the body under investigation. The JUICE spacecraft will be first inserted into an elliptical 200 × 10,000 km orbit. However, the main operational phase for the GALA instrument will be after a period of five month when the JUICE spacecraft is transferred in a polar circular orbit with 500 km altitude. The nominal operational time in this orbit is 132 days. During this time the laser altimeter ground tracks will intersect at certain locations known as cross-over points, which can be derived from the spacecraft trajectory containing the current mission profile by using a dedicated search algorithm (the SPICE kernel used in this study is referenced as `JUP_A5D_140A_LAU_FIN_BET_500`). Since the number of cross-over points increases quadratically with the number of orbits, this leads to a total of 1,068,126 cross-over points, mostly concentrated in the polar regions. The change in tidal distortion can then be inferred from a differential height measurement using two passes above one cross-over point. Fig. 4.1 (right) shows the maximal measurable amplitudes in a grid with a resolution of $1^\circ \times 1^\circ$ in comparison to the expected tidal pattern. It has been considered that JUICE will not conduct science operations continuously due to eight hours per day reserved for downlink communication. The remaining 16 hours operational time will lead to a reduction of cross-over points to $N = 480,220$. Nonetheless, the pattern of the tidal potential can be clearly recognized. Note that the figure also contains cross-over points provided by the Ganymede flybys, which appear on the chart as equatorial stripes in the eastern hemisphere. The similar looking stripes in the northern hemisphere belong to the high elliptical insertion phase. While in the white areas no data is available from cross-over measurements, the black pattern is formed by areas where the two height measurements are performed at the same tidal phase. These black spots do not contribute to the tidal measurement but have the potential to help with the calibration of the instrument and to provide additional constraints on the orbit errors for those tracks.

4.2.3. General Model Description

Since at a cross-over point with the surface coordinates (θ, ϕ) the static topography cancels out, the difference of the range measurements du at each cross-over point can be expressed as

$$du = \frac{h_2}{g}(\Phi_1(r,\theta,\phi,t_1) - \Phi_2(r,\theta,\phi,t_2)) + dr_{n1} - dr_{n2}. \tag{4.5}$$

The two measurements originate from two passes over this point at the times t_1 and t_2. It has been

Parameter	Symbol	Unit	BELA	GALA
Energy	E_t	mJ	50	17
Wavelength	λ_t	nm	1064	1064
Frequency	f_q	Hz	10	30
Pulsewidth	σ_0	ns	3.4	2.9
Divergence (full cone)	Θ_T	μrad	50	100
Telescope radius	r_R	cm	10	12.5
Field of view (full cone)	Θ_{FOV}	μ rad	495	450
Optical efficiency	ϵ_{RO}		0.84	0.85
Optical filter efficiency	ϵ_{RF}		0.8	0.8
Optical filter bandpass	σ_{RF}	nm	2	2
Quantum efficiency	ϵ_{QE}		0.36	0.36
APD dark current (bulk)	I_{DB}	pA	50	50
APD dark current (surface)	I_{DS}	nA	20	20
Maximum gain	M		150	150
TIA bandwidth	B_0	MHz	20	100
Digital filter width	σ_f	ns	5-60	5-60

Table 4.2: Comparison between the BELA and assumed GALA instrument parameters.

shown useful in practice to add a large number of parameters representing vertical orbit errors at the orbital frequency of the spacecraft (compare to Mazarico et al. (2014a)). Here, the orbit errors are modeled by a sine function and a constant term. The error dr_n of the n-th spacecraft orbit is therefore given by

$$dr_n(t) = A_n \sin(\omega_n t + \phi_n) + C_n \quad (4.6)$$
$$= U_n \sin(\omega_n t) + V_n \cos(\omega_n t) + C_n, \quad (4.7)$$

with $U_n = A_n \cos(\phi_n)$ and $V_n = A_n \sin(\phi_n)$. While the sine term represents a periodic orbit error at the orbital period, the constant C_n also accounts for distortions at longer periods which can, however, be assumed as constant on the time scale of one spacecraft orbit ($\approx$ 3 to 4 hours). For the sake of internal consistency, we require that the orbit corrections of neighboring orbits are continuous at the connecting points

$$dr_n(2\pi/\omega_n) = dr_{n+1}(0). \quad (4.8)$$

Inserting eq. 4.7 in eq. 4.8 results into the constraint

$$V_n - V_{n+1} + C_n - C_{n+1} = 0. \quad (4.9)$$

Eq. 4.5 together with the constraints of eq. 4.9 formulates a linear model which can be solved by a least-squares adjustment. The unknown parameters forming the parameter vector $\mathbf{x}$ are h_2 and one set of U_n, V_n and C_n for each orbit. While the design matrix $\mathbf{A}$ is composed of the derivatives of eq. 4.5 with respect to the parameters, $\mathbf{B}$ contains the constraints given by eq. 4.9. The solution of the problem is given by

$$\begin{pmatrix} \mathbf{x} \\ \mathbf{-k} \end{pmatrix} = \begin{pmatrix} \mathbf{A}^T\mathbf{A} & \mathbf{B}^T \\ \mathbf{B} & \mathbf{0} \end{pmatrix}^{-1} \begin{pmatrix} \mathbf{A}^T\mathbf{O} \\ \mathbf{0} \end{pmatrix} = \mathbf{N}^{-1} \begin{pmatrix} \mathbf{A}^T\mathbf{O} \\ \mathbf{0} \end{pmatrix}. \quad (4.10)$$

Here $\mathbf{O}$ contains the observations on each cross over point and $\mathbf{k}$ are the Lagrange multipliers solving the system. However, in this particular case we are not aiming at solving for the parameter vector $\mathbf{x}$ since no observations are available yet. Instead we are foremost interested to determine how sensitive to h_2 the measurement is. Such a covariance analysis is justified here since the model is linear in h_2 while, by introducing several degrees of freedom, still having the necessary degree of complexity in order not to underestimate the error. The sensitivity we define as $\Gamma = 1/\sqrt{\left(\mathbf{N}^{-1}\right)_{h_2}}$, where $\left(\mathbf{N}^{-1}\right)_{h_2}$ denotes the matrix element of $\mathbf{N}^{-1}$ associated with the h_2 parameter. Assuming that the mean altitude measurement error is σ_z and since one tidal measurement consists of two altitude measurements the error estimate of h_2 is then:

$$\Delta h_2 = \frac{\sqrt{2} \cdot \sigma_z}{\Gamma} = \sqrt{2\left(\mathbf{N}^{-1}\right)_{h_2}} \cdot \sigma_z. \quad (4.11)$$

The accuracy of the measurement of the h_2 value is therefore dependent on two main components:

- The number and distribution (in space and time) of cross-over points available for evaluation after the mission lifetime. This point is driven by the orbit, the mission lifetime and

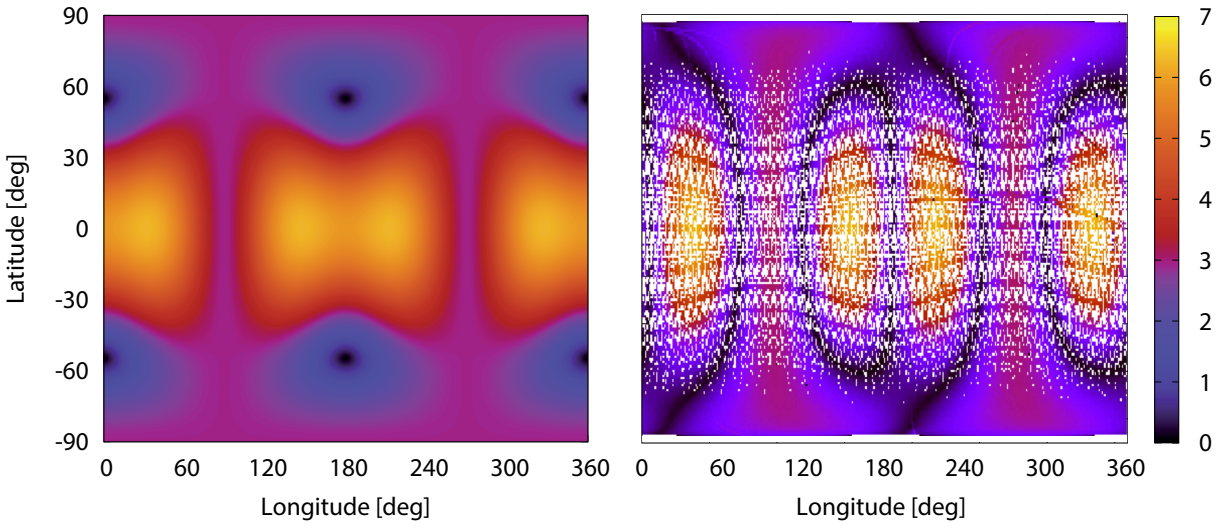

Figure 4.1: Expected tidal double amplitudes on Ganymede in the presence of a global ocean (left) and maximal measurable amplitudes by the cross-over technique based on the JUICE trajectory and projected on Ganymede's surface (right).

the operation scenario for the instrument and can be expressed by the sensitivity factor Γ.

- The accuracy of one tidal measurement which is dependent on the error budget driven by the instrument and spacecraft performance and expressed by the mean measurement error σ_z.

The mean measurement error must be assessed by analyzing the single error sources, where the first one is the instrument itself and can be quantified by an instrument performance model.

4.2.4. Instrument Performance Model

The BELA and GALA instrument are both designed for harsh, though very different environments. While BELA must be expected to face hot temperatures in the proximity of the Sun, GALA will investigate Jupiter's icy moons in a cold, irradiated environment, additionally restricted by low power and downlink budgets. However, besides the thermal and mechanical design which is adapted to the respective environment, the working principle of both instruments follows the same baseline design. While a general performance model for laser altimetry has been provided by Gardner (1992), the model used in this study is based on the performance model developed for BELA in order to account for the specific instrument design and the special needs of modeling the signal of a digital laser altimeter. The complete model is described in detail in Gunderson et al. (2006) and in Gunderson and Thomas (2010). It is a predominantly analytical model taking into account a wide set of instrument parameters as well as the surface roughness, albedo, illumination conditions and spacecraft position. It allows computing the signal to noise ratio (SNR) as well as the single shot probability of false detection (PFD). From the SNR an estimate for the ranging accuracy can be obtained which will provide the instrument error for the present analysis.

4.2.5. Spacecraft Pointing Error

In addition to the instrumental error, a significant contribution to the overall error budget comes from the pointing accuracy. Here we distinguish three different pointing errors. First the absolute pointing error $\Delta\Phi$ which is the difference between the intended pointing angle and the measured pointing angle. This error has no contribution to the error budget since it can be measured by the star tracker of the spacecraft and is therefore known. The second pointing angle is the inertial spacecraft pointing knowledge $\Delta\phi_i$, which is the difference between the measured pointing angle and the actual pointing angle. We assume that this error is < 10 arcsec. The third angle is the guidance pointing angle $\Delta\phi_g$ which is the result of the uncertainty in the tra-

jectory of the spacecraft in cross- and along-track direction. A value of 20 arcsec has been taken here, which corresponds to an orbit knowledge along and cross-track on the order of 20 m. Further, it has to be considered that the line of sight of the instrument will not be perfectly co-aligned to the nadir axis of the spacecraft inertial frame. This misalignment, even if measured on ground, is subject to change due to vibrations at launch and therefore needs to be calibrated in cruise. The possible options to realise this are by laser ranging to Earth or by cross-calibration with a camera system (e.g. the navigation camera or the JANUS instrument). The residual of the calibration $\Delta\phi_a$ by laser ranging is limited by the inertial pointing error of the spacecraft and the beam divergence of GALA. The resulting error due to misalignment is therefore estimated to be 14 arcsec. All pointing and alignment errors can be assumed to be uncorrelated so that the total pointing error is

$$\Delta\phi = \sqrt{\Delta\phi_i^2 + \Delta\phi_g^2 + \Delta\phi_a^2}. \tag{4.12}$$

The error in the range measurement due to the pointing knowledge can now be expressed as a function of the spacecraft altitude H and the surface slope α as

$$\delta z_{\text{point}} = H \tan(\Delta\phi) \tan(\alpha). \tag{4.13}$$

This expression is consistent with that of Gardner (1992) and will present one of the major contributions to the range measurement error.

4.2.6. Other Error Sources

Further contributions to the error budget come from the finite shot frequency f_q (30 Hz in the nominal operation mode). The laser footprints are not necessarily situated directly on the cross-over point but in order to get the corresponding height the adjacent footprints must be used for interpolation. This results in an interpolation error also dependent on the surface slope α and the spacecraft ground velocity v with a maximum value of

$$\delta z_{\text{interp}} = \frac{v}{2f_q} \tan\alpha. \tag{4.14}$$

4.2.7. Numerical Simulation

To assess the mean measurement error σ_z of the cross-over measurements over the mission lifetime, we first determine all cross-over points including their altitude, coordinates on the surface, phase angle to the Sun and the spacecraft velocity over ground. However, for the quantitative determination of the error contributions described in section 4.2.4 to 4.2.6 also the surface slope is required. Since this information is not available on footprint scale ($\approx$ 50m) we use global slope distributions derived from Voyager and Galileo data (Berquin et al., 2013). The slope is then assigned statistically but following Ganymede-specific slope statistics. During the mission lifetime we will have on the order of 10^5 cross over points, thereby justifying the use of a Monte Carlo simulation in which errors are randomised, assuming an error-specific distribution for the contributions given in sections 4.2.4 to 4.2.6. The pointing error is assumed to jitter around the intended pointing angle leading to a Gaussian distribution. The interpolation error depends on the distance between the cross-over point and the closest laser footprint of a given track. We assume that this distance is equally distributed between zero and the half of the maximum distance betweeen two laser spots making a linear distribution of the interpolation errors plausible. An overview of all included errors with their assigned distribution is given in table 4.3.

4.3. Application and Results for the GALA Experiment

4.3.1. Measurement Error

For the numerical model we derive the altitude and illumination conditions from the JUICE trajectory and assign a slope according to the given statistics to all the cross-over points. The instrument error can then be estimated by calculating the SNR according to equation (26) in Gunderson and Thomas (2010). The main environmental factors influencing the instrument accuracy are the spacecraft altitude, the surface roughness on footprint scale and the solar infrared noise. However, the latter can be seen as the smallest influence in the case for the GALA instrument due to the large distance from the Sun. The rangefinder module of GALA is able to detect a signal within a SNR of 1 in order of magnitude. Assuming an albedo of 0.44 and the instrument characteristics in Tab. 4.2 the detection limit is at about 1600 km altitude for a surface with moderate slope while decreasing with rising surface roughness as shown in Fig. 5.3.1. For the circular orbits around Ganymede at almost constant altitude we considered the PFD for different albedo values A

Error source	Symbol	Slope dependent	Distribution
Instrument error	σ_{instr}	yes	Gaussian
Pointing error	σ_{point}	yes	Gaussian
Other errors	σ_{misc}	no	Constant
Interpolation error	σ_{interp}	yes	Linear

Table 4.3: Overview on the error contributions and applied statistics

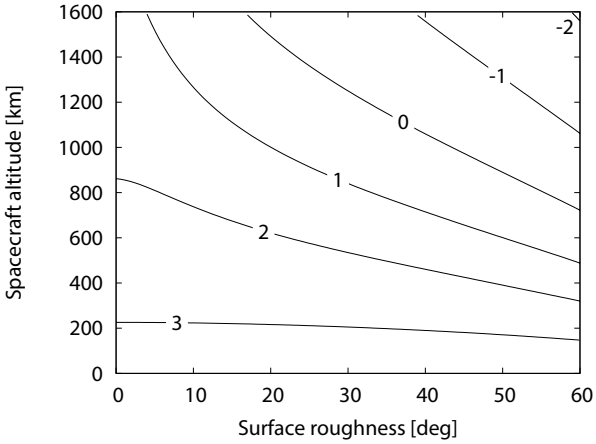

Figure 4.2: Contours of decadic logarithm of the SNR as a function of spacecraft altitude and surface roughness.

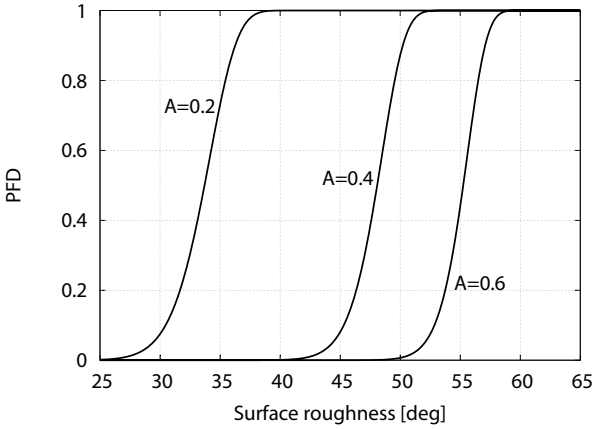

Figure 4.3: Single shot probability of false detection (PFD) in dependence of the surface roughness. Shown are three different cases for albedo values ranging from 0.2 corresponding to dark terrain on Ganymede's surface to 0.6 for fresh icy terrain.

from 0.2 to 0.6. Due to albedo variations it is required that the instrument is able to operate for the defined worst case condition of $A = 0.2$. If we translate the SNR into a PFD according to equation (43)-(49) in Gunderson et al. (2006) for the 500 km orbit, the PFD is < 0.1 for areas with 30° surface roughness (Fig. 4.3), which is considered to be the detection limit for operation in this study. For higher albedo values, even pulses returned from terrain with roughness up to 53° can be detected. The numerical analysis has been performed using 100 simulation runs, a number which led to sufficiently stable results. The numerical results of the error budget are reported in table 4.4.

The sensitivity Γ of the h_2 determination to the calculated measurement error can be assessed numerically according to section 4.2.3. Note that since the model is linear in h_2 the sensitivity factor is independent of the actual h_2 value but depends on the number and distribution of cross-overs available for the analysis and is therefore dependent on the mission and operational scenario. We consider a scenario where GALA is operating continuously except 8h per day, which are reserved for downlink communication. Starting from this orbit scenario one can assess the respective number of cross-overs available for the post-processing and derive the sensitivity of the h_2 value with respect to the range measurement errors. In this specific case, we obtain:

$$\Gamma = 342.70.$$

Inserting Γ and the calculated mean measurement error from table 4.4 in equation 4.11, we get an estimate for the error in the h_2 determination of

$$\Delta h_2 = 0.026$$

for the assumed operational scenario.

4.3.2. Implication on the Ice Thickness

The numerical model of the GALA experiment provides an estimate of the accuracy of the h_2 measurement based on a combination of the predicted instrument performance and the amount and distribution of cross-over points on Ganymede's surface. The measurement error of a single cross-over

Error source	Symbol	Mean value [m]	Standard deviation [m]
Instrument	σ_{instr}	1.45	<0.01
Pointing & alignment	σ_{point}	5.72	0.02
Interpolation	σ_{interp}	1.80	<0.01
Others	σ_{misc}	1.6	-
Total mean error	σ_z	6.38	0.03

Table 4.4: Total error budget for GALA. The single error contributions are assumed to be uncorrelated so the total mean error has been calculated by the square sum.

point is on average 6.4 m. Assuming a continuous operation (interrupted by 8h downlink per day) in orbit around Ganymede, this leads to a total error of 2.0% in h_2 (assuming h_2=1.3). This accuracy is sufficient to unambiguously confirm or disprove the existence of an ocean underneath Ganymede's outer ice shell. Furthermore it can be used to constrain the thickness of the ice shell in the presence of an ocean.

Table 4.5 shows a plausible structural model for Ganymede's interior consistent with the total mass and mean moment of inertia (MoI) as measured by the Galileo mission (Anderson et al., 1998). Computing the Love number h_2 for this model using a fully elastic rheology with varying ocean thickness, the error of h_2 can be directly translated in an error of the outer ice shell thickness. For the computation of h_2 a numerical integration of the linearized field equations has been used (Segatz et al., 1988; Wieczerkowski, 1999; Hussmann et al., 2011). Fig. 4.4 shows the dependence of the ice thickness for the model of table 4.5. An accuracy of ±2.0% leads to a constraint on the ice-I thickness down to less than ± 20 km. In the first instance this result must be regarded with caution due to specific assumptions in the numerical model. In particular the impact of the operation scenario, structural model, viscosity, and rigidity will be discussed in the next section.

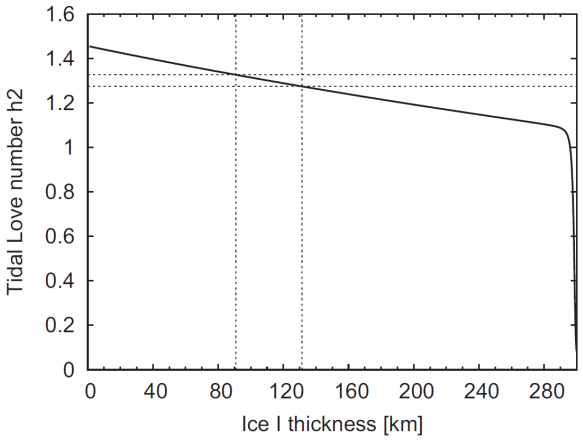

Figure 4.4: Dependence between the thickness of Ganymede's outer ice shell and radial displacement tidal Love number h_2.

Layer	Radius [km]	Density [kg/m^3]
Core	800	5900
Mantle	1881	3080
HP-ice	2331	1310
Ocean & ice-I	2631.2	1000

Table 4.5: Reference model of Ganymede's interior structure.

4.4. Discussion

4.4.1. Operation Scenario

The sensitivity of the measurements on h_2 is highly dependent on the operational time. Since every orbit track intersects most of the other orbit tracks, the number of cross-over points increases significantly with each additional orbit leading to a quadratic growth of the available data. Thus, at the beginning of the 500 km orbit phase the error on the h_2 measurement decreases rapidly. Fig. 4.5 shows how the accuracy of the measurement would evolve over time in the case of a mission extension. Even if the curve asymptotically approaches zero, it would be necessary to double the mission time in order to halve the error of h_2. On the other side, a reduction of the operational time due to resource constraints, e.g. power, data or due to technical failures on instrument or spacecraft level would have a severe impact on the h_2 determination. Nonetheless the significant amplitude of the radial tides allows the determination of h_2 within a remarkable short

period of time considering the short mission time in Ganymede's orbit.

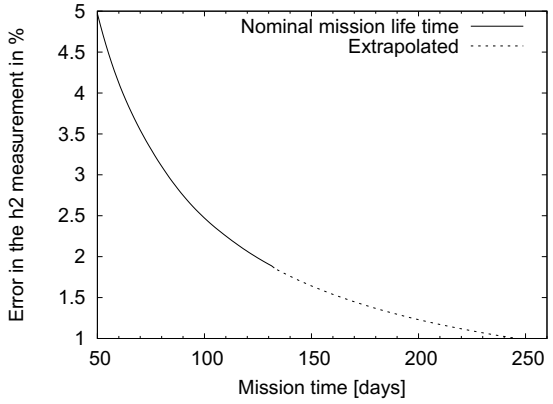

Figure 4.5: Error in the h_2 measurement assuming a value of h_2=1.3 in dependence of the mission time. The thick line shows the analysis result for the nominal mission lifetime of 132 days, while the dotted line represents an extrapolation for the 500 km orbit.

4.4.2. Dependence on the Slope Distribution

Little information about the slope distribution on Ganymede is known at footprint scale. This work assumes the distribution for bright terrain (Berquin et al. (2013), Fig. 3), covering the largest area in the available data, to be globally representative. However, locally, as for the Arbela or Harpagia Sulcus vicinity, also larger slopes are reported. In order to test the effect of different slope distributions on the performance model, we repeated the analysis increasing the slope by 20 % and 50 %. Also a scenario with 20 % lower slopes has been tested.

The distribution only affects the instrument error budget, so the range measurement, and not the sensitivity of the measurement since the latter is only dependent on the operation scenario. The relation can be approximated as linear resulting in a 50 % higher error in h_2 if the slope distribution is globally 50 % higher.

Distribution	**Range Error [m]**	h_2 **Error**
Slope - 20%	5.22	1.7%
Nominal	6.38	2.0%
Slope + 20%	7.55	2.4%
Slope + 50%	9.38	3.0%

Table 4.6: Slope dependence of the error budget

4.4.3. Ambiguity in the Structural Model

The model described in the previous section gives an overview on the capabilities of the GALA instrument to infer the ice-I thickness assuming a specific structure and a fully elastic rheological model. However, we did not yet account for a set of factors that influence the interpretation of a measured h_2 value.

The knowledge of the satellite's total mass and mean moment of inertia still leaves a substantial degeneracy of structural models usually compensated by further (i.e. physical or cosmochemical) assumptions. In order to test how the possible diversity of structural models would affect the relation between the h_2 and the ice-I thickness, we calculated 700 structural models all consistent with Ganymede's mass and mean moment of inertia. We therefore assumed a wide parameter range for the thicknesses and densities of each layer. We intentionally avoided implementing additional constraints, like cosmochemical arguments. Only the requirement that Ganymede's water ice/liquid content should be greater than 40 % has been added to discard possible solutions that would not represent an icy moon anymore. The assumed parameter range is shown in table 4.7. As a result, the linear behaviour of the h_2 vs. ice thickness is now overlayed by a jitter making the constraint on the ice-I thickness less tight, i.e. from $\pm$20 km to $\pm$30 km, when using h_2 only.

4.4.4. Linear Combination of h_2 and k_2

One alternative solution to constrain the ice thickness with the same accuracy consists in combining the GALA data with data from the radio science experiment 3GM. Wahr et al. (2006) showed that the ice thickness can be further constrained when using a linear combination of h_2 and the tidal potential Love number k_2 which can be inferred from radio science observations. Fig. 4.7 shows the linear combination $1 + k_2 - h_2$ as a function of the ice-I thickness for the same models shown in Fig 4.6. Assuming that k_2 will be known with an accuracy of 10^{-3} (Parisi et al., 2014), the ice-I thickness

Layer	Thickness [km]	Density [kg/m^3]	Comment
Core	200 - R/2	5000-8000	FeS-Fe composition
Mantle	-	2400 - 3500	hydr. Si to "Io-rock"
HP-ice	depth>120*	1100-1300	
Ocean	-	1000-1050	dep. on salinity
Ice-I	depth<120*	900-1000	dep. on e.g. dust content

Table 4.7: Constraints for the structural models. The mantle and ocean thicknesses are only constrained by the total mass and the mean moment of inertia. *(Spohn and Schubert, 2003)

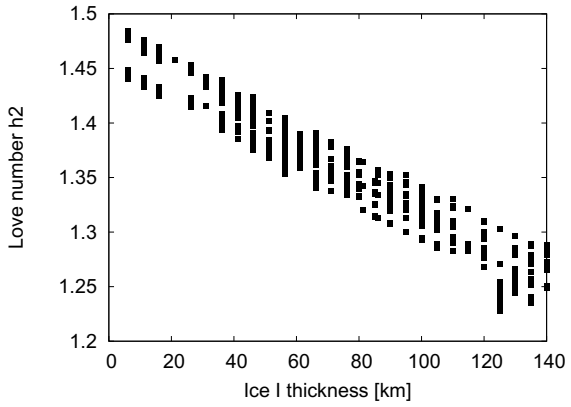

Figure 4.6: Love number h_2 in dependence of the outer ice shell thickness. Each point represents an interior model consisent with Ganymede's mass and MoI.

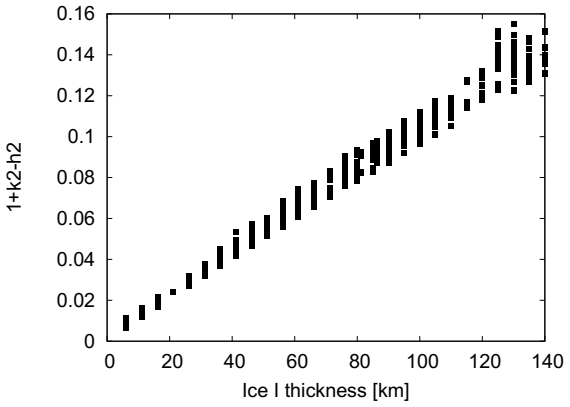

Figure 4.7: Linear combination of k_2 and h_2 in dependence of the outer ice thickness.

can be constrained to ± 20 km without additional constraints on the structural models.

4.4.5. The Elastic Case vs. the Visco-elastic Case

In addition to the thickness of the outer ice shell, h_2 will depend on the rigidity μ and viscosity η of the outer ice-I shell. While we can assume the rigidity of ice-I to be fairly well constrained (Sotin et al. (1998) gives a value between 3.3 and 3.6 GPa) the viscosity must be considered as an unknown parameter mainly due to its strong dependence on temperature. Assuming a Maxwell-rheology as a basic model, the visco-elastic part of the deformation can be calculated using the formalism developed for the purely elastic response, if the rigidity μ is replaced by the complex shear modulus $\widetilde{\mu}$ given by Zschau (1978)

$$\widetilde{\mu} = \frac{in\mu}{in + 1/\tau}. \tag{4.15}$$

n is the frequency of the tidal forcing, i.e. Ganymede's mean motion, $i = \sqrt{-1}$, and $\tau = \eta/\mu$ the characteristic Maxwell-time. We can distinguish three different regimes: (1) the elastic regime in with $\tau \to \infty$, implying $\eta \to \infty$ and $\widetilde{\mu} \to \mu$, (2) the visco-elastic regime with $\tau \approx n$ and (3) the fluid regime with $\tau \to 0$, implying $\eta \to 0$ and $\widetilde{\mu} \to 0$. Applied to the case of Ganymede with a mean motion of $n = 1.0164 \times 10^{-5}\mathrm{s}^{-1}$ and a rigidity of 3.3 GPa the viscosity η would have to be on the order of 10^{14} Pa s for the response to be visco-elastic. For $\eta \gg 10^{14}$ Pa s the ice would respond elastically and for $\eta \ll 10^{14}$ Pa s the material would be in the fluid regime. For the latter case, however, it is questionable that the Maxwell model chosen here is applicable. The needed viscosities of $\ll 10^{14}$ Pa s would imply relatively high temperatures inside the outer ice shell which seems inconsistent with geologic evidences (Pappalardo et al., 2004). Furthermore, Spohn and Schubert (2003) investigated heat conduction and thermal convection mechanisms for Jupiters icy satellites. For the case of low viscosities, it was shown for Ganymede that, in contrast to the Europa case, thermal equilibrium can only be reached for thin ice layers. Instead, equilibrium

temperatures at Ganymede's surface are of the order of 126 K (Moore and Schubert, 2003), implying viscosities many orders of magnitude greater than 10^{14} Pa s. We therefore may expect that the outer ice shell responds elastically to the external tidal forcing. Its response is controlled by the elastic rigidity only and is independent from the viscosity value. Though, at the lower boundary of the ice shell (top of the ocean) where the ice is close to the melting point we can expect viscosities on the order of 10^{13} Pa s (or 10^{14} Pa s at most) which are in the fluid regime for the given forcing. However, unless there is a layer of substantial thickness with viscosities around 10^{14} Pa s, the response will be dominated by the elastic contribution, justifying our previous assumption to neglect the visco-elastic contributions. Only in case of a substantial layer with a viscosity around 10^{14} Pa s the response of the ice shell would be dominated by visco-elasticity and the outer elastic part would follow the visco-elastic deformation inside the ice shell. We will investigate this very special case in further studies. In the visco-elastic case, the response would show a significant phase-lag on the order of 1° which could be measurable by GALA under certain circumstances. We will investigate the sensitivity of the GALA instrument to lateral displacements (e.g. phase lags) of the tidal pattern and the possible constraints that could be put on the viscosity in a separate study.

4.5. Conclusion

A key measurement of GALA will be to measure the radial deformation of Ganymede's outer ice shell. The range measurement error of the instrument will be < 2 m, on average, while showing good signal to noise ratios even on rough or dark surfaces. When measuring tidal deformations using the cross-over approach, other errors have to be considered, thereby leading to a total mean error of 6 to 7 m. The highest uncertainty arises from pointing and alignment errors even if presuming that the instrument will be calibrated in cruise. An improvement of this aspect would appreciably improve the tidal measurements. Further improvement could be achieved by a mission extension in a lower (e.g. 200 km) orbit leading to more orbits and therefore to more cross-over points per time. The sensitivity of the measurement to the tidal Love number h_2 is given by the number and distribution of cross-over points available for the evaluation. While the distribution is settled by the polar orbit, resulting in a dense concentration of cross-over points in the polar regions, the number is dependent on the final operation time. Assuming the nominal 132 days in a circular 500 km orbit, we end up with a measurement error of h_2 of 2.0 % in the case an sub-surface ocean is present. By measuring h_2 the thickness of Ganymede's outer ice shell can be constrained. Assuming an elastic Maxwell model we can constrain the ice thickness to ±20 km for a given structural model. Considering the uncertainty in Ganymede's interior structure the constraint is less tight (± 20–30 km), but can be recovered using a linear combination of h_2 with the tidal potential Love number k_2 in order to compensate for this uncertainty. Further investigations will focus on possibilities to use GALA for better constraining the ice-I thickness even in the visco-elastic case simultaneously with the ice viscosity. For viscosities below 10^{15} Pa s phase, lags would be sufficiently large and probably detectable by GALA. Finally it should be noted that GALA will form an integral part of a larger geodesy and geophysics instrument package, incorporating radio science, stereo imaging, sub-surface radar and a magnetometer. This synergy between different instruments will allow to further constrain the ice thickness.

Acknowledgements

We would like to thank Karsten Seiferlin and Nick Thomas for their helpful comments and two anonymous reviewers for improving the manuscript. JO greatly acknowledges being hosted by MIIGAiK and supported by the Russian Science Foundation under project 14-22-00197.

References

JD Anderson, G Schubert, RA Jacobson, EL Lau, WB Moore, and WL Sjogren. Europa's differentiated internal structure: Inferences from four Galileo encounters. *Science*, 281(5385):2019–2022, 1998.

Y. Berquin, W. Kofman, A. Herique, G. Alberti, and P. Beck. A study on Ganymede's surface topography: Perspectives for radar sounding. *Planetary and Space Science*, 77(0):40 – 44, 2013. 10.1016/j.pss.2012.07.004.

C.S. Gardner. "Ranging Performance of Satellite Laser Altimeters". *"IEEE Transactions on Geo-*

science and Remote Sensing", 30 No 5:1061–1072, 1992.

O. Grasset, M.K. Dougherty, A. Coustenis, E.J. Bunce, C. Erd, D. Titove, M. Blanc, A. Coates, P. Drossart, L.N. Fletcher, H. Hussmann, R. Jaumann, N. Krupp, J.-P. Lebreton, O. Prieto-Ballesteros, P. Tortora, F. Tosi, and T. Van Hoolst. JUpiter ICy moons Explorer (JUICE): An ESA mission to orbit Ganymede and to characterise the Jupiter system. *Planeary and Space Science*, 78, 2013. 10.1016/j.pss.2012.12.002.

K. Gunderson and N. Thomas. BELA receiver performance modeling over the BepiColombo mission lifetime. *Planetary and Space Science*, 58: 309–318, 2010.

K. Gunderson, N. Thomas, and M. Rohner. A laser altimeter performance model and its application to BELA. *"IEEE Transactions on Geoscience and Remote Sensing"*, 44 No 11:3308–3319, 2006.

H. Hussmann, F. Sohl, and J. Oberst. Measuring tidal deformations at Europa's surface. *Advances in Space Research*, 48:718–724, 2011. 10.1016/j.asr.2010.06.001.

W.M. Kaula. Tidal dissipation by solid friction and the resulting orbital evolution. *Reviews of Geophysics*, 2:661–685, 1964. 10.1029/RG002i004p00661.

M.G. Kivelson, K.K. Khurana, and M. Volwerk. The permanent and inductive magnetic moments of Ganymede. *Icarus*, 157:507–522, 2002. 10.1006/icar.2002.6834.

E. Mazarico, M.K. Barker, G.A. Neumann, M.T. Zuber, and D.E. Smith. Detection of the lunar body tide by the Lunar Orbiter Laser Altimeter. *Geophysical Research Letters*, 41, 2014. 10.1002/2013GL059085.

W.B. Moore and G. Schubert. The tidal response of Europa. *Icarus*, 147:317–319, 2000.

W.B. Moore and G. Schubert. The tidal response of Ganymede and Callisto with and without liquid water oceans. *Icarus*, 16:223–226, 2003.

R.T. Pappalardo, G.C. Collins, J.W. Head, III, P. Helfenstein, T.B. McCord, J.M. Moore, L.M. Prockter, P.M. Schenk, and J.R. Spencer. *Geology of Ganymede*, pages 363–396. 2004.

M. Parisi, L. Iess, and S. Finocchiaro. The gravity fields of Ganymede, Callisto and Europa: how well can JUICE do? *Geophysical Research Abstracts*, EGU2014:11758, 2014.

Joachim Saur, Stefan Duling, Lorenz Roth, Xianzhe Jia, Darrell F. Strobel, Paul D. Feldman, Ulrich R. Christensen, Kurt D. Retherford, Melissa A. McGrath, Fabrizio Musacchio, Alexandre Wennmacher, Fritz M. Neubauer, Sven Simon, and Oliver Hartkorn. The search for a subsurface ocean in Ganymede with Hubble Space Telescope observations of its auroral ovals. *Journal of Geophysical Research: Space Physics*, 120(3):1715–1737, 2015. 10.1002/2014JA020778.

G. Schubert, K. Zhang, M.G. Kivelson, and J.D. Anderson. The magnetic field and internal structure of Ganymede. *Nature*, 384:544–545, 1996. 10.1038/384544a0.

G. Schubert, J.D. Anderson, T. Spohn, and W.B. McKinnon. *Jupiter. The Planet, Satellites and Magnetosphere*, chapter Interior composition, structure and dynamics of the Galilean satellites, pages 281–306. Cambridge University Press, 2004.

M. Segatz, T. Spohn, M.N. Ross, and G. Schubert. Tidal dissipation, surface heat flow, and figure of viscoelastic models of Io. *Icarus*, 75:187–206, 1988. 10.1016/0019-1035(88)90001-2.

F. Sohl, T. Spohn, D. Breuer, and K. Nagel. Implications from Galileo observations on the interior structure and chemistry of the Galilean satellites. *Icarus*, 157(1):104 – 119, 2002. ISSN 0019-1035. http://dx.doi.org/10.1006/icar.2002.6828.

C. Sotin, O. Grasset, and S. Beauchesne. *Solar system ices*, chapter Thermodynamic properties of high pressure ices: Implications for the dynamics and internal structure of large icy satellites, pages 79–96. Springer Netherlands, 1998. 10.1007/978-94-011-5252-5-4.

T. Spohn and G.. Schubert. Oceans in the icy Galilean satellites of Jupiter? *Icarus*, 161:456–467, 2003. 10.1016/S0019-1035(02)00048-9.

N. Thomas, T. Spohn, J.-P. Barriot, W. Benz, G. Beutler, U. Christensen, V. Dehant, C. Fallnich, D. Giardini, O. Groussin, K. Gunderson, E. Hauber, M. Hilchenbach, L. Iess, P. Lamy, L.-M. Lara, P. Logonne, J.J. Lopez-Moreno, H. Michaelis, J. Oberst, D. Resendes, J.-L. Reynaud, R. Rodrigro, S. Sasaki, K. Seiferlin, M. Wieczorek, and J. Whitby. The BepiColombo

Laser Altimeter (BELA): Concept and baseline design. *Planetary and Space Science*, 55:1398–1413, 2007. 10.1016/j.pss.2007.03.003.

S. Vance, M. Bouffard, M. Choukroun, and C. Sotin. Ganymede's internal structure including thermodynamics of magnesium sulfate oceans in contact with ice. *Planetary and Space Science*, 96:62–70, 2014. 10.1016/j.pss.2014.03.011.

J. Wahr, Z.A. Selvans, M.E. Mullen, A.C. Barr, G.C. Collins, M.M. Selvans, and R.T. Pappalardo. Modeling stresses on satellites due to nonsynchronous rotation and orbital eccentricity using gravitational potential theory. *Icarus*, 200:188–206, 2009. 10.1016/j.icarus.2008.11.002.

J.M. Wahr, M.T. Zuber, D.E. Smith, and J.I. Luine. Tides on Europa, and the thickness of Europa's icy shell. *Journal of Geophysical Research*, 111: E12005, 2006. 10.1029/2006JE002729.

K. Wieczerkowski. Gravito-Viscoelasto-dynamics for generalized rheologies with applications to Jupiter's Moon Io and the Earth. *Deutsche Geodaetische Kommission*, Reihe C 515, 1999.

Xiaoping Wu, Yoaz E. Bar-Sever, William M. Folkner, James G. Williams, and James F. Zumberge. Probing Europa's hidden ocean from tidal effects on orbital dynamics. *Geophysical Research Letters*, 28(11):2245–2248, 2001. ISSN 1944-8007. 10.1029/2000GL012814.

J. Zschau. *Tidal Friction and the Earth's Rotation*, chapter Tidal Friction in the Solid Earth: Loading Tides Versus Body Tides, pages 62–94. Springer Berlin Heidelberg, 1978. 10.1007/978-3-642-67097-8-7.

Chapter 5

Research Paper IV

Assessing the potential for measuring Europa's tidal Love number h_2 using radar sounder and topographic imager data

G. Steinbrügge[1], D.M. Schroeder[2], M.S. Haynes[3], H. Hussmann[1], C. Grima[4], D.D. Blankenship[4]

[1]German Aerospace Center, Institute of Planetary Research, D-12489 Berlin, Germany
[2]Department of Geophysics, Stanford University, Stanford, CA, USA
[3]Jet Propulsion Laboratory, California Institute of Technology, Pasadena, CA, USA
[4]Institute for Geophysics, University of Texas at Austin, Austin, TX, USA

Published in Earth and Planetary Science Letters, Volume 482, Pages 334–341
doi: 10.1016/j.epsl.2017.11.028
Postprint

Abstract

The tidal Love number h_2 is a key geophysical measurement for the characterization of Europa's interior, especially of its outer ice shell if a subsurface ocean is present. We performed numerical simulations to assess the potential for estimating h_2 using altimetric measurements with a combination of radar sounding and stereo imaging data. The measurement principle exploits both delay and Doppler information in the radar surface return in combination with topography from a digital terrain model (DTM). The resulting radar range measurements at cross-over locations can be used in combination with radio science Doppler data for an improved trajectory solution and for estimating the h_2 Love number. Our simulation results suggest that the accuracy of h_2 from the joint analysis of REASON (Radar for Europa Assessment and Sounding: Ocean to Near-surface) surface return and EIS (Europa Imaging System) DTM data will be in the range of 0.04-0.17 assuming full radio link coverage. The error is controlled by the SNR budget and DTM quality, both dependent on the surface properties of Europa. We estimate that this would unambiguously confirm (or reject) the global ocean hypothesis and, in combination with a nominal radio-science based measurement of the tidal Love number k_2, constrain the thickness of Europa's outer ice shell to up to $\pm$15 km.

5.1. Introduction

The potential habitability of a subsurface ocean of Europa makes the second moon of Jupiter a high-priority target for planetary exploration. The National Aeronautics and Space Administration (NASA) plans to observe the icy satellite with a dedicated flyby tour over a period of several years. One of the top priorities of the Europa Clipper is the characterization of the structure of the icy shell (Pappalardo et al., 2015). It is a key measurement for future exploration and provides insights into the thermal state and interior dynamics of the moon. However, in order to effectively constrain the interior structure a combined analysis of multiple measurements will be necessary. Previous publications have already pointed out the importance of measuring both tidal Love numbers h_2 and k_2 to constrain the ice thickness, e.g. Wahr et al. (2006) and Wu et al. (2001). The tidal Love number k_2 describes the secondary potential induced by the mass redistribution as a consequence of the external forcing by Jupiter and the tidal Love number h_2 expresses the corresponding radial amplitude of the tidal deformation. While k_2 can be measured by radio science experiments, the assessment of h_2 requires altimetric measurements. One of the instruments onboard the Europa Clipper is the Radar for Europa Assessment and Sounding: Ocean to Near-surface (REASON). While its primary focus will be the direct detection of subsurface water reservoirs, we will show that it also has the potential to deliver altimetric measurements which can be used for the detection of solid body tides and therefore make an enhanced contribution to the characterization of Europa's outer ice shell. Further, with magnetometer, imaging and radio science data it constitutes a broader geophysics packet for revealing Europa's interior structure.

In the following section we will give an overview of the instrument and describe the proposed concept for altimetry measurements by combined stereo graphic camera and radar observations. This concept will be quantified by an analytic performance model and a variety of influences on the range measurement accuracy will be discussed in section 3. The resulting predictions for the ranging errors will then be incorporated in a numerical simulation of the flyby tour in section 4. Finally, the results and their potential contribution to the reconnaissance of Europa's interior will be discussed in section 5.

5.2. Instrument Description and Measurement Principle

REASON is a dual-band, nadir-pointed, interferometric radar sounder. It has a VHF band operating at 60 MHz with a 10 MHz bandwidth and an HF band operating at 9 MHz with a 1 MHz bandwidth. The chirp (radar pulse) length is adjustable between 30 and 100 μs. The radar is designed to characterize the surface and subsurface of Europa's ice shell by means of sounding, reflectometry, and altimetry (Blankenship et al., 2009; Moussessian et al., 2015). The instrument is composed of a two elements HF antenna mainly dedicated to penetrate the surface up to a depth of 30 km and four VHF antennas which allow to examine the upper ice layers and to perform altimetric measurements. The radius of the first pulse-limited footprint of the VHF is about 2.2 km from an altitude of 1000 km.

Over the Earth's oceans, radar instruments routinely achieve resolutions one magnitude better than their inherent range resolution (Garcia et al., 2014). However, the ocean is a generally flat surface which is well understood and therefore allows precise retracking of the altimeter waveforms. In application to planetary surfaces the topography can include much more complex structures making it difficult to discriminate the nadir return from surface clutter. However, this effect can be mitigated by utilizing additional knowledge of the topography at the footprint scale, e.g. from a stereo imagery derived digital terrain model (DTM) and by exploiting both the delay and Doppler information, in the surface return signal (Raney, 1998). In delay space, the principle uses the fact that on a flat surface a return from the n-th pulse-limited footprint will arrive before the return of the $(n+1)$-th pulse-limited footprint allowing them to be distinguished in the return signal. In the Doppler dimension footprints in along track direction can be separated according to their azimuth Doppler bin (figure. 5.1a,b). The size of such a delay/ Doppler cell is typically in the order of several hundreds of meters to a few kilometers.

Utilizing this information to map returns in delay/Doppler space to a known surface geometry or DTM simultaneously reduces any directional ambiguity in the rough-surface return and increases the number of usable "looks" or statistically independent observations of the surface (Raney, 2012). This allows the topography in each delay/Doppler cell to be seen as an individual range measurement (figure 5.1c). The accuracy of the range measurement on one delay/Doppler cell can then estimated

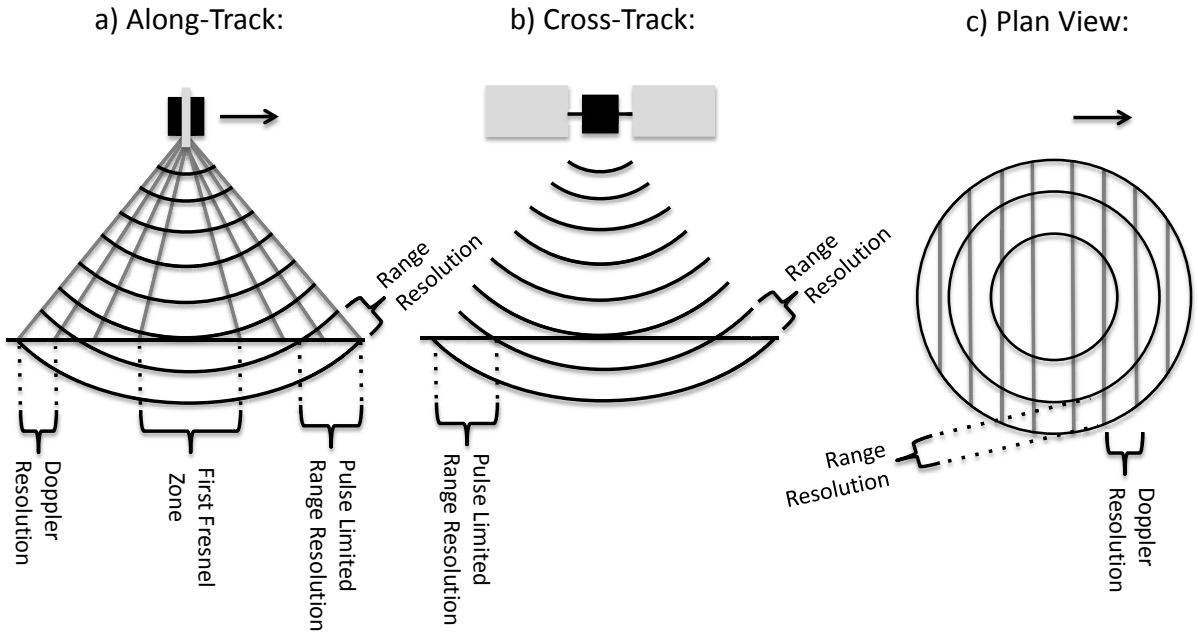

Figure 5.1: a) In along-track direction the pulse can be discriminated by the Doppler phase. b) Each pulse-limited footprint is delimited by the range resolution (one range-bin) and can be distinguished in the return signal by the respective time delay. c) Top view on the cross-over plate composed of multiple delay/Doppler cells. Each cell contributes as a statistically independent range measurement to the differential average height of the plate between the two flybys.

as

$$\sigma_z = \sqrt{\left(\frac{c}{2B}\right)^2 + \sigma_r^2 + \sigma_c^2}, \tag{5.1}$$

where σ_r and σ_c are the root mean square (rms) roughness within a delay/Doppler cell and the vertical resolution of the camera-derived, digital terrain model (DTM) respectively, c is the speed of light and B is the analog bandwidth of the radar. Because nadir-looking radar altimeters are nearly always limited by multiplicative (e.g. speckle, sidelobes, clutter) rather than additive noise, for the purposes of range estimate precision, the range error is rather constrained by the number of looks than by the signal to noise ratio (SNR) as long as the latter is above 1 (Raney, 2012). However, in case of a very rough surface the SNR can possibly drop with $1/R^4$ (see section 5.3.1) leading to a maximum useful altitude R of about 200 km. In contrast, on a flat surface the SNR can be very strong but only nadir returns are observed, eliminating azimuth processing and therefore multi-looking performance gains. Since precise information about the surface properties at the wavelength scale is lacking, both cases will be treated as separate possible end members bounding the likely performance over a realistic surface.

Here, we are mainly interested in retrieving a tidal signal of specific surface elements by measuring the differential ranges to a single area on the surface between two distinct points in time. A cross-over surface element is then defined by the geometry given by two spacecraft flybys over the same area. In order to measure tidal deformations cross-over based techniques are the method of choice since they cancel out any large scale topography effects (e.g. Mazarico et al. (2014a); Steinbrügge et al. (2015)). In the case of a radar sounder altimeter the cross-over surface element is a cross-over plate containing multiple delay/Doppler cells, rather than a point (as it is the case in laser-altimeter based cross-over approaches). Since the two passes can occur at different altitudes the contributing radar footprints and DTMs may be significantly different in size. However, using forward simulated radar data from a DTM allows our technique to fit the specific subset of the returns to selected cross-over areas within the DTM and therefore compare the same area on the surface even though observations are made from

different altitudes (Garcia et al., 2014). Each delay/Doppler cell inside the selected area will then be considered as one look (i.e. as a statistically independent observation). Having N uncorrelated looks on the surface, the total range measurement error of the cross-over plate would be $\sigma_z/\sqrt{N}$ (Raney, 2012).
To estimate the impact of stereo DTM resolution and extent on REASON altimetry for the Clipper we assume that wide angle camera (WAC) DTMs are available from altitudes lower than 1000 km and narrow angle camera (NAC) DTMs from altitudes up to 2600 km. Both cameras are part of the Europa Imaging System (EIS) (Turtle et al., 2016). In order to identify which DTM to use to simulate radar data for both flyby altitudes, we can select between up to four possible DTMs (NAC lower flyby, WAC lower flyby, NAC higher flyby, WAC higher flyby) which are constrained by the following requirements:

1. The altitude of the spacecraft at the cross-over location must be below the limit stated above for the respective camera;
2. The cross-over location must be illuminated by the Sun;
3. The vertical resolution of the DTM must be sufficient to ensure that the consecutive returns of the radar are not moved into other range bins than the ones predicted by the DTM;
4. The horizontal resolution of the DTM must be higher than the size of the outermost pulse-limited footprint within the cross-over plate portion of the DTM;
5. The size of the cross-over plate must not exceed the size of the DTM.

When applying these constraints to the cross-over locations of the trajectory the first three requirements reduce the amount of usable cross-overs. The latter two determine the shape and area of the cross-over plate and therefore the resulting ranging error for the remaining cross-overs. In general, it is desirable to have a cross-over plate as large as possible in order to benefit from the maximum number of looks. However, since the pulse-limited footprints become smaller with increasing distance from the center, the maximum usable size and therefore the minimal achievable range error will be limited by one of the requirements above. Although higher altitudes generally allow for larger cross-over plate areas, this effect is counteracted by increasing surface roughness within corresponding larger delay/Doppler cells. The balance of these competing effects depends on the character of the surface roughness. Further effects taken into account are possible systematic errors inside the DTMs as well as the illumination conditions and resulting shadowed areas. The latter is calculated for each cross-over plate as a function of surface roughness and solar incidence angle (section 5.3.2).

5.3. Radar Altimetric Performance

5.3.1. Signal to Noise Ratio

At the time this article is written the exact values of the radar system parameters and operational modes for REASON continue to evolve. For this reason we limit this section to a discussion of the link budget for nominal radar system parameters and the limits it places on usable, high-SNR cross-over altitudes. For example a radar transmitter emitting 10 W at a central frequency of 60 MHz is about 140 dB above the environmental background noise (Cecconi et al., 2012), an antenna array with 5 dB of gain will experience 10 dB round-trip gain, and a 100-microsecond pulse with 10 MHz of bandwidth will experience 30 dB of pulse compression gain. The exact realized azimuth gain will depend on the details of surface roughness at each cross-over. For rough surfaces, a nominal pulse repetition rate of 1 kHz on a spacecraft moving with 5 km/s across a 1 km Fresnel zone will experience an additional unfocused SAR azimuth gain of around 20 dB. For a very smooth (mirror-like) surface, the very narrow scattering function will prevent this azimuth gain. An ice surface will have a reflection coefficient of around -10 dB (Peters et al., 2005), but the exact geometric loss will depend on the distance R to the surface as well as the character of local surface roughness. If the surface is very flat and the spacecraft is close enough for the curvature of the moon to be neglected (<400 km) the geometric losses relate with $1/R^2$. Even for very smooth surfaces, at higher altitudes the losses approach asymptotically $1/R^4$ at about 10,000 km leading to a maximum useful altitude induced by the curvature of the moon. For rough surfaces, the maximum altitude is limited by rough-surface backscatter and geometric spreading losses. For typical Europa roughness parameters $H \approx 0.75$ and $\sigma_0 \approx 0.2$ (Compare to Section 5.3.2, Table 5.1), based on limited Galileo observations (Nimmo and Schenk, 2008), this altitude is about 200 km. Therefore, depending on the exact

roughness character of Europa's surface, cross-over altitudes available for geodetic inversion will range from 200 km (very rough surface and $1/R^4$ losses) to 5000 km (perfectly smooth surface, limited by the moon-curvature). Campbell et al. (2018) investigated MARSIS data and report an increased ratio of off-nadir returns also from very rough surfaces. Thus, for our nominal case we expect the real surface characteristics to lay in between these two end members and not to scale with $1/R^4$.

5.3.2. Geometric Performance Model

The roughness of a fractal surface can be described by the Hurst exponent H, where the rms height σ_z on a profile of length x is given by

$$\sigma_z = \sigma_0 \left(\frac{x}{x_0}\right)^H, \tag{5.2}$$

with the rms height σ_0 at unity scale $x_0 = 1$ m.
The performance model used in the simulation is executed in three steps. The first step is to identify the DTM which gives the best range performance for the radar. Since there are two flybys over one spot and from each flyby we can choose potentially between a DTM from the WAC or NAC this results in four possible DTMs. However, if during one of the flybys the cross-over plate is not illuminated or the altitude is higher than specified, the DTM option is rejected. In step two we calculate the maximum area of the cross-over plate that is allowed by the DTM without violating one of the resolution requirements. The horizontal resolution is required to be higher than the width of the outermost pulse-limited footprint. The radius r_n of the n-th pulse-limited footprint of the radar is given by

$$r_n = \sqrt{\frac{nhc}{B} + \left(\frac{nc}{2B}\right)^2}, \tag{5.3}$$

when the spacecraft is at altitude h. The width w_n of the n-th pulse-limited footprint is then

$$w_n = r_n - r_{n-1}. \tag{5.4}$$

The other cell dimension is given by the size of a Doppler bin

$$d = \sqrt{0.5\lambda h}, \tag{5.5}$$

with λ being the signal wavelength, i.e. 5 m. The area of a delay/Doppler cell inside the n-th pulse-limited footprint is then $A = w_n \times d$. Since d is usually not the limiting factor, we have to choose n such that w_n remains larger than the horizontal resolution of the DTM. It should be noted that this is not a limit on whether a DTM can be used, but rather on how much of the DTM can be used for the cross-over plate. Further, we require that the vertical resolution of the DTM exceeds twice the inherent range resolution of the radar which is given as $c/(2B)$, so that the ranging error introduced by the DTM at the mid-point of a delay/Doppler cell is less than or equal to that from the range resolution of a single radar pulse. The maximum area is then limited either by one of the two requirements above or by the maximum size of the DTM.
Concerning the surface roughness, the altimetric performance is mainly dependent on the large scale roughness expressed by the Hurst exponent (H) rather than by the small scale roughness expressed by the roughness at unity scale (σ_0). Therefore, Europa being rough at small scales (order of meters), but rather flat at larger scales (order of kilometers) turns out to be an advantage for a radar altimeter. This surface morphology is also expressed by the results of Nimmo and Schenk (2008) (Table 5.1) showing big differences in the roughness distribution at 1 m level (between 0.2 and 1.5), but showing a quite uniform distribution at larger scales ($0.5 < H < 0.8$).
The roughness further dictates together with the solar incidence angle i the shadowed fraction of the surface. Shepard and Campbell (1998) studied the shadowing behavior of fractal surfaces. Their parametrization for the non-shadowed fraction of the surface S is given by

$$S(i, \sigma_0, H) = 1 - \frac{1}{2}\sum_{n=1}^{\infty} \frac{1}{2.3^{n-1}} \times \operatorname{erfc}\left(\frac{n^{1-H}}{\sqrt{2}\tan(i)\tan(\sigma_0)}\right). \tag{5.6}$$

For each cross-over point, we evaluated equation 5.6 up to $n = 6$ as recommended by Shepard and Campbell (1998). We assume that a delay/Doppler cell is removed if less than 50% of the respective area in the DTM is illuminated. We therefore multiply the shadowed area by a factor of 2, accounting for the fact that more area has to be removed than actually shadowed. The amount of delay/Doppler cells is then decreased by the respective fraction.
In the limiting case of an extremely rough surface, for which geometric spreading losses are proportional to $1/R^4$, the maximum number of usable cells is also SNR dependent for altitudes below 200 km. To account for this we use the radar equation for a scattering surface computing the received power as

$$P_r = \frac{P_t G^2 \lambda^2 \sigma_l A \cos^4(\phi)}{(4\pi)^3 R^4}. \tag{5.7}$$

Data set	RMS dev. 100 m	RMS dev. 1 m	Hurst exponent
e86-32_Z	7.7	0.21	0.78
ediss_Z	8.5	0.27	0.75
eplains_Z	7.1	0.22	0.75
erhad_Z	5.6	0.2	0.72
etyre-3_Z	15.9	1.5	0.51
manan-80_Z	14.9	1.2	0.55

Table 5.1: RMS deviations for different data sets at different scale lengths as derived from Nimmo and Schenk (2008). The last column has been added to express the results in terms of Hurst exponents.

In Equation 5.7 P_t is the transmitted power of 10 W, G is the one-way gain, λ is the radar wavelength and σ_l are the backscatter losses due to the surface roughness at normal incidence. The latter is assumed to be -15 dB. Further, R is the distance from the spacecraft to the respective cell, A is the area of that cell and ϕ expresses the off-nadir angle to the cell such that the $\cos^4\phi$ term accounts for the backscatter falloff from the nadir value. We only consider cells where the area is large enough to reach the SNR threshold of 1.

5.3.3. Point Target Simulator

For a more in-depth analysis of the proposed concept and the validation of the model described above a point target simulator is used to simulate raw radar echoes from a surface DTM. The DTM we used for this purpose is the *Ediss* region from Nimmo and Schenk (2008) (compare to Table 5.1). The DTM is tiled to create a larger DTM long enough, for the radar track. The DTM is faceted and evenly sampled in latitude and longitude at half the range resolution of the radar. Each facet is given a random scattering phase that is constant for all sensor positions. The radar equation is then used to sum up the range compressed point target response of each facet for each sensor position. To evaluate the altimetric precision, we first simulate a truth echo set from the DTM. This represents the 'measured' data. We then simulate echoes from a DTM with different sets of systematic errors. Each DTM is given a new set of random phases for the point targets, and Gaussian noise is added with a signal to noise ratio of 24 dB, which corresponds to REASON assuming $1/R^4$ geometric spreading, -10 dB surface backscatter cross section, 100 km altitude, and 30 dB range compression gain. Using an azimuth window with the size of the number of looks, we find the peak of the range correlation between the 'measured' echoes and the error DTM to determine the altimetric range. The window is then stepped and we gather 7000 estimates of the range from which the precision is determined from the standard deviation of the altimetric estimates for a given number of looks. The point-target simulator did not take advantage of the Doppler information in the signal and is therefore a conservative lower bound. The results are shown in figure 5.2 together with the range measurement errors as estimated by the geometric performance model described in section 5.3.2. The result is shown as a function of looks and evaluated for all cross-over points in the 17F12 v2 trajectory developed by the Europa mission project. While the point target simulator does not make any assumptions about the altitude nor viewing conditions, the geometric performance model is sensitive to these parameters and therefore may give different results for the same amount of looks. Further, we investigated the results assuming different systematic errors inside the DTM. We applied cross track shifts, rotations and tilts with different values. These errors are generic and might account for different sources by covering the degrees of freedom that can affect a DTM in its entirety. Rotation is about a surface normal vector at the midpoint of the track. A tilt is a cross track rotation about the ground track. From figure 5.2 we can infer that a rotation is the least critical distortion since it only slightly shifts the beam pattern gain without a significant net change in the range determination. However, significant error contributions are expected if the DTM is tilted in the order of 1° or higher or if a systematic cross track bias is present. To successfully measure the range with high accuracy it is therefore crucial to have high quality DTMs making them an important driver for the range accuracy.

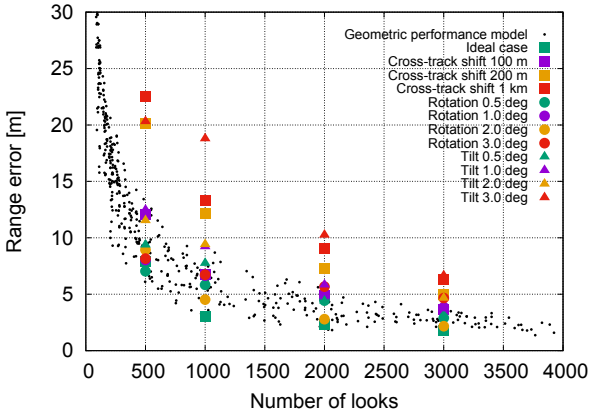

Figure 5.2: Estimated range errors as a function of looks. The coloured symbols represent the results from the point target raw simulator. In comparison the results from the geometric performance model at all cross-over locations covered by the WAC are shown. The "jitter" is a consequence of cross-overs with two different altitudes, which can contribute to one range measurement while still having a similar amount of looks.

5.3.4. Influence of the Ionosphere

Europa possesses a complex plasma environment. The ionosphere is fed by multiple sources (Kivelson et al., 2009) but dominated by two main processes: photo- and particle-impact ionization (McGrath et al., 2009). The first effect is strongest at the solar illuminated hemisphere, while particle impacts are correlated to the rotation of the Jupiter magnetosphere and focused on the trailing hemisphere of the moon. The variability of Jupiter's magnetosphere can further lead to a time dependence of the ionospheric conditions. Since the propagation of radio waves through an electrically charged medium can disturb the signal, the effect must be discussed for the here proposed measurement. The radar signal propagation through the ionosphere of Europa has been studied previously by Grima et al. (2015b). The authors examined two frequency dependent effects as a function of altitude. The first one being an alteration of the inherent range resolution due to a pulse spreading around the center frequency and the second one an induced time delay. The inherent resolution degrades from the original 15 m to down to 25 m when ranging at altitudes > 1000 km (Grima et al. (2015b), figure 5). The two-way time delay at the central frequency of 60 MHz is expected to range between 10^{-8} seconds at low altitudes and up to 3×10^{-7} seconds at 1000 km and higher corresponding to an one-way range error of 1.5 to 45 m if remaining unconsidered. While the authors conclude that the ionosphere does not significantly impact the sounding aspect it does matter for the altimetry. However, there are possible strategies to mitigate this effect. The vertical time resolution of a radar sounder is theoretically the best uncertainty a correction technique could achieve for inverting the ionospheric delay. This value is explicitly stated for the correction of the REASON HF signal (Grima et al., 2015b) and implicitly assumed for MARSIS's (Mouginot et al., 2008). However, both do not use autofocused techniques, but rather rely on a third-party signal undisturbed by the ionosphere to estimate what the traveling time of the signal should be. The effect of the ionosphere leads to a relative difference of delay ΔT between the higher and the lower frequencies in the bandwidth B around the center frequency f. This chirp broadening is directly related to the global signal delay δt and has been expressed by Grima et al. (2015b) as

$$\Delta T = |\delta t(f - B/2) - \delta t(f + B/2)| \,. \qquad (5.8)$$

The parentheses in the formula should be read as δt where the frequency is (f-B/2) and (f+B/2). To restore the pulse one can make use of the general compressed SNR loss that occurs due to the pulse spreading. However, the SNR loss can be regained by adapting the matched filter using the same broadening. By maximizing the compressed SNR the pulse spread and therefore also the pulse delay can be restored. In reality this pulse reconstruction is a function of (uncompressed) SNR. To further investigate this issue we performed numerical simulations using a 30 μs radar chirp at $f = 60$MHz and an artificially induced delay of $\delta t = 100$ ns. For uncompressed SNR's between 1 and 20 we then swept through different filters with broadening and found that for any SNR > 1 the delay can be constrained better than 10 ns.
Sanchez-Cano et al. (2015) compared the performance of both approaches, autofocused and reference-based corrections. Although some biases were found under thick-ionosphere conditions, no difference in the time delay estimation was reported for a weak ionosphere distortion as expected at Europa at VHF frequencies. For the following analysis we assume that the ionospheric delay can be corrected, but that a residual of 20% of the initial delay difference between the two flyby altitudes will remain.

5.4. Tidal Inversion

In regard of the uncertainties treated in the section above, the strategy for the tidal inversion is to investigate five possible cases. Scenario 1 is the best case scenario for SNR and uses cross-over points up to 4000 km altitude with the full delay/Doppler information. Scenario 2 considers the nominal operation scenario up to 1000 km altitude. Scenario 3 studies the case of severe biases in the DTM used for the cross correlation. Scenario 4 assumes a flat surface and therefore no available azimuth information limiting the range accuracy to 15 m. Finally, Scenario 5 assumes a very rough surface where the SNR limits the maximum altitude to 200 km.

In our a priori cross-over search we considered all

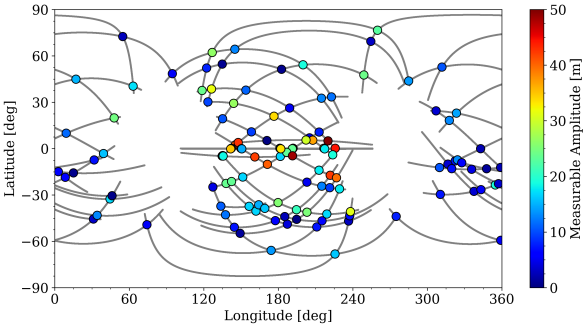

Figure 5.3: Cross-over locations of the 17F12v2 trajectory up to an altitude of 1000 km. The color indicates the measurable tidal amplitude at the respective cross over point assuming a tidal Love number h_2 of 1.2.

points below a spacecraft altitude of 4000 km ending up with a total of 303 cross-over points. Scenario 1 only appears feasible however, in case of favorable surface roughness conditions and is therefore considered as the most optimistic case. Given the observational evidence from the surfaces of Europa it can nonetheless not be ruled out that such surfaces exit. In this scenario the vertical range resolution of the WAC limits the use to a maximum altitude of around 1000 km, while the vertical resolution of the NAC is sufficient in order to be used up to a maximum altitude of around 2000 km. The nominal operation scenario for REASON includes continuous operation at altitudes below 1000 km, an altitude that would be compliant with WAC coverage only. Therefore, Scenario 2 will define our nominal case including 124 cross-over points (figure 5.3). In this scenario we assume that the SNR budget is dominated by $1/R^2$ losses; that the ionospheric delay can be corrected to better than 20%; and that the additional range error, due to systematic DTM errors is less than 2 m. For most cross-over plates this implies tilts and rotations to be limited to 0.5° and a correct cross-track georeferencing with around 100 m accuracy. In case of more biased DTMs we consider Scenario 3, which differs from the latter one by having 10 m of systematic errors from the DTMs included. Such errors can occur if the cross-track location is known with less than 1 km accuracy or if the DTM is tilted or rotated by more than 3°.

We further consider two pessimistic Scenarios, 4 and 5. In Scenario 4 an unexpectedly low roughness limits the delay/Doppler approach to "one look" and therefore to the inherent range resolution of 15 m. In Scenario 5 the SNR is limited by $1/R^4$ losses due to surface roughness limiting the maximum altitude down to 200 km and further reducing the amount of delay/Doppler cells at the remaining cross-over points.

Besides of the instrument error the determination of the tidal Love number h_2 will depend on the knowledge of the orbit. We assumed that the position of the spacecraft is known at the beginning of the flyby with an accuracy of 1 km and 1 mm/s in each axis at a radial distance of 10,000 km from Europa. Using two pairs of observables, the range between spacecraft and surface at the cross-over points and synthetic Doppler velocity data sampled every 60 s with an accuracy of 0.1 mm/s, we solve for the initial position of the spacecraft at each flyby as well as for h_2 using an iterative least squares algorithm. The parameter vector therefore consists of 277 unknowns, 46 initial state vectors each consisting of 6 parameters and h_2 ($6 \times 46 + 1$). The range measurement errors of the radar are applied to each cross-over point according to the described performance model assuming a surface roughness given by $\sigma_0 = 0.6$ and $H = 0.6$. If this analytical range error exceeds the inherent range resolution the cross-over is removed from the inversion. Otherwise the analytical error is used to generate a random error using a Gaussian generator with the analytical value as 1-sigma input. For each scenario the simulation has been repeated 20 times. The results for the different scenarios are given in table 5.2. In case of operation up to 4000 km altitude we find that h_2 can be constrained with an absolute accuracy of 0.04. Due to the high operational altitude the ionosphere delays between the different passes can dominate the range error. However this effect is counteracted by the high amount of cross-over points leading to the best accuracy of all studied cases. The nominal

Scenario	**Comment**	**Max. altitude [km]**	Δr [m]	**Nb. of usable/total cross-over points**	h_2 **error**
1	High SNR	4000	6.7	229/303	0.04
2	Nominal case	1000	5.3	103/124	0.06
3	Biased DTMs	1000	11.2	101/124	0.17
4	No azimuth gain	1000	15	124/124	0.11
5	SNR with $1/R^4$ losses	200	3.8	39/44	0.13

Table 5.2: Results of the inversion for the different scenarios studied. The h_2 error estimates and range error values Δr have been averaged over 20 runs.

case with operation up to 1000 km leads to an estimated h_2 accuracy of 0.06 with an average range error of around 6 m. This accuracy is significantly degraded in case of the DTMs being affected by large systematic errors. The lower range measurement accuracy of about 11 m does not only directly affect the h_2 measurement but further degrades the orbit determination which has a feedback on the tidal measurement. The resulting h_2 estimate in this case is assessed to be 0.17. The last two cases are studying the two end members of possible SNR behavior. In case of a flat (mirror-like) surface the range error would be limited to the inherent range resolution of 15 m. However, in this case DTM constraints no longer apply, therefore more cross-over points are available for the geodetic inversion. Thus, while having even higher range errors as in case 3, the overall h_2 accuracy would still be slightly better with an absolute value of 0.11. In the other case of a very rough surface and a maximum operational altitude for altimetry of about 200 km the high amount of delay/Doppler cells in combination with the low ionospheric distortions lead to the best range error of less than 4 m. However, only 44 cross-over points remain for the evaluation. This leads to an estimated h_2 error of 0.13.

5.5. Implications for Europa's Interior

In order to deduce the resulting ice thickness we must consider that the tidal Love numbers k_2 and h_2 further depend on the deep interior of Europa as well as on the rheology of the outer ice layer. We assumed a general structural model for Europa with four layers which are an iron core, a silicate mantle, an ocean and an ice-I layer. Then we calculated a wide number of possible interior structure models all in agreement with Europa's total mass and mean moment of inertia as measured by the Galileo mission (Anderson et al., 1998). The parameter ranges and step sizes for the radii as well as densities of the respective layers are given in table 5.3. The models have been solved for the core radius and the mantle density while the other parameters have been dynamically varied. For the resulting structural models the tidal Love numbers h_2 and k_2 have been computed using a numerical integration of the linearized field equations (Segatz et al., 1988) for the simplified assumptions of a fully elastic outer ice shell and an ice-I rigidity of 3.3 GPa (Sotin et al., 1998). The relation between ice thickness and h_2 are plotted in figure 5.4. Typical values for h_2 are around 1.2 in the presence of an ocean and drop below 0.1 if no ocean is present. Using the estimated error bounds for h_2 alone this would allow to unambiguously confirm or reject the hypothesis of a global ocean also in a reasonably unfavorable scenario with high orbit errors, low SNR and less accurate DTMs. But no further conclusion on the ice thickness could be drawn. The most promising approach to constrain the ice thickness, is to use the linear combination $\Delta = 1 + k_2 - h_2$ (Wahr et al., 2006). This reduces the ambiguity significantly, especially for thin ice shells as shown in figure 5.4. As for h_2 the exact error of k_2 will depend on the final scenario, but usually the k_2 error is equal or below the h_2 error (Mazarico et al., 2015; Steinbrügge et al., 2015; Parisi et al., 2014). Assuming an error in k_2 in the same order of magnitude and 4% in h_2 according to the optimistic case of the analysis presented above, we infer that the ice thickness can be constrained with an accuracy of about $\pm$15 km, when assuming the rheology to be known.

5.6. Discussion

The proposed method using the radar returns in combination with stereo DTMs from a camera system can be compared to surface clutter removal

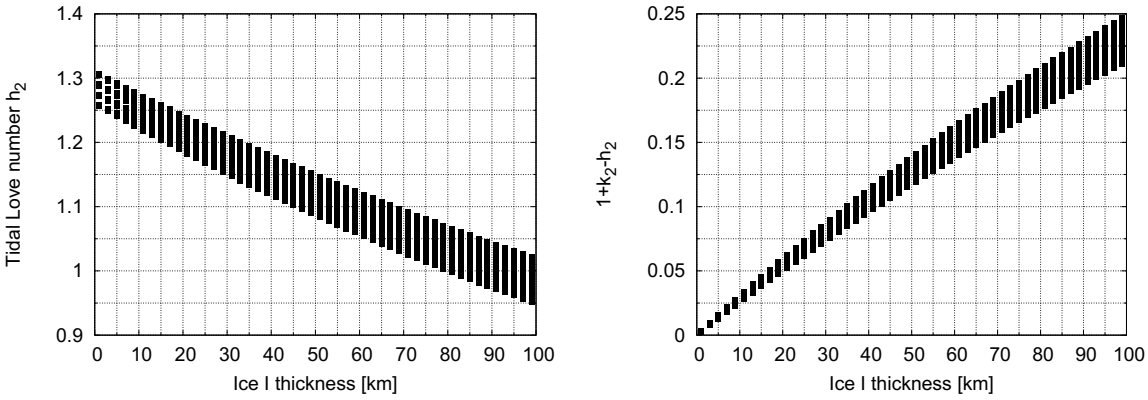

Figure 5.4: Left: Tidal Love number h_2 as a function of ice thickness. Right: Linear combination $1+k_2$-h_2. Each point represents a structural model in agreement with the total mass and mean moment of inertia.

Layer	$d_{\min}$	$d_{\max}$	Δd	$\rho_{\min}$	$\rho_{\max}$	$\Delta\rho$
Core	200	500	-	4000	7000	500
Mantle	500	1200	100	2400	3800	-
Ocean	10	200	10	1000	1200	50
Ice	1	100	10	900	1100	20

Table 5.3: Boundaries and step sizes for the used parameters of Europa. The thickness d [km] and density ρ [kg/m^3] of each individual layer has been varied between a min and a max value with a stepsize Δ. The models have been solved assuming a gravitational parameter of $GM = 3202.72 \times 10^9$ km^3/s^2 and a mean moment of inertia of 0.346 (Schubert et al., 2004).

techniques successfully applied to the Mars polar caps with ShaRad and MOLA DTMs (Ferro and Bruzzone, 2013). This application was able to get similar results for the co-registration of both data sets vertically as well as in azimuth. The authors report comparable numbers of (5 ± 2)m in range and (4 ± 3)m in azimuth. However, certain assumptions have been made in our study one needs to be aware of. We do not account for subsurface returns since we assume that any volume scattering return will be undetectable compared to the dominant return from the ice/void interface in nearly every case (Aglyamov et al., 2017) and that the cross-correlation method will not be significantly affected also in presence of echoes from coherently reflecting near-nadir subsurface interfaces. Also, we do not account for different surface materials or dielectric properties since the even in the presence of heterogeneous surface material, the ice/void interface will produce the dominant return. The ranging errors calculated by the point target simulator can be nonetheless considered as conservative since they do not fully exploit the delay/Doppler information. And not all capabilities of REASON have been explored in the frame of this work. Additional improvements in performance could come from combining data of the HF and VHF bands or exploiting the cross-track interferometric capability of the VHF band. For the tidal inversion we do not consider uncertainties in the rotational state of the body. This approach is considered to be justified by the idea that the location of the DTM in a body-fixed coordinate system is not needed to be known with high accuracy when inverting for the response to a degree two potential. Finally, we assume that all cross-over points are known a priori. Changes in the planned trajectory, which imply changes of the cross-over locations might need to be recovered by taking additional stereo images in a later phase of the mission.

An estimated accuracy of 0.04 and the resulting ice shell constraint of $\pm$15 km would generally be meaningful for larger ice thicknesses (>20 km), however it would clearly loose its significance for thin shells. Therefore, the altimetry capabilities can be seen as complementary to the direct sounding approach where in case of a thin ice shell ($<$ 15 km) the radar would be able to detect the ice-ocean boundary directly. A higher accuracy is unlikely to be achieved by altimetric radar measurements alone without mission extension or changes in the instrument bandwidth. However, such ranging accuracy could be achieved by laser altimetry.

The highest ambiguity in the ice shell thickness comes from the unknown rigidity and viscosity of the ice. In order to find a unique solution, a combination of complementary instrument data products

(magnetometer, camera, radar, radio science) will be needed. A potential strategy to constrain the viscosity could in principle also consist in the determination of a tidal phase-lag or by measuring the horizontal displacement expressed by the tidal Love number l_2 since also a horizontal co-registration of the radar returns with the DTM is feasible (Ferro and Bruzzone, 2013). Assessing the potential for these measurements will be part of future work.

5.7. Conclusion

The potential for the REASON instrument to perform altimetric measurements during NASA's Europa Clipper mission has been assessed and a simulation using the planned trajectory has been performed. In order to measure the tidal Love number h_2 detailed DTMs from Europa's surface are required. The performance of these measurements has been evaluated and several possible influences on the h_2 measurement accuracy have been discussed. Exploiting the delay and Doppler information we found that ranging accuracies of 3-8 m on average across all cross-over points are achievable. Possible additional error sources might be systematic errors in the DTM leading to range errors of up to 11 m. However, the dominating error source are orbit errors in case no full radio coverage is available. The entirety of these constraints lead to an estimated error in h_2 between 0.04 and 0.17. All cases would allow us to confirm the presence of a subsurface ocean, the optimistic case could constrain the thickness of Europa's outer ice shell to $\pm$ 15 km independently of the deep interior structure. The biggest uncertainty under these conditions would result from the unknown ice rheology. Possible strategies to further reduce this ambiguity could come from additional altimetry observations like planetary phase lags or by a combination of data from complementary instruments onboard the Europa Clipper.

Acknowledgments

We thank Ryan Park and Francis Nimmo for providing data sets supporting this work and providing helpful comments. We thank Alexander Stark, Klaus Gwinner and Ashok Verma for helpful discussions and two anonymous reviewers for a constructive review which helped significantly to improve this contribution. A portion of this work was carried out by the Jet Propulsion Laboratory, California Institute of Technology, under a contract with NASA.

References

Aglyamov, Y., Schroeder, D.M., Vance, S.D.. Bright prospects for radar detection of Europa's ocean. Icarus 2017;281(Supplement C):334 – 337. doi:doi.org/10.1016/j.icarus.2016.08.014.

Anderson, J., Schubert, G., Jacobson, R., Lau, E., Moore, W., Sjogren, W.. Europa's differentiated internal structure: Inferences from four Galileo encounters. Science 1998;281(5385):2019–2022.

Blankenship, D., Young, D., Moore, W., Moore, J.. Eruopa; The University of Arizona Press.

Campbell, B.A., Schroeder, D.M., Whitten, J.L.. Mars radar clutter and surface roughness characteristics from MARSIS data. Icarus 2018;299:22 – 30. doi:10.1016/j.icarus.2017.07.011.

Cecconi, B., Hess, S., Herique, A., Santovito, M., Santos-Costa, D., Zarka, P., Alberti, G., Blankenship, D., Bougeret, J.L., Bruzzone, L., Kofman, W.. Natural radio emission of Jupiter as interferences for radar investigations of the icy satellites of Jupiter. Planetary and Space Science 2012;61(1):32 – 45. doi:10.1016/j.pss.2011.06.012.

Ferro, A., Bruzzone, L.. Automatic Extraction and Analysis of Ice Layering in Radar Sounder Data. IEEE Transactions on Geoscience and Remote Sensing 2013;51(3):1622–1634. doi:10.1109/TGRS.2012.2206078.

Garcia, E., Sandwell, S., Smith, W.. Retracking CryoSat-2, Envisat and Jason-1 radar altimetry waveforms for improved gravity field recovery. Geophysical Journal International 2014;196:1402–1422. doi:10.1093/gji/ggt469.

Grima, C., Blankenship, D., Schroeder, D.. Radar signal propagation through the ionosphere of Europa. Planetary and Space Science 2015;117:421–428.

Kivelson, M., Kuhrana, K., Volwerk, M.. Eruopa; The University of Arizona Press.

Mazarico, E., Barker, M., Neumann, G., Zuber, M., Smith, D.. Detection of the lunar body tide by the Lunar Orbiter Laser Al-

timeter. Geophysical Research Letters 2014;41. doi:10.1002/2013GL059085.

Mazarico, E., Genova, A., Neumann, G., Smith, D., Zuber, M.. Simulated recovery of Europa's global shape and tidal Love numbers from altimetry and radio tracking during a dedicated flyby tour. Geophysical Research Letters 2015;42. doi:10.1002/2015GL063224.

McGrath, M., Hansen, C., Hendrix, A.. Eruopa; The University of Arizona Press.

Mouginot, J., Kofman, W., Safaeinili, A., Herique, A.. Correction of the ionospheric distortion on the MARSIS surface sounding echoes. Planetary and Space Science 2008;56(7):917 – 926. doi:10.1016/j.pss.2008.01.010.

Moussessian, A., Blankenship, D., Plaut, J., Patterson, W., Gim, Y., Schroeder, D.. REASON for Europa. AGU Fall Meeting 2015;.

Nimmo, F., Schenk, P.. Stereo and photoclinometric comparisons and topographic roughness of Europa. Lunar and Planetary Science 2008;XXXIX.

Pappalardo, R., Senske, D., Prockter, L., Paczkowski, B., Vance, S., Rhoden, A., Goldstein, B., Magner, T., Cooke, B.. Science Objectives for the Europa Clipper Mission. Concept: Investigating the Potential Habitability of Europa. EPSC 2015 2015;10.

Parisi, M., Iess, L., Finocchiaro, S.. The gravity fields of Ganymede, Callisto and Europa: how well can JUICE do? Geophysical Research Abstracts 2014;EGU2014:11758.

Peters, M.E., Blankenship, D.D., Morse, D.L.. Analysis techniques for coherent airborne radar sounding: Application to West Antarctic ice streams. Journal of Geophysical Research: Solid Earth 2005;110(B6):n/a–n/a. doi:10.1029/2004JB003222; b06303.

Raney, R.. The Delay/Doppler Radar Altimeter. IEEE Transactions on Geoscience and Remote Sensing 1998;36:1578–1588.

Raney, R.. CryoSat SAR-Mode Looks Revisitedr. IEEE Transactions on Geoscience and Remote Sensing 2012;9:393–397.

Schubert, G., Anderson, J., Spohn, T., McKinnon, W.. Jupiter. The Planet, Satellites and Magnetosphere; Cambridge University Press. p. 281–306.

Segatz, M., Spohn, T., Ross, M., Schubert, G.. Tidal dissipation, surface heat flow, and figure of viscoelastic models of Io. Icarus 1988;75:187–206. doi:10.1016/0019-1035(88)90001-2.

Shepard, M.K., Campbell, B.A.. Shadows on a Planetary Surface and Implications for Photometric Roughness. Icarus 1998;134(2):279 – 291. doi:10.1006/icar.1998.5958.

Sanchez-Cano, B., Morgan, D.D., Witasse, O., Radicella, S.M., Herraiz, M., Orosei, R., Cartacci, M., Cicchetti, A., Noschese, R., Kofman, W., Grima, C., Mouginot, J., Gurnett, D.A., Lester, M., Blelly, P.L., Opgenoorth, H., Quinsac, G.. Total electron content in the Martian atmosphere: A critical assessment of the Mars Express MARSIS data sets. Journal of Geophysical Research: Space Physics 2015;120(3):2166–2182. doi:10.1002/2014JA020630.

Sotin, C., Grasset, O., Beauchesne, S.. Solar system ices; Springer Netherlands. p. 79–96. doi:10.1007/978-94-011-5252-5-4.

Steinbrügge, G., Stark, A., Hussmann, H., Sohl, F., Oberst, A.. Measuring tidal deformations by laser altimetry. A performance model for the Ganymede Laser Altimeter. Planetary and Space Science 2015;doi:10.1016/j.pss.2015.06.013.

Turtle, E., McEwen, A., Collins, G., Fletcher, L., Hansen, C., Hayes, A., Hurford, T., Kirk R.L.and Barr Mlinar, A., Nimmo, F., Patterson, G., Quick, L., Soderblom, J., Thomas, N., Ernst, C.. The Eorpa Imaging System (EIS): High-esolution Imaging And Topogrpahy to Investigate Europa's Geology, Ice Shell, and Potential for Current Activity. 47th Lunar and Planetary Science Conference 2016;.

Wahr, J., Zuber, M., Smith, D., Luine, J.. Tides on Europa, and the thickness of Europa's icy shell. Journal of Geophysical Research 2006;111:E12005. doi:10.1029/2006JE002729.

Wu, X., Bar-Sever, Y.E., Folkner, W.M., Williams, J.G., Zumberge, J.F.. Probing Europa's hidden ocean from tidal effects on orbital dynamics. Geophysical Research Letters 2001;28(11):2245–2248. doi:10.1029/2000GL012814.

Chapter 6

Discussion

This thesis has been written in the context of the three projects BELA, GALA and REASON, and in interaction with the engineering and science teams involved in the instrument development and mission design. The availability of reliable performance models allows to assess the impact of various design choices and to search for trade-offs. The models further allow to specify and to verify requirements from top-level science requirements down to technical requirements on instrument level. Therefore, they are a valuable tool assuring the consistency and traceability of the requirement flow. The models also contribute to the instrument operation planning and provide a possibility to quantitatively analyze new tour designs.
The application of the models to the different missions further allows a comparative view and therefore to use synergies on the one hand and to recognize commonalities on the other hand, providing a deeper understanding of the driving factors of the tidal measurement. The key characteristics of all three studied cases are summarized in Table 6.1. It has been outlined in Paper I, Paper III, and Paper IV that

	Mercury (BELA)	**Ganymede (GALA)**	**Europa (REASON)**
Max. tidal double-amplitude	2 m	7 m	60 m
Operation time for tidal measurement	1 – 2 years orbit	132 days orbit	46 flybys
Cross-over points	60 million	1 million	126
Cross-over range error budget	12.5 m	6.4 m	3 – 15 m
Estimated h_2 accuracy	0.14	0.026	0.05 – 0.17

Table 6.1: Comparison of the estimated measurement results of the three instruments studied in this thesis.

the success of a tidal measurement always depends on three main components. Namely, the spacecraft trajectory and mission duration, the instrument performance, and the strength of the tidal signal.
In view of the three studied cases, Europa, Ganymede, and Mercury, it is therefore plausible why the prediction given in Paper I for the determination of h_2 by BELA during the nominal mission lifetime are so modest. With very small tidal deformations, Mercury is already a challenging target for the h_2 measurement. In combination with Mercury's high surface roughness at the relevant baselines this leads to significant interpolation and pointing errors when using the cross-over approach at a shot frequency of 10 Hz. It also shows that for GALA, the 30 Hz pulse repetition frequency is a very important design choice, since also for Ganymede rough terrain can be expected. The second aspect is the orbit of the MPO which has an inclination close to 90°. Together with the slow rotation rate of Mercury, the orbit leads to few cross-over points at equatorial latitudes lower than 60° N or above -60° S. The combination of low expected amplitudes, Mercury's slow rotation rate, and high cross-over error budget makes the h_2 measurement very challenging.
For BELA however, it should be noted that the h_2 measurement is not among the primary science goals, other than in the case of GALA. Based on the results of Paper II, I nonetheless suggest to reconsider the available options to eventually achieve the measurement with a better accuracy than predicted by Paper I. The determination of the inner core size of Mercury would be a valuable science goal beyond the achievements of the MESSENGER mission. Therefore, the accuracy would have to be in the order of few percent instead of the currently estimated 18%, which would not allow for any constraints on

the inner core radius. A possible option would be - naturally - a mission extension since this leads to more cross-over points at lower latitudes. An improvement in shorter time could also be achieved with a slightly lower orbit inclination (e.g., 80-85°) of the Mercury Planetary Orbiter, coming at the cost of a small gap at the poles. But also alternative methods for the tidal inversion might be successful. Due to the unfavorable distribution of cross-over points another option would be e.g., the method suggested by Koch et al. (2008, 2010) inferring the time variations of the topography expressed in spherical harmonics. The method has the advantage to exploit the complete data set and is currently investigated by Thor et al. (2017). But also the co-registration of laser tracks with themselves might be suitable (Stark et al., 2017b). However, other than cross-over measurements, these techniques are less established and will require further work.

For GALA, the presented performance model is currently the reference model used to validate all changes of the design parameters and intended to incorporate all upcoming test results. It should be noted however, that Paper III appeared before Paper I and therefore does not rely on the updated model but on the original version published by Gunderson et al. (2006); Gunderson and Thomas (2010). The results for the instrument performance in Paper III can therefore be considered as conservative from the modeling point of view since the Gunderson model uses a Cramer-Rao limit for the estimation of the range error, representing an upper boundary. The actually observed range errors during the end-to-end test campaign of BELA are well below the errors predicted by the Gunderson model. This is also because the filter matching algorithm of the range finding module (RFM) is not well represented by the analytical formulation in Gunderson and Thomas (2010). Test results show indeed that the RFM algorithm is more efficient than has been previously predicted. This finding is consistent with previous tests of BELA's RFM (Beck, 2012). Another element why the results of Paper III can be considered to be conservative is that the mean eccentricity of Ganymede (0.0015) has been taken to calculate the tidal potential. However, Ganymede's eccentricity is highly time-variant and changes from values close to zero up to eccentricities of ≈ 0.003 within 50 years (Figure 6.1). Fortunately, if the JUICE mission follows the current schedule, at the arrival time at Ganymede, the eccentricity will be close to its maximum. This leads to significantly higher amplitudes than estimated in Paper III, i.e. up to 14 m instead of 7 m double amplitudes. Also, during the mission lifetime the eccentricity cannot be considered constant when inverting for h_2. This is an effect which has been neglected in Paper III. A more precise description can be obtained by replacing the mean eccentricity e by a time dependent eccentricity function $e(t)$ when calculating the tidal potential. With consideration of the time varying eccentricity of Ganymede the h_2 measurement accuracy by GALA is below 0.02. The heavily time dependent eccentricity offers further interesting perspectives for the far future. Since these changes in eccentricity are periodic it is in principle possible to measure the reaction of Ganymede to tidal forcing at different frequencies. These second order effects should be in the order of centimeters and are therefore extremely difficult to measure. If done so however, they would provide a frequency spectra of the ice shell reaction, allowing a far better constraint on the rheological properties of the ice.

Previous studies emphasized that h_2 is not only a function of the ice-shell thickness but also of the rheological properties, i.e. of the rigidity and viscosity of the ice I layer (e.g., Wahr et al. (2006)). Therefore, the determination of the ice-shell thickness is still ambiguous. To reduce this ambiguity a determination of the tidal phase-lag would be very useful since it helps to constrain the Maxwell time. The dependency between the ice-shell thickness and h_2 can be subdivided into three major branches. In case 1, a very low viscosity of the ice shell would lead to a fluid regime, which is very unlikely in case of Ganymede. Case 2 is the viscoelastic case with viscosities between $10^{15} - 10^{17}$ Pa s. In this case a tidal phase-lag should be observable and therefore constrain the viscosity of the ice shell to the respective range. And in case 3, a mostly high viscosity ice shell, the layer would react elastically. Even if in the fully elastic case the tidal deformation still depends on the rigidity, this latter dependence can be greatly reduced by using the linear combination $1 + k_2 - h_2$ known as the *diminishing factor* (Wahr et al., 2006). Work published after Paper III did a broader investigation of possible Ganymede interior models and their dependency on tidal Love numbers. In a recent study, Kamata et al. (2016) concluded that the determination of h_2 alone is not sufficient to confirm the presence of a global subsurface ocean since models without ocean and h_2 values over 1.3 exists. Unfortunately, the authors do not provide details about the set of parameters that are required to achieve such a case. My own modeling efforts suggests

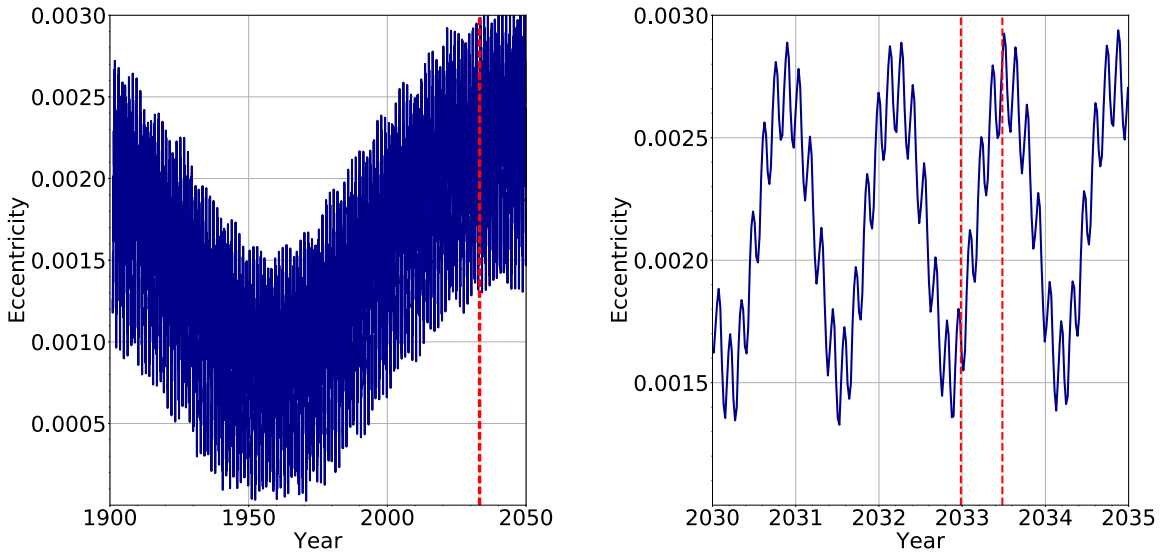

Figure 6.1: Orbital eccentricity of Ganymede averaged over one orbital period. The red dashed lines delineate the time frame of JUICE being in orbit around Ganymede. Left: Long term variations, shown here from 1900 to 2050, range between almost zero eccentricity and 0.003. Right: During the orbital phase around Ganymede, the eccentricity almost doubles from 0.0015 to 0.003.

that a very low viscosity high pressure ice layer ($< 10^{13}$ Pa s) is needed in order to get the corresponding radial tides. The high-pressure ice layer then acts as a quasi-ocean being close to the fluid regime. While such a case cannot be excluded, I consider it rather unlikely to have an extended low viscosity, high pressure ice layer in combination with a cold ice I layer and no ocean in between. An option to test this case would be the previously mentioned observation of the tidal phase-lags of k_2 and h_2. The difference in phase-lags is a proxy for the dissipation in the HP ice layer as has been shown in Hussmann et al. (2016).

In the case of Europa, a high tidal Love number h_2 (>1) is an ultimate evidence for a global subsurface ocean. The advantage in this case is the high tidal amplitude. The peak-to-peak height deviation is in case of a global liquid layer in the order of 60 m at the equator. This sets the requirement on the measurement accuracy and amount of cross-over points to a lower value than for Ganymede or even Mercury. Even if the flyby trajectory does not provide as many cross-over points as would be available with an orbiter, it does contain about 20 very valuable profile crossings with significant amplitudes. Therefore, the measurement of a tidal signal of Europa can be expected. However, in absence of a laser altimeter and given that the mission is conceived as a flyby missions, other challenges arise. Aside from the actual measurement principle discussed in Paper IV, the main issue is the contribution of orbit determination errors. Any altimetric instrument only measures the range from spacecraft to the surface. This information is worthless for the tidal deformation measurement without information about the spacecraft location. While BepiColombo and JUICE are equipped with very powerful radio science experiments (MORE and 3GM, e.g., Iess and Boscagli (2001); Iess (2013); Imperi et al. (2018)), the Clipper mission has only limited radio tracking abilities. This means that only one 20 W X-band radio transmitter is available in combination with three fan beam antennas. Verma and Margot (2018) investigated the radio science capabilities of the Europa Clipper. They considered different NASA Deep Space Network (DSN) configurations starting with one 34 m antenna to 3×34 m antennas complemented by a 70 m antenna for selected flybys. They came to the conclusion that tracking of all flybys might be possible when incorporating the 70 m antenna. This case would lead to orbit covariance errors favorable for the h_2 determination. If only e.g., a 2×34 m antenna configuration is available, not all flybys would be tracked and the amount of cross-over points available for the inversion could be reduced from 126 to 68. Orbit

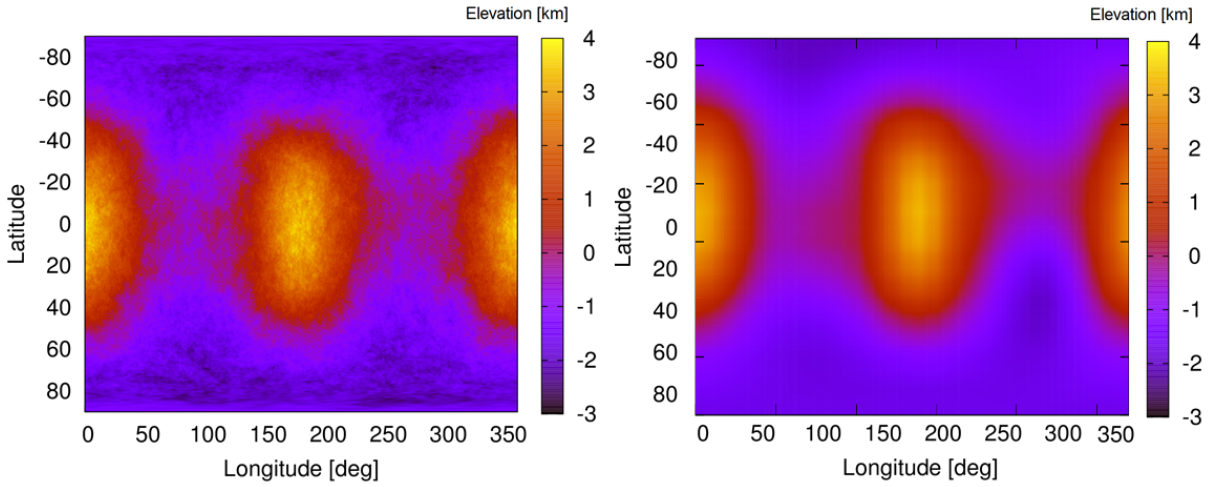

Figure 6.2: Left: Synthetic global shape model of Europa provided by Francis Nimmo (personal communication). Right: Inferred shape model based on synthetic REASON radar tracks modeled based on the methods presented in Paper IV.

uncertainties are therefore in the case of the Europa Clipper the dominant error source.
Aside from the tidal measurement the proposed technique for altimetric radar measurements has also the potential to perform other geodetic measurements like the global shape of Europa. This is usually difficult to provide from stereo images and therefore benefits from an altimeter. I performed additional analysis using the full ground tracks for shape reconstruction. The result with the synthetic shape of Europa compared to the inferred shape are depicted in Figure 6.2. The analysis suggests that Europa's global shape can be inferred up to degree and order six in spherical harmonics. The accuracy of the C_{20} and C_{22} shape coefficients are between 2 and 3%. Another aspect of Europa with its thin ice shell and dynamic geologic environment is that the assumption of a spherical ice shell might be oversimplified. For instance, ocean-driven heating of Europa's icy shell at low latitudes (Soderlund et al., 2014) can have an impact on the shell thickness and therefore also on the tidal deformation pattern. Therefore, future work should address the possibility of non-spherical ice shells and assess the impact on different models on tides. Other geodetic measurements, like librations and obliquity, have to be further investigated as well.

However, like all models also the ones presented in this dissertation are only valid under the given assumptions and constitute in many aspects a simplification. These will be discussed in this section in a broader context. For a detailed discussion of the methods applied, I refer to the discussion section of the respective publication.
An important step towards a reliable instrument performance model was the first availability of BELA test data which indeed indicated that the analytical description by Gunderson et al. (2006); Gunderson and Thomas (2010) was not well representing the actual instrument performance. This lead to the development of the refined model presented in Paper I. The test data which has been acquired with the BELA flight model integrated on the BepiColombo spacecraft can be considered as the most representative data for model validation in terms of hardware. Nonetheless, under these environmental conditions no optical return pulse could be detected, therefore the pulse had to be simulated, including the associated shot noise. Previous measurements with optical return pulses have also been performed at the University of Berne (Gouman et al., 2014b). But since these measurements took place before the integration of the pi-filter (Kallenbach et al., 2016), the noise environment was not representative. Further, not all effects are testable under the given constraints. A significant uncertainty is the evolution of the detector and laser performance over the mission lifetime, also considering the seven years cruise phase. Further, the multiple mitigation strategies might lead to different behaviors of the avalanche photo diode (APD) (Barnes et al.,

2005), leaving some aspects of the performance unpredictable. Since most of the radiation effects lead to a degradation of the link budget its main consequence is a higher probability of false detection (PFD) and lower maximum altitude. Paper I showed that the performance of the instrument is almost uniquely PFD driven and that the ranging accuracy is secondary against pointing and interpolation errors. Therefore, as long as the total laser link budget stays in the specified range, the implications on the science performance should not be affected. Possible ways to re-increase the link budget are e.g., changing the high-voltage at the APD, which nominally only operates at half power.

Further, the thermal environment can lead to additional disturbances which are difficult to model. Paper I assumes that the post-launch alignment calibration strategy for BELA (Stark et al., 2017a) will be successful in order to minimize thermal effects in Mercury orbit. While the thesis aimed at identifying and modeling the dominant error sources that dictate the accuracy of the tidal measurements, there are a number of influences that have not been represented, e.g., thermal distortions or clock drifts. Further, it should be emphasized that a mission in orbit has to deal with numerous unpredictable challenges leading to modified operation or off-nadir pointing times. The studied Europa case is the most sensitive to this kind of events. For instance, the presence of active plumes in high latitude regions could change the mission profile between two flybys and therefore also the location of cross-over points. The nominal amount of 126 cross-over points is already a very low number compared to the $10^5 - 10^6$ cross-over points of the orbiter missions. Therefore, the sensitivity to spacecraft trajectory changes is very high.

To a lower extent this is also true for BELA and GALA. In the case of GALA there are nominal operation gaps every 8 hours which have been accounted for in Paper III. But for BELA the situation is more complicated. During periherm, the spacecraft enters a hot phase, requiring to change the orientation of the solar panels in order to avoid overheating. This procedure might lead to a power shortage not allowing for full science operation. However, large, measurable tidal amplitudes require the two passes at the cross-over points to occur at distinct phases in the tidal cycle. Therefore, the periherm is, together with the apoherm, the most important operation time for the tidal measurement. Under the given constraints, a successful tidal inversion without periherm measurements is unlikely to be successful.

The geodetic models are an important corner stone in the presented analysis. They are the transfer function from the instrument performance and given trajectories towards the geodetic parameters, which are then used to assess the scientific value. The algorithms for orbit determination Paper IV are based on cross-over points and radio science measurements and rely on numerical orbit integration. They provide a part of the functionality of software used for spacecraft navigation, for instance the well established MONTE software developed by JPL (e.g., Evans et al. (2016)). Comparison to similar analysis using MONTE done in the same framework also shows a good agreement.

The interior structure models computed for Mercury are also consistent with previous studies (Hauck et al., 2013; Knibbe and van Westrenen, 2015; Dumberry and Rivoldini, 2015) but the method used in Paper II relies on a slightly different approach. Instead of randomizing structural models and comparing the result to the given geodetic constraints, the algorithm conceived here uses the geodetic constraints to calculate the structural models such that they are consistent. This is done in an iterative process and allows to reduce the dimensions of the parameter space by the amount of given geodetic constraints. For Mercury, the method allows to generate valid structural models with less computational effort than to build them randomly by trial and error.

The Love number calculation is based on well established code (Wieczerkowski, 1999) as well. However, adaptions had to be made in order to allow for an arbitrary amount of layers. Previous versions of the code tended to numerical instability when the interior was subdivided into too many distinct layers. Also the possibility to use an Andrade rheology has been added. The code now gives results in excellent agreement with the code used in (Padovan et al., 2014).

The method proposed in Paper IV is in the first place a concept study since no comparable attempts to use a radar sounder for extended altimetric campaigns currently exist. However, important aspects of the study have been tested against well established simulation methods, mainly a point target simulator used at JPL and show good agreement. Since the proposed method has not been applied to actual measurements, future work should concentrate on evolving the suggested methods. For instance, data from the Shallow Radar (SHARAD) will be analyzed for Mars in combination with digital terrain models from the High Resolution Stereo Camera (HRSC) to obtain altimetric measurements. This application will on the one hand allow to refine the method suggested in Paper IV and on the other hand complement the MOLA data.

Chapter 7

Synthesis

This thesis aimed at the analysis of the radial tidal deformation measurements on Europa, Ganymede, and Mercury. In Paper I, a semi-analytical performance model for laser altimetry has been presented. Model and test results of the BELA flight model on board the BepiColombo spacecraft are in good agreement and therefore a significant improvement to previous work. The availability of an accurate performance model assures the compliance of the instrument with the scientific objectives of the mission. It has been further shown in Paper I that the measurement of Mercury's tidal Love number h_2 based on cross-over points will be very challenging for BELA during the nominal mission lifetime but possible with an 18% error after a one year mission extension. The importance of the measurement, however, has been emphasized in Paper II, by demonstrating that the h_2 measurement is key to set an upper bound on Mercury's inner core size via the h_2/k_2 ratio. The ratio gives a stronger constraint than previously inferred geodetic parameters. With the help of the models presented in Paper I other techniques possibly leading to a more accurate tidal measurement like from spherical harmonics expansion or co-registration can also be studied. This is currently work in progress.
For Ganymede, it has been shown in Paper III that GALA has bright perspectives to infer the tidal Love number h_2 from cross-over measurements. This is due to the significantly higher tidal amplitudes in presence of a subsurface ocean but also to the different design choices of the instrument. During the nominal mission lifetime, the absolute h_2 measurement accuracy is expected to be 0.026. In absence of a large phase-lag, and together with a nominal determination of Ganymede's tidal Love number k_2 by radio science, this allows to constrain the ice-shell thickness to $\pm$20 km.
The Europa Clipper has to rely on radar measurements for altimetry. A new method has been proposed and analysed in Paper IV. A very decisive impact for the h_2 measurement will however be the radio science configuration. Paper IV showed that in case of continuous radio science tracking, a determination of Europa's tidal Love number h_2 is possible with an accuracy below 0.17. This will allow for an ultimate evidence for a subsurface ocean and eventually also to set constraints on the ice shell thickness.
The thesis investigated the tidal measurement of three major upcoming missions. It presented models for the altimetric instruments, suggested methods for the geodetic inversion and provided estimates on the h_2 measurement accuracies. It further discussed how the tidal measurement can provide constraints on the interiors of Mercury, Ganymede, and Europa. But it also pointed out the challenges which have still to be overcome in the future.

Appendix A

Tidal Potential of Mercury

A.1. Second Order Eccentricity

The general form of the tidal potential is given as

$$V = \frac{GM}{a} \sum_{l=2}^{\infty} \left(\frac{r}{a}\right)^l P_l^0(\cos(\phi)). \tag{A.1}$$

Assuming that Mercury is on a Keplerian trajectory that can be described by the osculating elements $(a, e, i, M, \omega, \Omega)$ and expressing the angle of the subsolar point ϕ in latitude θ and longitude λ the potential becomes the form

$$V = \frac{GM}{a} \sum_{l=2}^{\infty} \left(\frac{r}{a}\right)^l \sum_{m=0}^{l} \frac{(m-l)!}{(m+l)!}(2-\delta_{0m}) P_l^m(\sin\theta) \tag{A.2}$$

$$\cdot \sum_{p=0}^{l} F_{lmp}(i) \sum_{q=-\infty}^{\infty} G_{lpq}(e) S_{lmpq}(\omega, M, \Omega, \Theta), \tag{A.3}$$

with

$$\delta_{0m} = \begin{cases} 0 & m \neq 0 \\ 1 & m = 0 \end{cases} \tag{A.4}$$

and

$$S_{lmpq} = \begin{bmatrix} C_{lm} \\ -S_{lm} \end{bmatrix}_{l-m \text{ odd}}^{l-m \text{ even}} \cos\left[(1-2p)\omega + (1-2p+q)M + m(\Omega-\Theta)\right] \tag{A.5}$$

$$+ \begin{bmatrix} S_{lm} \\ C_{lm} \end{bmatrix}_{l-m \text{ odd}}^{l-m \text{ even}} \sin\left[(1-2p)\omega + (1-2p+q)M + m(\Omega-\Theta)\right], \tag{A.6}$$

as well as

$$C_{lm} = \cos(m\lambda) \quad \text{and} \quad S_{lm} = \sin(m\lambda) \tag{A.7}$$

Expanding the potential up to degree and order two, we get

$$V_2 = \frac{GMr^2}{a^3}[P_2^0(\sin\theta) \sum_{p=0}^{2} F_{20p}(i) \sum_{q=-\infty}^{\infty} G_{2pq}(e) S_{20pq}(\omega, M, \Omega, \Theta) \tag{A.8}$$

$$+ \frac{1}{3} P_2^1(\sin\theta) \sum_{p=0}^{2} F_{21p}(i) \sum_{q=-\infty}^{\infty} G_{2pq}(e) S_{21pq}(\omega, M, \Omega, \Theta) \tag{A.9}$$

$$+ \frac{1}{12} P_2^2(\sin\theta) \sum_{p=0}^{2} F_{22p}(i) \sum_{q=-\infty}^{\infty} G_{2pq}(e) S_{22pq}(\omega, M, \Omega, \Theta)]. \tag{A.10}$$

The coefficients F_{lmp} and G_{lmp} can be calculated with the recipes given in Kaula (1964). For small inclinations the only non-zero inclination functions are $F_{201} = -\frac{1}{2}$ and $F_{220} = 3$. This simplifies the expression to

$$\begin{aligned} V_2 =& \frac{GMr^2}{a^3}[-\frac{1}{2}P_2^0(\sin\theta)\sum_{q=-\infty}^{\infty} G_{21q}(e)S_{201q}(\omega, M, \Omega, \Theta) \\ &+ \frac{3}{12}P_2^2(\sin\theta)\sum_{q=-\infty}^{\infty} G_{20q}(e)S_{220q}(\omega, M, \Omega, \Theta)]. \end{aligned} \tag{A.11}$$

For second order in eccentricity, the coefficients G_{2mq} are shown in Table A.1.

m \ q	-2	-1	0	1	2
-2	$\frac{15e^2}{2}$	$-\frac{9}{2}$	$1-\frac{69e^2}{2}$	$\frac{15e}{2}$	$33e^2$
-1	$\frac{7e^2}{4}$	$-\frac{5e}{2}$	$1-\frac{29e^2}{2}$	$\frac{11e}{2}$	$\frac{75e^2}{4}$
0	0	$-\frac{e}{2}$	$1-\frac{5e^2}{2}$	$\frac{7e}{2}$	$\frac{17e^2}{2}$
1	$\frac{9e^4}{2}$	$-\frac{3e}{2}$	$1+\frac{3e^2}{2}$	$\frac{3e}{2}$	$\frac{9e^2}{4}$
2	$\frac{17e^2}{2}$	$-\frac{7e}{2}$	$1-\frac{5e^2}{2}$	$-\frac{e}{2}$	0

Table A.1: G_{2mq} coefficients according to Kaula (1964).

Inserting the coefficients from Table A.1 into Equation (A.11) leads to the expression

$$\begin{aligned} V_2 =& -\frac{GMr^2}{8a^3}[P_2^0(\sin\theta)\left(4S_{2010} + 6eS_{201-1} + S_{2011} + e^2(S_{201-2} + 6S_{2010} + 9S_{2012})\right) \\ &+ P_2^2(\sin\theta)\left(-2S_{2200} + eS_{220-1} - 7S_{2201} + e^2(5S_{2200} - 17S_{2202})\right)]. \end{aligned} \tag{A.12}$$

For a body in a m:n mean motion resonance $\omega + \left(\frac{n}{m}\right)M + \Omega - \Theta = 0$. Using this relation we can calculate the coefficients S_{lmpq}:

$$\begin{aligned} S_{201-2} &= \cos(2M) & S_{220-2} &= \cos(3M + 2\lambda) \\ S_{201-1} &= \cos(M) & S_{220-1} &= \cos(2M + 2\lambda) \\ S_{2010} &= 1 & S_{2200} &= \cos(M + 2\lambda) \\ S_{2011} &= \cos(M) & S_{2201} &= \cos(M + \lambda) \\ S_{2012} &= \cos(2M) & S_{2202} &= \cos(M - \lambda). \end{aligned}$$

The coefficient S_{2010} generates a constant term and therefore generates no force on the planet. Inserting the remaining coefficients we obtain the final potential

$$\begin{aligned} V_2 = \Phi_2 =& \frac{GMr^2}{8a^3}\Big\{2\left[2 + 3e^2 + 6e\cos(M) + 9e^2\cos(2M)\right]P_2^0 + \big[-17e^2\cos(M - 2\lambda) \\ &- 7e\cos(2\lambda) + e\cos(2M + 2\lambda) - 2\cos(M + 2\lambda) + 5e^2\cos(M + 2\lambda)\big]P_2^2\Big\}. \end{aligned} \tag{A.13}$$

In[1]:= **Input parameters**

Out[1]= Input parameters

In[2]:=
```
oi = 0; (* Order inclination *)
oe = 4; (* Order eccentricity *)
lmax = 2; (* Order in l *)
res = 3/2; (* Resonance *)
```

In[59]:= **Coefficients F, G &S**

In[4]:=
```
F[l_, m_, p_] := Normal[Series[Sum[(2 l - 2 t)! Sin[i]^(l-m-2 t) / (t! (l - t)! (l - m - 2 t)! 2^(2 l-2 t)) Sum[Binomial[m, s] Cos[i]^s Sum[Binomial[l - m - 2 t + s, c] Binomial[m - s, p - t - c] (-1)^(c-IntegerPart[(l-m)/2]), {i, 0, oi}], {s, 0, m}], {t, 0, Min[p, IntegerPart[(l-m)/2]]}]]

S[l_, m_, p_, q_] := Cos[m λ] Cos[(l - 2 p) ω + (l - 2 p + q) M + m (Ω - Θ)] + Sin[m λ] Sin[(l - 2 p) ω + (l - 2 p + q) M + m (Ω - Θ)]

Θ := ω + res M + Ω

β[e_] := e / (1 + (1 - e^2)^(1/2))

q2[l_, p_, q_] := If[p ≤ 1/2, q, -q]

h[l_, p_, q_, k_] := If[q2[l, p, q] > 0, k + q2[l, p, q], k]
h2[l_, p_, q_, k_] := If[q2[l, p, q] > 0, k, k - q2[l, p, q]]

p2[l_, p_, q_] := If[p ≤ 1/2, p, 1 - p]

P[l_, p_, q_, k_, e_] :=
 Sum[Binomial[2 p2[l, p, q] - 2 l, h[l, p, q, k] - r] (-1)^r / r! (e (1 - 2 p2[l, p, q] + q2[l, p, q]) / (2 β[e]))^r, {r, 0, h[l, p, q, k]}]

Q[l_, p_, q_, k_, e_] :=
 Sum[Binomial[-2 p2[l, p, q], h2[l, p, q, k] - r] 1/r! (e (1 - 2 p2[l, p, q] + q2[l, p, q]) / (2 β[e]))^r, {r, 0, h2[l, p, q, k]}]

Ge[l_, p_, q_, e_] := (-1)^Abs[q] (1 + β[e]^2)^l β[e]^Abs[q] Sum[P[l, p, q, k, e] Q[l, p, q, k, e] β[e]^(2 k), {k, 0, 2}]

G[l_, p_, q_] := If[l == 2 && p == 1 && q == 0, Normal[Series[(1 - e^2)^(-3/2), {e, 0, oe}]], If[l - 2 p + q == 0, 0, Normal[Series[Ge[l, p, q, e], {e, 0, oe}]]]]
```

In[16]:= **Tidal potential with static components**

Out[16]= components potential static Tidal with

In[17]:=
```
V = Simplify[gm/R Sum[(r/R)^l (l - m)!/(l + m)! (2 - (KroneckerDelta[0, m])) P_{l,m} Sum[F[l, m, p], {p, 0, l}] Sum[G[l, p, q], {q, -30, 30}] S[l, m, p, q], {m, 0, l}], {l, 2, lmax}]
```

Out[17]=
$$-\frac{1}{192\,R^3}gm\,r^2\left(12\left(8+12\,e^2+15\,e^4+3\,e\left(8+9\,e^2\right)\text{Cos}[M]+4\,e^2\left(9+7\,e^2\right)\text{Cos}[2\,M]+53\,e^3\,\text{Cos}[3\,M]+77\,e^4\,\text{Cos}[4\,M]\right)P_{2,0}-\left(-8\,e^2\left(-51+115\,e^2\right)\text{Cos}[M-2\,\lambda]+1599\,e^4\,\text{Cos}[3\,M-2\,\lambda]+845\,e^3\,\text{Cos}[2\,(M-\lambda)]+168\,e\,\text{Cos}[2\,\lambda]-369\,e^3\,\text{Cos}[2\,\lambda]-24\,e\,\text{Cos}[2\,(M+\lambda)]+3\,e^3\,\text{Cos}[2\,(M+\lambda)]+e^3\,\text{Cos}[2\,(2\,M+\lambda)]+48\,\text{Cos}[M+2\,\lambda]-120\,e^2\,\text{Cos}[M+2\,\lambda]+39\,e^4\,\text{Cos}[M+2\,\lambda]+2\,e^4\,\text{Cos}[5\,M+2\,\lambda]\right)P_{2,2}\right)$$

In[18]= **Tidal potential with periodic components only**

Out[18]= components only periodic potential Tidal with

In[19]=
```
Vd = FullSimplify[V - Integrate[V, {M, 0, 2 π}] / (2 π)]
 (* Tidal potential without static components*)
```

Out[19]=
$$\frac{1}{192\,R^3}gm\,r^2\left(-12\,e\left(3\left(8+9\,e^2\right)\text{Cos}[M]+e\left(4\left(9+7\,e^2\right)\text{Cos}[2\,M]+53\,e\,\text{Cos}[3\,M]+77\,e^2\,\text{Cos}[4\,M]\right)\right)P_{2,0}+\left(48\,\text{Cos}[M+2\,\lambda]+e\left(-24\,\text{Cos}[2\,(M+\lambda)]+e\left(\left(408-920\,e^2\right)\text{Cos}[M-2\,\lambda]-120\,\text{Cos}[M+2\,\lambda]+e\,(845\,\text{Cos}[2\,(M-\lambda)]+3\,\text{Cos}[2\,(M+\lambda)]+\text{Cos}[2\,(2\,M+\lambda)]+39\,e\,(41\,\text{Cos}[3\,M-2\,\lambda]+\text{Cos}[M+2\,\lambda])+2\,e\,\text{Cos}[5\,M+2\,\lambda]\right)\right)\right)P_{2,2}\right)$$

Bibliography

Abshire, J.B., Sun, X., Afzal, R.S.. Mars Orbiter Laser Altimeter: Receiver Model and Performance Analysis. Applied Optics 2000;39:2449–2460. doi:10.1364/AO.39.002449.

Aglyamov, Y., Schroeder, D.M., Vance, S.D.. Bright prospects for radar detection of Europa's ocean. Icarus 2017;281:334–337. doi:10.1016/j.icarus.2016.08.014.

Althaus, C., Michaelis, H., Lingenauber, K., Behnke, T., Togno, S.d., Kallenbach, R., Wickhusen, K., Althaus, C.. Optical Performance Measurements of the BELA EQM and FM Transmitter Laser during AIV. European Planetary Science Congress 2014;9:EPSC2014–337.

Anderson, B.J., Johnson, C.L., Korth, H., Purucker, M.E., Winslow, R.M., Slavin, J.A., Solomon, S.C., McNutt, R.L., Raines, J.M., Zurbuchen, T.H.. The Global Magnetic Field of Mercury from MESSENGER Orbital Observations. Science 2011;333(6051):1859–1862. doi:10.1126/science.1211001.

Anderson, J., Schubert, G., Jacobson, R., Lau, E., Moore, W., Sjogren, W.. Europa's differentiated internal structure: Inferences from four Galileo encounters. Science 1998;281(5385):2019–2022.

Baland, R.M., Yseboodt, M., Van Hoolst, T.. Obliquity of the galilean satellites: The influence of a global internal liquid layer. Icarus 2012;220(2):435 – 448. doi:10.1016/j.icarus.2012.05.020.

Balogh, A., Giampieri, G.. Mercury: the planet and its orbit. Reports on Progress in Physics 2002;65(4):529.

Barnes, C., Ott, M., Becker, H., Wright, M., Johnston, A., Marshall, C., Shaw, H., Marshall, P., LaBel, K., Franzen, D.. NASA Electronic Parts and Packaging (NEPP) Program: assurance research on optoelectronics. In: Taylor, E.W., editor. Photonics for Space Environments X. volume 5897 of *Proceedings of the SPIE*; 2005. p. 67–83. doi:10.1117/12.619289.

Bauer, S., Hussmann, H., Oberst, J., Dirkx, D., Mao, D., Neumann, G.A., Mazarico, E., Torrence, M.H., McGarry, J.F., Smith, D.E., Zuber, M.T.. Analysis of one-way laser ranging data to LRO, time transfer and clock characterization. Icarus 2017;283:38–54. doi:10.1016/j.icarus.2016.09.026.

Beck, T.. Modeling and verification of BELA's thermal behavior and range finder performance. Ph.D. thesis; Institute of Physics at the University of Berne; 2012.

Beck, T., Lüthi,B.S., , Messina, G., Piazza, D., Seiferlin, K., Thomas, N.. Thermal analysis of a reflective baffle designed for space applications. Acta Astronautica 2011;69(5):323 – 334. doi:10.1016/j.actaastro.2011.03.014.

Benkhoff, J., van Casteren, J., Hayakawa, H., Fujimoto, M., Laakso, H., Novara, M., Ferri, P., Middleton, H.R., Ziethe, R.. BepiColombo-Comprehensive exploration of Mercury: Mission overview and science goals . Planetary and Space Science 2010;58(1-2):2 – 20. doi:10.1016/j.pss.2009.09.020.

Benveniste, J., Resti, A., Roca, M., Milagro-Perez, M.P., Levrini, G.. ENVISAT radar altimeter system. In: Bostater, C.R., Santoleri, R., editors. Remote Sensing of the Ocean and Sea Ice 2001. volume 4544 of *Proceedings of the SPIE*; 2002. p. 71–82. doi:10.1117/12.452745.

Berquin, Y., Kofman, W., Herique, A., Alberti, G., Beck, P.. A study on Ganymede's surface topography: Perspectives for radar sounding. Planetary and Space Science 2013;77(0):40 – 44. doi:10.1016/j.pss.2012.07.004.

Bland, M.T., Showman, A.P., Tobie, G.. The production of Ganymede's magnetic field. Icarus 2008;198:384–399. doi:10.1016/j.icarus.2008.07.011.

Bland, M.T., Showman, A.P., Tobie, G.. The orbital-thermal evolution and global expansion of ganymede. Icarus 2009;200(1):207–221. doi:10.1016/j.icarus.2008.11.016.

Blankenship, D., Young, D., Moore, W., Moore, J.. Eruopa; The University of Arizona Press.

Bruzzone, L., Plaut, J.J., Alberti, G., Blankenship, D.D., Bovolo, F., Campbell, B.A., Ferro, A., Gim, Y., Kofman, W., Komatsu, G., McKinnon, W., Mitri, G., Orosei, R., Patterson, G.W., Plettemeier, D., Seu, R.. RIME: Radar for Icy Moon Exploration. European Planetary Science Congress 2013;8:EPSC2013–744.

Byrne, P., Klimczak, C., Celâl Şengör, A., Solomon, S., Watters, T., Hauck II, S.. Mercury's global contraction much greater than earlier estimates. Nature Geoscience 2014;7:301–307. doi:10.1038/ngeo2097.

Cavanaugh, J.F., Smith, J.C., Sun, X., Bartels, A.E., Krebs, D.J., McGarry, J.F., Trunzo, R., Novo-Gradac, A.M., Britt, J.L., Karsh, J., Katz, R.B., Lukemire, A.T., Szymkiewicz, R., Berry, D.L., Swinski, J.P., Neumann, G.A., Zuber, M.T., Smith, D.E.. The Mercury Laser Altimeter Instrument for the MESSENGER Mission. Space Science Reviews 2007;131(1):451–479. doi:10.1007/s11214-007-9273-4.

Cecconi, B., Hess, S., Hérique, A., Santovito, M., Santos-Costa, D., Zarka, P., Alberti, G., Blankenship, D., Bougeret, J.L., Bruzzone, L., Kofman, W.. Natural radio emission of jupiter as interferences for radar investigations of the icy satellites of jupiter. Planetary and Space Science 2012;61(1):32 – 45. doi:10.1016/j.pss.2011.06.012.

Chicarro, A.F., Science Team, . The Mars Express Mission and Its Beagle-2 Lander. In: Albee, A.L., Kieffer, H.H., editors. Sixth International Conference on Mars. 2003. .

Chin, G., Brylow, S., Foote, M., Garvin, J., Kasper, J., Keller, J., Litvak, M., Mitrofanov, I., Paige, D., Raney, K., Robinson, M., Sanin, A., Smith, D., Spence, H., Spudis, P., Stern, S.A., Zuber, M.. Lunar reconnaissance orbiter overview: The instrument suite and mission. Space Science Reviews 2007;129(4):391–419. doi:10.1007/s11214-007-9153-y.

Choblet, G., Tobie, G., Sotin, C., Kalousová, K., Grasset, O.. Heat transport in the high-pressure ice mantle of large icy moons. Icarus 2017;285:252–262. doi:10.1016/j.icarus.2016.12.002.

Colombo, G., Shapiro, I.. The Rotation of the Planet Mercury. apj 1966;145:296. doi:10.1086/148762.

Deutsch, A.N., Chabot, N.L., Mazarico, E., Ernst, C.M., Head, J.W., Neumann, G.A., Solomon, S.C.. Comparison of areas in shadow from imaging and altimetry in the north polar region of Mercury and implications for polar ice deposits. Icarus 2016;280:158–171. doi:10.1016/j.icarus.2016.06.015.

Deutsch, A.N., Head, J., Chabot, N., Neumann, G.. "constraining the thickness of polar ice deposits on mercury using the mercury laser altimeter and small craters in permanently shadowed regions". Icarus 2018;305:139 – 148. doi:10.1016/j.icarus.2018.01.013.

Dowdeswell, J., Evans, S.. Investigations of the form and flow of ice sheets and glaciers using radio-echo sounding. Reports on Progress in Physics 2004;67(10):1821.

Dumberry, M., Rivoldini, A.. Mercury's inner core size and core-crystallization regime. Icarus 2015;248:254 – 268.

Edwards, B.C., Chyba, C.F., Abshire, J.B., Burns, J.A., Geissler, P., Konopliv, A.S., Malin, M.C., Ostro, S.J., Rhodes, C., Rudiger, C., Shao, X.M., Smith, D.E., Squyres, S.W., Thomas, P.C., Uphoff, C.W., Walberg, G.D., Werner, C.L., Yoder, C.F., Zuber, M.T.. The Europa Ocean

Discovery mission. In: Hoover, R.B., editor. Instruments, Methods, and Missions for the Investigation of Extraterrestrial Microorganisms. volume 3111 of *Proc. SPIE*; 1997. p. 249–261. doi:10.1117/12.278778.

Elachi, C., Allison, M.D., Borgarelli, L., Encrenaz, P., Im, E., Janssen, M.A., Johnson, W.T.K., Kirk, R.L., Lorenz, R.D., Lunine, J.I., Muhleman, D.O., Ostro, S.J., Picardi, G., Posa, F., Rapley, C.G., Roth, L.E., Seu, R., Soderblom, L.A., Vetrella, S., Wall, S.D., Wood, C.A., Zebker, H.A.. Radar: The Cassini Titan Radar Mapper. Space Science Reviews 2004;115:71–110. doi:10.1007/s11214-004-1438-9.

Elachi, C., Wall, S., Janssen, M., Stofan, E., Lopes, R., Kirk, R., Lorenz, R., Lunine, J., Paganelli, F., Soderblom, L., Wood, C., Wye, L., Zebker, H., Anderson, Y., Ostro, S., Allison, M., Boehmer, R., Callahan, P., Encrenaz, P., Flamini, E., Francescetti, G., Gim, Y., Hamilton, G., Hensley, S., Johnson, W., Kelleher, K., Muhleman, D., Picardi, G., Posa, F., Roth, L., Seu, R., Shaffer, S., Stiles, B., Vetrella, S., West, R.. Titan Radar Mapper observations from Cassini's T_3 fly-by. Nature 2006;441:709–713. doi:10.1038/nature04786.

Evans, S., Taber, T., Smith, H., Wu, M., Guevara, R., Sunseri, R., Evans, J.. MONTE: The next generation of mission design & navigation software. The 6th International Conference on Astrodynamics Tools and Techniques (ICATT) 2016;.

Figueredo, P.H., Greeley, R.. Geologic mapping of the northern leading hemisphere of Europa from Galileo solid-state imaging data. Journal of Geophysical Research: Planets 2000;105(E9):22629–22646. doi:10.1029/1999JE001107.

Fretwell, P., Pritchard, H.D., Vaughan, D.G., Bamber, J.L., Barrand, N.E., Bell, R., Bianchi, C., Bingham, R.G., Blankenship, D.D., Casassa, G., Catania, G., Callens, D., Conway, H., Cook, A.J., Corr, H.F.J., Damaske, D., Damm, V., Ferraccioli, F., Forsberg, R., Fujita, S., Gim, Y., Gogineni, P., Griggs, J.A., Hindmarsh, R.C.A., Holmlund, P., Holt, J.W., Jacobel, R.W., Jenkins, A., Jokat, W., Jordan, T., King, E.C., Kohler, J., Krabill, W., Riger-Kusk, M., Langley, K.A., Leitchenkov, G., Leuschen, C., Luyendyk, B.P., Matsuoka, K., Mouginot, J., Nitsche, F.O., Nogi, Y., Nost, O.A., Popov, S.V., Rignot, E., Rippin, D.M., Rivera, A., Roberts, J., Ross, N., Siegert, M.J., Smith, A.M., Steinhage, D., Studinger, M., Sun, B., Tinto, B.K., Welch, B.C., Wilson, D., Young, D.A., Xiangbin, C., Zirizzotti, A.. Bedmap2: improved ice bed, surface and thickness datasets for Antarctica. The Cryosphere 2013;7:375–393. doi:10.5194/tc-7-375-2013.

Gardner, C.. Ranging Performance of Satellite Laser Altimeters. "IEEE Transactions on Geoscience and Remote Sensing" 1992;30 No 5:1061–1072.

Gardner, C.S.. Target signatures for laser altimeters: an analysis. Appl Opt 1982;21(3):448–453. doi:10.1364/AO.21.000448.

Genova, A., Iess, L., Marabucci, M.. Mercury's gravity field from the first six months of MESSENGER data. Planetary and Space Science 2013;81:55–64. doi:10.1016/j.pss.2013.02.006.

Gogineni, S., Yan, J.B., Paden, J., Leuschen, C., Li, J., Rodriguez-Morales, F., Braaten, D., Purdon, K., Wang, Z., Liu, W., Gauch, J.. Bed topography of Jakobshavn Isbræ, Greenland, and Byrd Glacier, Antarctica. Journal of Glaciology 2014;60:813–833. doi:10.3189/2014JoG14J129.

Goldreich, P.. On the eccentricity of satellite orbits in the solar system. Monthly Notices of the Royal Astronomical Society 1963;126:257. doi:10.1093/mnras/126.3.257.

Goldreich, P.. Tidal De-spin of Planets and Satellites. Nature 1965;208:375–376. doi:10.1038/208375b0.

Goldreich, P., Peale, S.. Spin-orbit coupling in the solar system. Astronomical Journal 1966;71:425. doi:10.1086/109947.

Gouman, J., Beck, T., Affolter, M., Thomas, N., Geissbühler, U., Péteut, A., Bandy, T., Servonet, A., Piazza, D., Seiferlin, K.. Measurement and stability of the pointing of the BepiColombo Laser Altimeter under thermal load. European Planetary Science Congress 2014a;9:EPSC2014–66.

Gouman, J., Thomas, N., Marti, K.S., Beck, T., Péteut, A., Pommerol, A.. BepiColombo Laser Altimeter performance tests. European Planetary Science Congress 2014b;9:EPSC2014–64.

Grasset, O., Dougherty, M., Coustenis, A., Bunce, E., Erd, C., Titove, D., Blanc, M., Coates, A., Drossart, P., Fletcher, L., Hussmann, H., Jaumann, R., Krupp, N., Lebreton, J.P., Prieto-Ballesteros, O., Tortora, P., Tosi, F., Van Hoolst, T.. JUpiter ICy moons Explorer (JUICE): An ESA mission to orbit Ganymede and to characterise the Jupiter system. Planeary and Space Science 2013;78. doi:10.1016/j.pss.2012.12.002.

Greenbaum, J.S., Blankenship, D.D., Young, D.A., Richter, T.G., Roberts, J.L., Aitken, A.R.A., Legresy, B., Schroeder, D.M., Warner, R.C., van Ommen, T.D., Siegert, M.J.. Ocean access to a cavity beneath Totten Glacier in East Antarctica. Nature Geoscience 2015;8:294–298. doi:10.1038/ngeo2388.

Greenberg, R., Hoppa, G.V., Tufts, B., Geissler, P., Riley, J., Kadel, S.. Chaos on europa. Icarus 1999;141(2):263 – 286. doi:10.1006/icar.1999.6187.

Grima, C., Blankenship, D.D., Schroeder, D.M.. Radar signal propagation through the ionosphere of Europa. Planetary and Space Science 2015a;117:421–428. doi:10.1016/j.pss.2015.08.017.

Grima, C., Blankenship, D.D., Schroeder, D.M., Moussessian, A., Soderlund, K.M., Gim, Y., Plaut, J.J., Greenbaum, J.S., Lopez Garcia, E., Campbell, B.A., Putzig, N.E., Patterson, G.. Surface Reflectometry and Ionosphere Sounding from the Radar for Europa Assessment and Sounding: Ocean to Near-surface (REASON). AGU Fall Meeting Abstracts 2015b;:P11C–2110.

Grott, M., Breuer, D., Laneuville, M.. Thermo-chemical evolution and global contraction of Mercury. Earth and Planetary Science Letters 2011;307(1):135 – 146. doi:10.1016/j.epsl.2011.04.040.

Gunderson, K., Thomas, N.. BELA receiver performance modeling over the BepiColombo mission lifetime. Planetary and Space Science 2010;58:309–318.

Gunderson, K., Thomas, N., Rohner, M.. A laser altimeter performance model and its application to BELA. "IEEE Transactions on Geoscience and Remote Sensing" 2006;44 No 11:3308–3319.

Hauck, S.A., Margot, J.L., Solomon, S.C., Phillips, R.J., Johnson, C.L., Lemoine, F.G., Mazarico, E., McCoy, T.J., Padovan, S., Peale, S.J., Perry, M.E., Smith, D.E., Zuber, M.T.. The curious case of mercury's internal structure. Journal of Geophysical Research: Planets 2013;118(6):1204–1220. doi:10.1002/jgre.20091.

Hauck, S.A., Solomon, S.C., Smith, D.A.. Predicted recovery of Mercury's internal structure by MESSENGER. Geophysical Research Letters 2007;34(18):L18201. URL: 10.1029/2007GL030793. doi:10.1029/2007GL030793.

Head, J., Pappalardo, R., Collins, G., Belton, M.J.S., Giese, B., Wagner, R., Breneman, H., Spaun, N., Nixon, B., Neukum, G., Moore, J.. Evidence for Europa-like tectonic resurfacing styles on Ganymede. Geophysical Research Letters 2002;29(24):4–1–4–4. doi:10.1029/2002GL015961; 2151.

Head, J., Pappalardo, R., Kay, J., Collins, G., Prockter, L., Greeley, R., Chapman, C., Carr, M., Belton, M., Galileo Imaging Team, . Cryovolcanism on Ganymede: Evidence in Bright Terrain from Galileo Solid State Imaging Data. In: Lunar and Planetary Science Conference. volume 29; 1998. .

Head, J.W., Chapman, C.R., Strom, R.G., Fassett, C.I., Denevi, B.W., Blewett, D.T., Ernst, C.M., Watters, T.R., Solomon, S.C., Murchie, S.L., Prockter, L.M., Chabot, N.L., Gillis-Davis, J.J., Whitten, J.L., Goudge, T.A., Baker, D.M.H., Hurwitz, D.M., Ostrach, L.R., Xiao, Z., Merline, W.J., Kerber, L., Dickson, J.L., Oberst, J., Byrne, P.K., Klimczak, C., Nittler, L.. Flood Volcanism in the Northern High Latitudes of Mercury Revealed by MESSENGER. Science 2011;333(6051):1853–1856. doi:10.1126/science.1211997.

Hosseiniarani, A., Bertone, S., Jäggi, A., Thomas, N.. Bepicolombo Laser Altimeter (BELA) contributions to MPO orbit improvement towards a better determination of Mercury geophysical parameters. European Planetary Science Congress 2017;11:EPSC2017–682.

Hussmann, H., Lingenauber, K., Oberst, J., Enya, K., Kobayashi, M., Namiki, N., Kimura, J., Thomas, N., Lara, L., Steinbrügge, G., Stark, A., Luedicke, F., Behnke, T., Althaus, C., Del Togno, S., Borgs, B., Michaelis, H., Jänchen, J., Kallenbach, R.. The Ganymede Laser Altimeter (GALA). European Planetary Science Congress 2017;11:EPSC2017–567.

Hussmann, H., Lingenauber, K., Oberst, J., Kobayashi, M., Namiki, N., Kimura, J., Thomas, N., Lara, L., Steinbrügge, G.. The Ganymede Laser Altimeter (GALA). European Planetary Science Congress 2014;9:EPSC2014–347.

Hussmann, H., Shoji, D., Steinbrügge, G., Stark, A., Sohl, F.. Constraints on dissipation in the deep interiors of ganymede and europa from tidal phase-lags. Celestial Mechanics and Dynamical Astronomy 2016;126(1):131–144. doi:10.1007/s10569-016-9721-0.

Hussmann, H., Sohl, F., Oberst, J.. Measuring tidal deformations at Europa's surface. Advances in Space Research 2011;48:718–724. doi:10.1016/j.asr.2010.06.001.

Hussmann, H., Spohn, T., Wieczerkowski, K.. Thermal Equilibrium States of Europa's Ice Shell: Implications for Internal Ocean Thickness and Surface Heat Flow. Icarus 2002;156(1):143 – 151. doi:10.1006/icar.2001.6776.

Iess, L.. 3GM: Gravity and Geophysics of Jupiter and the Galilean Moons. European Planetary Science Congress 2013;8:EPSC2013–491.

Iess, L., Boscagli, G.. Advanced radio science instrumentation for the mission BepiColombo to Mercury. Planetary and Space Science 2001;49:1597–1608. doi:10.1016/S0032-0633(01)00096-4.

Imperi, L., Iess, L., M.ni, M.J.. An analysis of the geodesy and relativity experiments of BepiColombo. Icarus 2018;301:9025. doi:10.1016/j.icarus.2017.09.008.

Jordan, R., Picardi, G., Plaut, J., Wheeler, K., Kirchner, D., Safaeinili, A., Johnson, W., Seu, R., Calabrese, D., Zampolini, E., Cicchetti, A., Huff, R., Gurnett, D., Ivanov, A., Kofman, W., Orosei, R., Thompson, T., Edenhofer, P., Bombaci, O.. The Mars express MARSIS sounder instrument. Planetary and Space Science 2009;57:1975–1986. doi:10.1016/j.pss.2009.09.016.

Kallenbach, R., Behnke, T., Perplies, H., Henkelmann, R., Rech, M., Geissbühler, U., Péteut, A., Lichopoj, A., Schroedter, R., Michaelis, H., Seiferlin, K., Thomas, N., Castro, J.M., Herranz, M., Lara, L.. Electromagnetic compatibility of transmitter, receiver, and communication port of a space-qualified laser altimeter. 2016 ESA Workshop on Aerospace EMC (Aerospace EMC) 2016;:1–7.

Kalousova, K., Sotin, C., Choblet, G., Tobie, G., Grasset, O.. "two-phase convection in ganymede's high-pressure ice layer - implications for its geological evolution". Icarus 2018;299:133 – 147. doi:10.1016/j.icarus.2017.07.018.

Kamata, S., Kimura, J., Matsumoto, K., Nimmo, F., Kuramoto, K., Namiki, N.. Tidal deformation of Ganymede: Sensitivity of Love numbers on the interior structure. Journal of Geophysical Research (Planets) 2016;121:1362–1375. doi:10.1002/2016JE005071.

Kaula, W.. Tidal dissipation by solid friction and the resulting orbital evolution. Reviews of Geophysics 1964;2:661–685. doi:10.1029/RG002i004p00661.

Khurana, K.K., Jia, X., Kivelson, M.G., Nimmo, F., Schubert, G., Russell, C.T.. Evidence of a Global Magma Ocean in Io's Interior. Science 2011;332:1186. doi:10.1126/science.1201425.

Khurana, K.K., Kivelson, M.G., Stevenson, D.J., Schubert, G., Russell, C.T., Walker, R.J., Polanskey, C.. Induced magnetic fields as evidence for subsurface oceans in Europa and Callisto. Nature 1998;395:777–780. doi:10.1038/27394.

Kivelson, M., Khurana, K., Volwerk, M.. The permanent and inductive magnetic moments of Ganymede. Icarus 2002;157:507–522. doi:10.1006/icar.2002.6834.

Kivelson, M.G., Khurana, K.K., Russell, C.T., Volwerk, M., Walker, R.J., Zimmer, C.. Galileo magnetometer measurements: A stronger case for a subsurface ocean at europa. Science 2000;289(5483):1340–1343. doi:10.1126/science.289.5483.1340.

Kivelson, M.G., Khurana, K.K., Stevenson, D.J., Bennett, L., Joy, S., Russell, C.T., Walker, R.J., Zimmer, C., Polanskey, C.. Europa and Callisto: Induced or intrinsic fields in a periodically varying plasma environment. Journal of Geophysical Research 1999;104:4609–4626. doi:10.1029/1998JA900095.

Kliore, A.J., Anabtawi, A., Herrera, R.G., Asmar, S.W., Nagy, A.F., Hinson, D.P., Flasar, F.M.. Ionosphere of callisto from galileo radio occultation observations. Journal of Geophysical Research: Space Physics 2002;107(A11):SIA 19–1–SIA 19–7. doi:10.1029/2002JA009365.

Knibbe, J.S., van Westrenen, W.. The interior configuration of planet mercury constrained by moment of inertia and planetary contraction. Journal of Geophysical Research: Planets 2015;120(11):1904–1923. doi:10.1002/2015JE004908; 2015JE004908.

Koch, C., Christensen, U., Kallenbach, R.. Simultaneous determination of global topography, tidal Love number and libration amplitude of Mercury by laser altimetry. Planetary and Space Science 2008;56(9):1226 – 1237. doi:10.1016/j.pss.2008.04.002.

Koch, C., Kallenbach, R., Christensen, U.. Mercury's global topography and tidal signal from laser altimetry by using a rectangular grid. Planetary and Space Science 2010;58(14):2022 – 2030. doi:10.1016/j.pss.2010.10.002.

Kreslavsky, M.A., Head, J.W., Neumann, G.A., Rosenburg, M.A., Aharonson, O., Smith, D.E., Zuber, M.T.. Lunar topographic roughness maps from Lunar Orbiter Laser Altimeter (LOLA) data: Scale dependence and correlation with geologic features and units. Icarus 2013;226:52–66. doi:10.1016/j.icarus.2013.04.027.

Kreslavsky, M.A., Head, J.W., Neumann, G.A., Zuber, M.T., Smith, D.E.. "kilometer-scale topographic roughness of mercury: Correlation with geologic features and units". Geophysical Research Letters 2014;41(23):8245–8251. doi:10.1002/2014GL062162.

Lemoine, F., Smith, D., Rowlands, D., Zuber, M., Neumann, G., Chinn, D., Pavlis, D.. An improved solution of the gravity field of Mars (GMM-2B) from Mars Global Surveyor. Journal of Geophysical Research 2001;106:23359–23376. doi:10.1029/2000JE001426.

Löcher, A., Kusche, J.. Orbit determination of the Lunar Reconnaissance Orbiter using laser ranging and radiometric tracking data. In: EGU General Assembly Conference Abstracts. volume 16 of *EGU General Assembly Conference Abstracts*; 2014. p. 5488.

Lopes, R.M.C., Mitchell, K.L., Stofan, E.R., Lunine, J.I., Lorenz, R., Paganelli, F., Kirk, R.L., Wood, C.A., Wall, S.D., Robshaw, L.E., Fortes, A.D., Neish, C.D., Radebaugh, J., Reffet, E., Ostro, S.J., Elachi, C., Allison, M.D., Anderson, Y., Boehmer, R., Boubin, G., Callahan, P., Encrenaz, P., Flamini, E., Francescetti, G., Gim, Y., Hamilton, G., Hensley, S., Janssen, M.A., Johnson, W.T.K., Kelleher, K., Muhleman, D.O., Ori, G., Orosei, R., Picardi, G., Posa, F., Roth, L.E., Seu, R., Shaffer, S., Soderblom, L.A., Stiles, B., Vetrella, S., West, R.D., Wye, L., Zebker, H.A.. Cryovolcanic features on Titan's surface as revealed by the Cassini Titan Radar Mapper. Icarus 2007;186:395–412. doi:10.1016/j.icarus.2006.09.006.

Love, A.. Earth, the yielding of the, to disturbing forces. Monthly Notices of the Royal Astronomical Society 1909;69:476. doi:10.1093/mnras/69.6.476.

Lucey, P.G., Neumann, G.A., Riner, M.A., Mazarico, E., Smith, D.E., Zuber, M.T., Paige, D.A., Bussey, D.B., Cahill, J.T., McGovern, A., Isaacson, P., Corley, L.M., Torrence, M.H., Melosh, H.J., Head, J.W., Song, E.. The global albedo of the Moon at 1064 nm from LOLA. Journal of Geophysical Research (Planets) 2014;119:1665–1679. doi:10.1002/2013JE004592.

MacGregor, J.A., Fahnestock, M.A., Catania, G.A., Paden, J.D., Prasad Gogineni, S., Young, S.K., Rybarski, S.C., Mabrey, A.N., Wagman, B.M., Morlighem, M.. Radiostratigraphy and age

structure of the Greenland Ice Sheet. Journal of Geophysical Research (Earth Surface) 2015;120:212–241. doi:10.1002/2014JF003215.

Makarov, V., Efroimsky, M.. Tidal Dissipation in a Homogeneous Spherical Body. II. Three Examples: Mercury, IO, and Kepler-10 b. The Astrophysical Journal 2014;795:7. doi:10.1088/0004-637X/795/1/7.

Makarov, V.V.. Conditions of passage and entrapment of terrestrial planets in spin-orbit resonances. The Astrophysical Journal 2012;752(1):73.

Malavergne, V., Toplis, M.J., Berthet, S., Jones, J.. Highly reducing conditions during core formation on Mercury: Implications for internal structure and the origin of a magnetic field. Icarus 2010;206:199–209. doi:10.1016/j.icarus.2009.09.001.

Margot, J.L., Peale, S.J., Solomon, S.C., Hauck, S.A., Ghigo, F.D., Jurgens, R.F., Yseboodt, M., Giorgini, J.D., Padovan, S., Campbell, D.B.. Mercury's moment of inertia from spin and gravity data. Journal of Geophysical Research: Planets 2012;117(E12):E00L09. doi:10.1029/2012JE004161.

Mastrogiuseppe, M., Hayes, A.G., Poggiali, V., Lunine, J.I., Lorenz, R.D., Seu, R., Le Gall, A., Notarnicola, C., Mitchell, K.L., Malaska, M., Birch, S.P.D.. Bathymetry and composition of Titan's Ontario Lacus derived from Monte Carlo-based waveform inversion of Cassini RADAR altimetry data. Icarus 2018;300:203–209. doi:10.1016/j.icarus.2017.09.009.

Mastrogiuseppe, M., Poggiali, V., Hayes, A., Lorenz, R., Lunine, J., Picardi, G., Seu, R., Flamini, E., Mitri, G., Notarnicola, C., Paillou, P., Zebker, H.. The bathymetry of a titan sea. Geophysical Research Letters 2014;41(5):1432–1437. doi:10.1002/2013GL058618.

Mastrogiuseppe, M., Poggiali, V., Seu, R., Martufi, R., Notarnicola, C.. Titan dune heights retrieval by using Cassini Radar Altimeter. Icarus 2014;230:191–197. doi:10.1016/j.icarus.2013.09.028.

Mazarico, E., Barker, M., Neumann, G., Zuber, M., Smith, D.. Detection of the lunar body tide by the Lunar Orbiter Laser Altimeter. Geophysical Research Letters 2014a;41. doi:10.1002/2013GL059085.

Mazarico, E., Genova, A., Goossens, S., Lemoine, F.G., Neumann, G.A., Zuber, M.T., Smith, D.E., Solomon, S.C.. "the gravity field, orientation, and ephemeris of mercury from messenger observations after three years in orbit". Journal of Geophysical Research: Planets 2014b;119(12):2417–2436. doi:10.1002/2014JE004675.

Mazarico, E., Genova, A., Neumann, G., Smith, D., Zuber, M.. Simulated recovery of Europa's global shape and tidal Love numbers from altimetry and radio tracking during a dedicated flyby tour. Geophysical Research Letters 2015;42. doi:10.1002/2015GL063224.

Mazarico, E., Rowlands, D., Neumann, G., Smith, D., Torrence, M., Lemoine, F., Zuber, M.. Orbit determination of the Lunar Reconnaissance Orbiter. Journal of Geodesy 2012;86:193–207. doi:10.1007/s00190-011-0509-4.

McKinnon, W.B.. Convective instability in Europa's floating ice shell. Geophysical Research Letters 1999;26(7):951–954. doi:10.1029/1999GL900125.

Moore, W., Schubert, G.. The tidal response of Europa. Icarus 2000;147:317–319.

Moore, W., Schubert, G.. The tidal response of Ganymede and Callisto with and without liquid water oceans. Icarus 2003;16:223–226.

Moussessian, A., Blankenship, D., Plaut, J., Patterson, W., Gim, Y., Schroeder, D.. REASON for Europa. AGU Fall Meeting 2015;.

Munk, W., MacDonald, G.. The rotation of the earth; a geophysical discussion. Cambridge [Eng.] University Press, 1960.

Ness, N.F., Behannon, K.W., Lepping, R.P., Whang, Y.C.. The magnetic field of mercury, 1. Journal of Geophysical Research 1975;80(19):2708–2716. doi:10.1029/JA080i019p02708.

Neukum, G.. Cratering chronology in the jovian system and derivation of absolute ages. Lunar and Planetary Science Conference 2001;XXIX:Abstract 1428.

Neumann, G., Rowlands, D., Lemoine, F., Smith, D., Zuber, M.. Crossover analysis of Mars Orbiter Laser Altimeter data. Journal of Geophysical Research 2001;106:23753–23768. doi:10.1029/2000JE001381.

Neumann, G.A., Smith, D.E., Zuber, M.T.. Two Mars years of clouds detected by the Mars Orbiter Laser Altimeter. Journal of Geophysical Research (Planets) 2003;108:5023. doi:10.1029/2002JE001849.

Nimmo, F., Schenk, P.. Stereo and photoclinometric comparisons and topographic roughness of Europa. Lunar and Planetary Science 2008;XXXIX.

Noyelles, B., Frouard, J., Makarov, V., Efroimsky, M.. Spin-orbit evolution of Mercury revisited. icarus 2014;241:26–44. doi:10.1016/j.icarus.2014.05.045.

Nozette, S., Rustan, P., Pleasance, L.P., Kordas, J.F., Lewis, I.T., Park, H.S., Priest, R.E., Horan, D.M., Regeon, P., Lichtenberg, C.L., Shoemaker, E.M., Eliason, E.M., McEwen, A.S., Robinson, M.S., Spudis, P.D., Acton, C.H., Buratti, B.J., Duxbury, T.C., Baker, D.N., Jakosky, B.M., Blamont, J.E., Corson, M.P., Resnick, J.H., Rollins, C.J., Davies, M.E., Lucey, P.G., Malaret, E., Massie, M.A., Pieters, C.M., Reisse, R.A., Simpson, R.A., Smith, D.E., Sorenson, T.C., Breugge, R.W.V., Zuber, M.T.. The Clementine Mission to the Moon: Scientific Overview. Science 1994;266(5192):1835–1839. doi:10.1126/science.266.5192.1835.

Padovan, S., Margot, J.L., Hauck, S.A., Moore, W.B., Solomon, S.C.. "the tides of mercury and possible implications for its interior structure". Journal of Geophysical Research: Planets 2014;119(4):850–866. doi:10.1002/2013JE004459.

Paganelli, F., Janssen, M.A., Stiles, B., West, R., Lorenz, R.D., Lunine, J.I., Wall, S.D., Callahan, P., Lopes, R.M., Stofan, E., Kirk, R.L., Johnson, W.T.K., Roth, L., Elachi, C., the Radar Team, . Titan's surface from Cassini RADAR SAR and high resolution radiometry data of the first five flybys. Icarus 2007;191:211–222. doi:10.1016/j.icarus.2007.04.032.

Pappalardo, R., Collins, G., Head III, J., Helfenstein, P., McCord, T., Moore, J., Prockter, L., Schenk, P., Spencer, J.. Geology of Ganymede. p. 363–396.

Pappalardo, R., Phillips, B.. Europa Clipper Mission Concept: Exploring Jupiter's Ocean Moon. Eos 2014;95:165–167.

Pappalardo, R.T., Belton, M.J.S., Breneman, H.H., Carr, M.H., Chapman, C.R., Collins, G.C., Denk, T., Fagents, S., Geissler, P.E., Giese, B., Greeley, R., Greenberg, R., Head, J.W., Helfenstein, P., Hoppa, G., Kadel, S.D., Klaasen, K.P., Klemaszewski, J.E., Magee, K., McEwen, A.S., Moore, J.M., Moore, W.B., Neukum, G., Phillips, C.B., Prockter, L.M., Schubert, G., Senske, D.A., Sullivan, R.J., Tufts, B.R., Turtle, E.P., Wagner, R., Williams, K.K.. Does Europa have a subsurface ocean? Evaluation of the geological evidence. Journal of Geophysical Research: Planets 1999;104(E10):24015–24055. doi:10.1029/1998JE000628.

Pappalardo, R.T., Head, J.W., Greeley, R., Sullivan, R.J., Pilcher, C., Schubert, G., Moore, W.B., Carr, M.H., Moore, J.M., Belton, M.J.S., Goldsby, D.L.. Geological evidence for solid-state convection in Europa's ice shell. Nature 1998;391:365 – 368. doi:10.1038/34862.

Parisi, M., Iess, L., Finocchiaro, S.. The gravity fields of Ganymede, Callisto and Europa: how well can JUICE do? Geophysical Research Abstracts 2014;EGU2014:11758.

Peale, S.. Generalized Cassini's Laws. Astronomical Journal 1969;74:483. doi:10.1086/110825.

Peale, S.. Does Mercury have a molten core. Nature 1976a;262:765. doi:10.1038/262765a0.

Peale, S., Cassen, P., Reynolds, R.. Melting of Io by tidal dissipation. Science 1979;203:892–894. doi:10.1126/science.203.4383.892.

Peale, S.J.. Orbital resonances in the solar system. Annual review of astronomy and astrophysics 1976b;14:215–246. doi:10.1146/annurev.aa.14.090176.001243.

Peale, S.J.. The rotational dynamics of Mercury and the state of its core. p. 461–493.

Peale, S.J., Cassen, P.. Contribution of tidal dissipation to lunar thermal history. Icarus 1978;36:245–269. doi:10.1016/0019-1035(78)90109-4.

Peale, S.J., Gold, T.. Rotation of the Planet Mercury. Nature 1965;206:1240–1241. doi:10.1038/2061240b0.

Peale, S.J., Phillips, R.J., Solomon, S.C., Smith, D.E., Zuber, M.T.. A procedure for determining the nature of mercury's core. Meteoritics & Planetary Science 2002;37(9):1269–1283. doi:10.1111/j.1945-5100.2002.tb00895.x.

Perry, M.E., Neumann, G.A., Phillips, R.J., Barnouin, O.S., Ernst, C.M., Kahan, D.S., Solomon, S.C., Zuber, M.T., Smith, D.E., Hauck, S.A., Peale, S.J., Margot, J.L., Mazarico, E., Johnson, C.L., Gaskell, R.W., Roberts, J.H., McNutt, R.L., Oberst, J.. The low-degree shape of mercury. Geophysical Research Letters 2015;42(17):6951–6958. doi:10.1002/2015GL065101; 2015GL065101.

Phillips, R.J., Adams, G.F., Brown Jr., W.E., Eggleton, R.E., Jackson, P., Jordan, R., Peeples, W.J., Porcello, L.J., Ryu, J., Schaber, G., Sill, W.R., Thompson, T.W., Ward, S.H., Zelenka, J.S.. The Apollo 17 Lunar Sounder. In: Lunar and Planetary Science Conference Proceedings. volume 4 of *Lunar and Planetary Science Conference Proceedings*; 1973. p. 2821.

Plaut, J.J., Picardi, G., Safaeinili, A., Ivanov, A.B., Milkovich, S.M., Cicchetti, A., Kofman, W., Mouginot, J., F., W.M., Phillips, R.J., Clifford, S.M., Frigeri, A., Orosei, R., Federico, C., Williams, I.P., Gurnett, D.A., Nielsen, E., Hagfors, T., Heggy, E., Stofan, E.R., Plettemeier, D., Watters, T.R., Leuschen, C.J., Edenhofer, P.. "subsurface radar sounding of the south polar layered deposits of mars". Science 2007;316(5821):92–95. doi:10.1126/science.1139672.

Prockter, L.M., Lopes, R.M.C., Giese, B., Jaumann, R., Lorenz, R.D., Pappalardo, R.T., Patterson, G.W., Thomas, P.C., Turtle, E.P., Wagner, R.J.. Characteristics of Icy Surfaces. Space Science Reviews 2010;153(1):63–111. doi:10.1007/s11214-010-9649-8.

Raney, R.. The Delay/Doppler Radar Altimeter. IEEE TRANSACTIONS ON GEOSCIENCE AND REMOTE SENSING 1998;36:1578–1588.

Raney, R.. CryoSat SAR-Mode Looks Revisited. IEEE Transactions on Geoscience and Remote Sensing 2012;9:393–397.

Reynolds, R.T., Squyres, S.W., Colburn, D.S., McKay, C.P.. On the habitability of Europa. Icarus 1983;56:246–254. doi:10.1016/0019-1035(83)90037-4.

Ross, M., Schubert, G.. Tidally forced viscous heating in a partially molten Io. Icarus 1985;64:391–400. doi:10.1016/0019-1035(85)90063-6.

Roth, L., Saur, J., Retherford, K.D., Strobel, D.F., Feldman, P.D., McGrath, M.A., Nimmo, F.. Transient water vapor at europa's south pole. Science 2014;343(6167):171–174. doi:10.1126/science.1247051.

Rückriemen, T., Breuer, D., Spohn, T.. The Fe snow regime in Ganymede's core: A deep-seated dynamo below a stable snow zone. Journal of Geophysical Research (Planets) 2015;120:1095–1118. doi:10.1002/2014JE004781.

Saur, J., Duling, S., Roth, L., Jia, X., Strobel, D.F., Feldman, P.D., Christensen, U.R., Retherford, K.D., McGrath, M.A., Musacchio, F., Wennmacher, A., Neubauer, F.M., Simon, S., Hartkorn, O.. The search for a subsurface ocean in Ganymede with Hubble Space Telescope observations of its auroral ovals. Journal of Geophysical Research: Space Physics 2015;120(3):1715–1737. doi:10.1002/2014JA020778.

Schmidt, B.E., Blankenship, D.D., Patterson, G.W., Schenk, P.M.. Active formation of 'chaos terrain' over shallow subsurface water on Europa. Nature 2011;479:502–505. doi:10.1038/nature10608.

Schoemaker, E., Wolfe, R.. The Satellites of Jupiter; Univ. of Arizona Press. p. 277–339.

Schroeder, D.M., Blankenship, D.D., Young, D.A., Witus, A.E., Anderson, J.B.. Airborne radar sounding evidence for deformable sediments and outcropping bedrock beneath Thwaites Glacier, West Antarctica. Geophysical Review Letters 2014;41:7200–7208. doi:10.1002/2014GL061645.

Schroeder, D.M., Romero-Wolf, A., Carrer, L., Grima, C., Campbell, B.A., Kofman, W., Bruzzone, L., Blankenship, D.D.. Assessing the potential for passive radio sounding of Europa and Ganymede with RIME and REASON. Planetary and Space Science 2016;134:52–60. doi:10.1016/j.pss.2016.10.007.

Schubert, G., Anderson, J., Spohn, T., McKinnon, W.. Jupiter. The Planet, Satellites and Magnetosphere; Cambridge University Press. p. 281–306.

Schubert, G., Zhang, K., Kivelson, M., Anderson, J.. The magnetic field and internal structure of Ganymede. Nature 1996;384:544–545. doi:10.1038/384544a0.

Segatz, M., Spohn, T., Ross, M., Schubert, G.. Tidal dissipation, surface heat flow, and figure of viscoelastic models of Io. Icarus 1988;75:187–206. doi:10.1016/0019-1035(88)90001-2.

Seu, R., Biccari, D., Orosei, R., Lorenzoni, L.V., Phillips, R.J., Marinangeli, L., Picardi, G., Masdea, A., Zampolini, E.. SHARAD: The MRO 2005 shallow radar. Planetary and Space Science 2004;52:157–166. doi:10.1016/j.pss.2003.08.024.

Shida, T., Matsuyama, M.. Change of the plumb line referred to the axis of the Earth as found from the result of the international latitude observations. J Mem College Sci Eng, Kyoto Imp 1912;4:277–284.

Smith, B.A., Soderblom, L.A., Beebe, R., Boyce, J., Briggs, G., Carr, M., Collins, S.A., Cook, A.F., Danielson, G.E., Davies, M.E., Hunt, G.E., Ingersoll, A., Johnson, T.V., Masursky, H., McCauly, J., Morrison, D., Owen, T., Sagan, C., Shoemaker, E.M., Strom, R., Suomi, V.E., Veverka, J.. The Galilean Satellites and Jupiter: Voyager 2 Imaging Science Results. Science 1979;206(4421):927–950. doi:10.1126/science.206.4421.927.

Smith, D., Zuber, M., Neuman, G., Lemoine, F., Rowlands, D.. Orbit Determination of the Mars Global Surveyor Spacecraft using Laser Altimetry. In: AAS/Division for Planetary Sciences Meeting Abstracts #32. volume 32 of *Bulletin of the American Astronomical Society*; 2000. p. 1114.

Smith, D., Zuber, M., Neumann, G., Lemoine, F.. Topography of the Moon from the Clementine LIDAR. Journal of Geophysical Research 1997;102:1591. doi:10.1029/96JE02940.

Smith, D., Zuber, M., Sun, X., Neumann, G., Cavanaugh, J., McGarry, J., Zagwodzki, T.. Two-way Laser Link over Interplanetary Distance. Science 2006;311:53–53. doi:10.1126/science.1120091.

Smith, D.E., Zuber, M.T., Jackson, G.B., Cavanaugh, J.F., Neumann, G.A., Riris, H., Sun, X., Zellar, R.S., Coltharp, C., Connelly, J., Katz, R.B., Kleyner, I., Liiva, P., Matuszeski, A., Mazarico, E.M., McGarry, J.F., Novo-Gradac, A.M., Ott, M.N., Peters, C., Ramos-Izquierdo, L.A., Ramsey, L., Rowlands, D.D., Schmidt, S., Scott, V.S., Shaw, G.B., Smith, J.C., Swinski, J.P., Torrence, M.H., Unger, G., Yu, A.W., Zagwodzki, T.W.. The Lunar Orbiter Laser Altimeter Investigation on the Lunar Reconnaissance Orbiter Mission. Space Science Reviews 2010;150:209–241. doi:10.1007/s11214-009-9512-y.

Smith, D.E., Zuber, M.T., Neumann, G.A., Mazarico, E., Lemoine, F.G., Head III, J.W., Lucey, P.G., Aharonson, O., Robinson, M.S., Sun, X., Torrence, M.H., Barker, M.K., Oberst, J., Duxbury, T.C., Mao, D., Barnouin, O.S., Jha, K., Rowlands, D.D., Goossens, S., Baker, D., Bauer, S., Gläser, P., Lemelin, M., Rosenburg, M., Sori, M.M., Whitten, J., Mcclanahan, T.. Summary of the results from the lunar orbiter laser altimeter after seven years in lunar orbit. Icarus 2017;283:70–91. doi:10.1016/j.icarus.2016.06.006.

Smith, D.E., Zuber, M.T., Phillips, R.J., Solomon, S.C., Hauck, S.A., Lemoine, F.G., Mazarico, E., Neumann, G.A., Peale, S.J., Margot, J.L., Johnson, C.L., Torrence, M.H., Perry, M.E., Rowlands, D.D., Goossens, S., Head, J.W., Taylor, A.H.. Gravity Field and Internal Structure of Mercury from MESSENGER. Science 2012;336:214. doi:10.1126/science.1218809.

Smith, D.E., Zuber, M.T., Solomon, S.C., Phillips, R.J., Head, J.W., Garvin, J.B., Banerdt, W.B., Muhleman, D.O., Pettengill, G.H., Neumann, G.A., Lemoine, F.G., Abshire, J.B., Aharonson, O., Brown C., D., Hauck, S.A., Ivanov, A.B., McGovern, P.J., Zwally, H.J., Duxbury, T.C.. The Global Topography of Mars and Implications for Surface Evolution. Science 1999;284:1495. doi:10.1126/science.284.5419.1495.

Soderlund, K.M., Schmidt, B.E., Wicht, J., Blankenship, D.D.. Ocean-driven heating of Europa's icy shell at low latitudes. Nature Geoscience 2014;7:16–19. doi:10.1038/ngeo2021.

Sohl, F., Spohn, T., Breuer, D., Nagel, K.. Implications from Galileo observations on the interior structure and chemistry of the Galilean satellites. Icarus 2002;157(1):104 – 119. doi:10.1006/icar.2002.6828.

Solomon, S.C., McNutt Jr, R.L., Prockter, L.M.. "mercury after the messenger flybys: An introduction to the special issue of planetary and space science ". Planetary and Space Science 2011;59(15):1827 – 1828. doi:10.1016/j.pss.2011.08.004.

Sotin, C., Grasset, O., Beauchesne, S.. Solar system ices; Springer Netherlands. p. 79–96. doi:10.1007/978-94-011-5252-5-4.

Sparks, W.B., McGrath, M., Schmidt, B., Bergeron, E., Hand, K., Spencer, J., Cracraft, M., Deustua, S.. Evidence of Plumes on Europa from far-ultraviolet observations with HST. In: American Astronomical Society Meeting Abstracts. volume 231 of *American Astronomical Society Meeting Abstracts*; 2018. p. 106.03.

Sparks, W.B., Schmidt, B.E., McGrath, M.A., Hand, K.P., Spencer, J.R., Cracraft, M., Deustua, S.E.. Active cryovolcanism on europa? The Astrophysical Journal Letters 2017;839(2):L18.

Spohn, T., Schubert, G.. Oceans in the icy Galilean satellites of Jupiter? Icarus 2003;161:456–467. doi:10.1016/S0019-1035(02)00048-9.

Spohn, T., Sohl, F., Wieczerkowski, K., Conzelmann, V.. The interior structure of Mercury: what we know, what we expect from BepiColombo. Planetary and Space Science 2001;49:1561–1570. doi:10.1016/S0032-0633(01)00093-9.

Stark, A., Hussmann, H., Steinbrügge, G., Gläser, P., Gwinner, K., Oberst, J., Casasco, M., Cremonese, G.. In-flight alignment calibration between a laser altimeter and an imaging system - Application to the BepiColombo mission. In: EGU General Assembly Conference Abstracts. volume 19 of *EGU General Assembly Conference Abstracts*; 2017a. p. 8364.

Stark, A., Oberst, J., Hussmann, H.. Mercury's resonant rotation from secular orbital elements. Celestial Mechanics and Dynamical Astronomy 2015a;123(3):263–277. doi:10.1007/s10569-015-9633-4.

Stark, A., Oberst, J., Preusker, F., Peale, S.J., Margot, J.L., Phillips, R.J., Neumann, G.A., Smith, D.E., Zuber, M.T., Solomon, S.C.. "first messenger orbital observations of mercury's librations". Geophysical Research Letters 2015b;42(19):7881–7889. doi:10.1002/2015GL065152.

Stark, A., Oberst, J., Scholten, F., Gläser, P.. Measurements of Moon's Rotation by Co-Registration of Laser Altimeter Profiles and Stereo Terrain Models. In: Lunar and Planetary Science Conference. volume 48; 2017b. p. 2304.

Steinbrügge, G., Stark, A., Hussmann, H., Sohl, F., Oberst, A.. Measuring tidal deformations by laser altimetry. A performance model for the Ganymede Laser Altimeter. Planetary and Space Science 2015;doi:10.1016/j.pss.2015.06.013.

Steinke, T., Stark, A., Steinbrügge, G., Hussmann, H., Oberst, J.. Estimation of Ganymede's Topography, Rotation and Tidal Deformation - a Study of Synthetic Ganymede Laser Altimeter Observations. European Planetary Science Congress 2015;10:EPSC2015–514.

Stevenson, D.J., Spohn, T., Schubert, G.. Magnetism and thermal evolution of the terrestrial planets. Icarus 1983;54:466–489. doi:10.1016/0019-1035(83)90241-5.

Sun, X., Barker, M.K., Mao, D., Marzarico, E., Neumann, G.A., Skillman, D.R., Zagwodzki, T.W., Torrence, M.H., Mcgarry, J., Smith, D.E., Zuber, M.T.. In-orbit Calibration of the Lunar Orbiter Laser Altimeter Via Two-Way Laser Ranging with an Earth Station. AGU Fall Meeting Abstracts 2014;:P13B–3814.

Thomas, N., Spohn, T., Barriot, J.P., Benz, W., Beutler, G., Christensen, U., Dehant, V., Fallnich, C., Giardini, D., Groussin, O., Gunderson, K., Hauber, E., Hilchenbach, M., Iess, L., Lamy, P., Lara, L.M., Logonné, P., Lopez-Moreno, J., Michaelis, H., Oberst, J., Resendes, D., Reynaud, J.L., Rodrigro, R., Sasaki, S., Seiferlin, K., Wieczorek, M., Whitby, J.. The BepiColombo Laser Altimeter (BELA): Concept and baseline design. Planetary and Space Science 2007;55:1398–1413. doi:10.1016/j.pss.2007.03.003.

Thor, R., Kallenbach, R., Christensen, U., Oberst, J., Stark, A., Steinbrügge, G.. Improved algorithms for the retrieval of the h2 Love number of Mercury from laser altimetry data. In: EGU General Assembly Conference Abstracts. volume 19; 2017. p. 7789.

Tosi, N., Grott, M., Plesa, A.C., Breuer, D.. Thermochemical evolution of mercury's interior. Journal of Geophysical Research: Planets 2013;118(12):2474–2487. doi:10.1002/jgre.20168.

Tufts, B., Greenberg, R., Hoppa, G., Geissler, P.. Lithospheric Dilation on Europa. Icarus 2000;146(1):75 – 97. doi:10.1006/icar.2000.6369.

Van Hoolst, T., Baland, R.M., Trinh, A.. On the librations and tides of large icy satellites. Icarus 2013;226(1):299 – 315. doi:10.1016/j.icarus.2013.05.036.

Vance, S., Bouffard, M., Choukroun, M., Sotin, C.. Ganymede's internal structure including thermodynamics of magnesium sulfate oceans in contact with ice. Planetary and Space Science 2014;96:62–70. doi:10.1016/j.pss.2014.03.011.

Verma, A.K., Margot, J.L.. Mercury's gravity, tides, and spin from messenger radio science data. Journal of Geophysical Research: Planets 2016;121(9):1627–1640. doi:10.1002/2016JE005037.

Verma, A.K., Margot, J.L.. Expected Precision of Europa Clipper Gravity Measurements. arXiv 2018;ArXiv: 1801.08946v1.

Wahr, J., Selvans, Z., Mullen, M., Barr, A., Collins, G., Selvans, M., Pappalardo, R.. Modeling stresses on satellites due to nonsynchronous rotation and orbital eccentricity using gravitational potential theory. Icarus 2009;200:188–206. doi:10.1016/j.icarus.2008.11.002.

Wahr, J., Zuber, M., Smith, D., Luine, J.. Tides on Europa, and the thickness of Europa's icy shell. Journal of Geophysical Research 2006;111:E12005. doi:10.1029/2006JE002729.

Watters, T.R., Leuschen, C.J., Plaut, J.J., Picardi, G., Safaeinili, A., Clifford, S.M., Farrell, W.M., Ivanov, A.B., Phillips, R.J., Stofan, E.R.. MARSIS radar sounder evidence of buried basins in the northern lowlands of Mars. Nature 2006;444:905–908. doi:10.1038/nature05356.

Wieczerkowski, K.. Gravito-Viscoelasto-dynamics for generalized rheologies with applications to Jupiter's Moon Io and the Earth. Deutsche Geodaetische Kommission 1999;Reihe C 515.

Wieczorek, M.A., Correia, A.C.M., Le Feuvre, M., Laskar, J., Rambaux, N.. Mercury's spin-orbit resonance explained by initial retrograde and subsequent synchronous rotation. Nature Geoscience 2012;5:18–21. doi:10.1038/ngeo1350. arXiv:1112.2384.

Wingham, D.. CryoSat: a mission to the ice fields of Earth. ESA Bulletin 2005;122:10–17.

Wu, X., Bar-Sever, Y.E., Folkner, W.M., Williams, J.G., Zumberge, J.F.. Probing Europa's hidden ocean from tidal effects on orbital dynamics. Geophysical Research Letters 2001;28(11):2245–2248. doi:10.1029/2000GL012814.

Yoder, C.. How tidal heating in Io drives the Galilean orbital resonance locks. Nature 1979;279:767–770. doi:10.1038/279767a0.

Yoder, C., Peale, S.. The tides of Io. Icarus 1981;47:1–35. doi:10.1016/0019-1035(81)90088-9.

Zahnle, K., Dones, L., Levison, H.. Cratering rates on the Galilean satellites. Icarus 1998;136:202–222.

Zebker, H.A., Gim, Y., Callahan, P., Hensley, S., Lorenz, R., Cassini Radar Team, . Analysis and interpretation of Cassini Titan radar altimeter echoes. Icarus 2009;200:240–255. doi:10.1016/j.icarus.2008.10.023.

Zschau, J.. Tidal Friction and the Earth's Rotation; Springer Berlin Heidelberg. p. 62–94. doi:10.1007/978-3-642-67097-8-7.

Zuber, M.T., Smith, D.E., Lemoine, F.G., Neumann, G.A.. The Shape and Internal Structure of the Moon from the Clementine Mission. Science 1994;266:1839–1843. doi:10.1126/science.266.5192.1839.

Zuber, M.T., Smith, D.E., Phillips, R.J., Solomon, S.C., Neumann, G.A., Hauck, S.A., Peale, S.J., Barnouin, O.S., Head, J.W., Johnson, C.L., Lemoine, F.G., Mazarico, E., Sun, X., Torrence, M.H., Freed, A.M., Klimczak, C., Margot, J.L., Oberst, J., Perry, M.E., McNutt, R.L., Balcerski, J.A., Michel, N., Talpe, M.J., Yang, D.. Topography of the Northern Hemisphere of Mercury from MESSENGER Laser Altimetry. Science 2012;336(6078):217–220. doi:10.1126/science.1218805.

Zuber, M.T., Smith, D.E., Solomon, S.C., Muhleman, D.O., Head, J.W., Garvin, J.B., Abshire, J.B., Bufton, J.L.. The mars observer laser altimeter investigation. Journal of Geophysical Research 1992;97(E5):7781–7797. doi:10.1029/92JE00341.

Zuber, M.T., Smith, D.E., Zellar, R.S., Neumann, G.A., Sun, X., Katz, R.B., Kleyner, I., Matuszeski, A., McGarry, J.F., Ott, M.N., Ramos-Izquierdo, L.A., Rowlands, D.D., Torrence, M.H., Zagwodzki, T.W.. The lunar reconnaissance orbiter laser ranging investigation. Space Science Reviews 2010;150(1):63–80. doi:10.1007/s11214-009-9511-z.

Zurek, R.W., Smrekar, S.E.. An overview of the Mars Reconnaissance Orbiter (MRO) science mission. Journal of Geophysical Research (Planets) 2007;112:E05S01. doi:10.1029/2006JE002701.

Acknowledgments

I would like to thank Jürgen Oberst to give me the opportunity to work in his group and for the support of this thesis. A special thanks to Hauke Hußmann for his consistent support during all the time and for giving me the opportunity to be part of these exciting projects. I would like also to thank Alexander Stark for having me taught a lot and for all the fruitful discussions we had. It has been a pleasure to work with you guys.
I would further like to thank Dustin Schroeder for his support and for hosting me at JPL. I also thank Mark Haynes for the good collaboration during and after that time. It's been a productive but also very enjoyable stay in Pasadena. Also big thanks for Donald D. Blankenship for involving me into REASON. I thank Tilman Spohn and Nick Thomas for reviewing this thesis and Harald Schuh for being the chair of the dissertation committee.
I would further like to thank the complete teams of BELA, GALA, and REASON for all the good collaboration. It is an honor to be part of these teams. I thank Christian Althaus and Dennis Höning for all the serious and less serious discussions we had during lunch. Further, I thank my parents Lieselotte Steinbrügge and Johannes Rohbeck for their support. And last but not least I thank Joana Voigt for her love and never ending support.